

Elevation dependent landscape processes in rapidly warming sub-Arctic mountains:
influences of snow, temperature and vegetation

by

Scott Norman Williamson

A thesis submitted in partial fulfillment of the requirements for the degree of

Doctor of Philosophy

in

Ecology

Department of Biological Sciences
University of Alberta

© Scott Norman Williamson, 2015

Abstract

The loss of spring snow in the Northern Hemisphere has been dramatic. From 1967 to 2008 snow cover decreased by 14% in May and 46% in June, with a simultaneous reduction in snow cover duration of 6 – 8 days per decade in both summer and fall. These effects have been particularly pronounced in the Kluane region of the southwest Yukon, making the area well suited for a detailed study of the effects of the reciprocal interactions of snow cover decline with ecological, geographical and climatological features. The mountainous Kluane region, like most of the Arctic, is difficult to access and has few long-term ground-based observations, which necessitates the use of remote sensing and mathematical modelling to determine surface characteristics.

This thesis integrates data from diverse sources including meteorological stations, field albedo measurements, downscaled surface temperature, infrared Land Surface Temperature (LST), snow cover, land cover, and cloud cover to quantify the snow albedo feedback in the southwest Yukon.

The first four chapters of this thesis addresses the validation and integration of different sources of data. My main findings are that (i) cloud contamination of MODIS-derived day-time LST within the study area is ~15%, which cools affected grid cells by no more than 2 K; (ii) combining night-time with day-time LST leads to a cold bias when compared to temporally averaged (8-day or monthly) air temperature; and (iii) the cold bias gets larger as within grid cell snow fraction increases.

The last three chapters of my thesis attempts to account for various feedback processes using a combination of field measurements and modeling studies. Following

spring snow melt, albedo increases for woody tundra vegetation as the growing season progresses, but the increase is small in magnitude compared to the albedo difference between snow covered and snow-free land. The albedo increase caused by the progressive canopy closure of woody vegetation is differentiated by stature and species, a result that will influence tundra energy balance on a successional timescale in a wetter, warmer Arctic. Finally, I demonstrate that the 35 – 50% decrease in snow cover in tundra in May between 2000 and 2008 produces a small radiative feedback to climate, but the strength is insufficient to influence the monthly average temperature change. This suggests that snow cover and temperature change is largely the result of external forcing consistent with meridional heat transport. Furthermore, the similarity in temperature trends among three land cover types (Icefields, Conifer forests with no snow, and Tundra characterized by a large decrease in snow cover) indicates that the snow cover albedo feedback contributes < 6% (or the equivalent of $<0.091 \text{ W m}^{-2}$ per decade over the 2000 to 2008 study period) to the changes observed in air temperature. Consequently, if the atmospheric local heating related to the large albedo decrease caused by snow cover decline is small, the much smaller albedo changes caused by successional changes in vegetation will be negligible over the short-term.

Preface

This thesis is an original work by Scott Norman Williamson. At the time of submission of this thesis Chapter Two has been published as Williamson, S. N., Hik, D. S., Gamon, J. A., Kavanaugh, J. L., & Koh, S. (2013). Evaluating cloud contamination in clear-sky MODIS Terra daytime land surface temperatures using ground-based meteorology station observations. *Journal of Climate*, 26(5), 1551-1560. Chapter Three has been published as Williamson, S. N., Hik, D. S., Gamon, J. A., Kavanaugh, J. L., & Flowers, G. E. (2014). Estimating temperature fields from MODIS land surface temperature and air temperature observations in a sub-Arctic Alpine environment. *Remote Sensing*, 6(2), 946-963. I am the first author on all chapters within this thesis, and took the lead role in all aspects of their design and execution.

Acknowledgements

I would like to thank my thesis supervisors Dr. David Hik and Dr. John Gamon, and Dr. Jeffery Kavanaugh who was a member of my supervisory committee.

The glaciology group at the University of British Columbia, headed by Dr. Garry Clarke, provided downscaled climate data, produced by Dr. Alexander Jarocsh and Dr. Farron Anslow. The generous provision of meteorological measurement and logging capacity was also provided by Dr. Clarke. Dr. Gwenn Flower's glaciology group at Simon Fraser University, and Dr. Christian Zdanowicz, at Uppsala University, provided much needed, and difficult to acquire meteorological field measurements from the St. Elias Icefields. Additional downscaled climatology data was provided by the Scenarios Network for Alaska + Arctic Planning (SNAP) at the University of Alaska Fairbanks.

At the University of Alberta, Lorne LeClair provided advice on computing and Charlene Neilson helped with Geographic Information Systems. Claude Labine at Campbell Scientific generously spent a few days providing me with an introductory course for programming Campbell Scientific loggers.

Sian Williams, Lance Goodwin and Andy Williams at Kluane Lake Research Station provided logistical support for much of the fieldwork conducted in the Kluane region of the Yukon.

Air temperature data for the southwest Yukon was obtained through the Environment Canada's National Climate Data and Information Archive. MODerate resolution Imaging Spectroradiometer (MODIS) data, which forms the backbone of this thesis, was provided free of charge by the Land Processes Distributed Active Archive Centre

(LPDAAC). The GLOBCOVER product is freely available by the European Space Agency.

Financial support for this project was provided by the Canada Foundation for Innovation, the Canada Research Chairs Program, the Government of Canada International Polar Year Program (PPS Arctic Canada Project), NSERC (Discovery and International Polar Year Programs), the Northern Scientific Training Program (AANDC), the Canadian Circumpolar Institute at the University of Alberta, Alberta Innovates Centre for Research Excellence, the W. Garfield Weston Foundation, Wildlife Conservation Society of Canada, and the Arctic Institute of North America (AINA).

Scholarships to Scott Williamson were awarded by NSERC EnviroNorth Interdisciplinary Doctoral Scholarship, the Alberta Government's Queen Elizabeth II Doctoral Scholarship, the Profiling Alberta's Graduate Students Award, and the W. Garfield Weston Foundation Fellowship for Northern Conservation.

CONTENTS

Abstract.....	ii
Preface.....	iv
Acknowledgements.....	v
Chapter 1: The Relationship between Landscape Ecology, Climate and Snow	
Cover Decline in Altitudinal Tundra.....	1
Introduction Arctic amplification and Local Climate Feedbacks.....	1
Local Heating in the Arctic.....	6
Cloud Feedbacks.....	11
Study Area.....	13
Observations & Measurements.....	15
Objectives.....	16
References.....	27

Chapter 2: Evaluating cloud contamination in clear-sky MODIS Terra daytime

Land Surface Temperatures using ground-based meteorology station observations.....36

 Introduction.....36

 Study Area.....38

 Data.....39

 MODIS (MOD11A1) Terra Collection 5 clear-sky daytime Land

 Surface Temperatures (LST).....40

 MODIS data pre-processing.....42

 Meteorology station air temperature and weather observations.....42

 MODIS and Meteorology data intersection.....43

 Statistical Analysis.....43

Results.....44

Discussion.....47

Conclusions.....50

References.....59

Chapter 3: Estimating Temperature Fields from MODIS Land Surface Temperature

and Air Temperature Observations in a Sub-Arctic Alpine environment.....62

 Introduction.....62

 Study Area.....67

 Methods.....68

 MODIS Version 5 Clear Sky Daytime Land Surface

 Temperatures (LST).....68

 Pre-Processing of MODIS Terra Tile and Terra and Aqua

 Swath Data.....69

 Meteorology Station Air Temperature Data.....71

 Interpolated Curve Mean Daily Surface Temperature (ICM).....71

 Mean Daily Surface Temperature Calculated from Maximum and

 Minimum LST (MMM).....74

 Results.....75

 Discussion.....76

 Conclusions.....80

 References.....91

Chapter 4: Night-Time Cloud Cover over Snow Covered Mountainous Terrain
Produces an Inherent Cold Bias in MODIS LST when compared to Average

Air Temperature.....	97
Introduction.....	97
Study Area.....	101
Methods.....	103
Processing MODIS data	103
Calculating mean monthly surface temperature from daily maximum and minimum LST.....	105
MODIS Snow cover.....	105
Scenarios Network for Alaska + Arctic Planning (SNAP) air temperature.....	106
NCEP North American Regional Re-analysis (NARR) Downscaling.....	106
Statistical analyses.....	107
Results.....	107
Discussion.....	110

Conclusions.....	112
References.....	121
Chapter 5: Phenology and species determine growing season albedo increase at the altitudinal limit of shrub growth in the sub-Arctic.....	126
Introduction.....	126
Methods.....	129
Field Albedo Measurements.....	129
Field Spectra Measurements.....	131
Field Observation of Phenological Change.....	132
MODIS Albedo.....	133
Solar Radiation Energy Budget Calculations.....	133
Statistical Analyses.....	135
Results.....	136
Discussion.....	138
Conclusions.....	143
References.....	149

Chapter 6: Spring snow cover decline in altitudinal tundra provides a minimal contribution to Arctic temperature amplification	155
Introduction.....	155
Study Area.....	157
Methods.....	159
MODIS LST.....	159
Maximum LST.....	161
MODIS Snow & Cloud cover.....	161
NCEP North American Regional Re-analysis (NARR) downscaling...	162
Air Temperature.....	163
Pacific Decadal Oscillation (PDO).....	163
Statistical Analysis.....	164
Results.....	164
Discussion.....	167
Conclusions.....	171
References.....	181
 Chapter 7: Summary & Conclusions: Warming in sub-Arctic Mountains.....	 188

Introduction.....	188
Summary of Results.....	189
Conclusions & Future work.....	195
References.....	199
Inclusive Bibliography.....	201

TABLES

Table 2-1: Station information for the four Environment Canada locations in the southwest Yukon.....	52
Table 3-1: Description and location of meteorology stations in southwest Yukon.....	82
Table 3-2: Coefficient of determination (R^2), root mean square error (RMSE) and skew between daily air temperature averages and modeled mean daily surface temperature (ICM & MMM).....	83
Table 3-3: Number of daily minimum and maximum values observed and calculated (mean) for seven meteorology stations for period between May 1 and August 31, 2008.....	83
Table 3-4: Number of 8-day composite values observed and calculated (mean) for seven meteorology stations for period between May 1 and August 31, 2008.....	84
Table 4-1: Validation meteorological stations, descriptions and locations.....	114
Table 4-2: The average number of daily measurements of maximum and minimum temperature for each month and 10 % snow cover bins, including standard deviation. This table is presented with the same categorical breaks as figure 4-2.....	115
Table 4-3: The comparison of air temperature from nine meteorological stations to the intersecting NARR, SNAP and LST (average, maximum and minimum) grid cells. Included is the number of observations of minimum and maximum LST. NA refers to LST grid cell's where Average LST could not be calculated because minimum or	

maximum LST were not acquired.....116

Table 5-1: Site characteristics for representative tundra plant communities. Dominant plant cover is presented as a percentage of plot area, and was assessed using the point intercept method. Vascular plants were identified to species, but are grouped here to the main functional types of interest. Cover by different plant groups overlaps, so percentages do not sum to 100%. Mean growing season albedo (\pm SD) is the average of measurements acquired one hour around solar noon July and August for 2012. The 2013 albedo values (\pm SD) are the averages of July 15 and 29 measurements recorded over 10 minutes at each site under direct sunlight within two hours of solar noon.....145

FIGURES

- Figure 1-1: The Yukon Territory, Canada, including major rivers and lakes. The smaller outline in the bottom left of the figure (southwest) is the Kluane study area. The star marks Mount Logan and the dendritic shape marks Kluane Lake. The line marks a cross sectional elevation profile, between sea-level at Icy Bay, Alaska, and Carmacks, Yukon. Solid circles indicate locations of Environment Canada meteorological monitoring stations.....19
- Figure 1-2: Digital Elevation Map covering Alaska, the Yukon and northern British Columbia. The smaller outline in the bottom right of the figure (southwest) is the Kluane study area. The line marks a cross sectional elevation profile displayed in figure.....20
- Figure 1-3: Elevation transect between Icy Bay Alaska and Carmacks Yukon. Annual average total precipitation is also included. Precipitation for Icy Bay was recorded at Yakutat, Alaska (Approximatley 100 km south east). Kluane lake precipitation was measured at the Burwash Landing. The Carmacks precipitation was measured at Pelly Crossing (Approximately 90 km north). These data originate with the National Ocean and Atmospheric Administration (NOAA) and are 1981 – 2010 averages.....21
- Figure 1-4: GLOBCOVER land cover product covering Alaska, the Yukon and northern British Columbia. The Yukon and the smaller Kluane study area are marked by the black outlines.....22
- Figure 1-5: Sparse vegetation dry tundra in the Ruby Range. Note the snow patches and clouds in the background.....23

Figure 1-6: Low elevation conifer (*Picea glauca*) near Kluane Lake Research Station at the south end of Kluane Lake looking east into the Ruby Range. Note the snow cover at higher elevation in the Ruby Range.....23

Figure 1-7: Mount Logan, the highest peak (5,959 m) in the St. Elias Mountains. This image represents the GLOBCOVER Permanent Snow & Ice category.....23

Figure 1-8: May average air temperature recorded at Burwash Landing Environment Canada Station. The lower plot is May monthly averages of Pacific Decadal Oscillation. The horizontal dotted line in the Temperature plot is the 1967-2014 May average air temperature (5.6 °C). The solid lines indicate the trend. Note that PDO is evenly distributed between positive and negative phases between 2000 and 2008.....24

Figure 1-9: Conceptual diagram of elevational dependent landscape processes related to spring snow cover derived albedo change. The left panel represents the land cover related to elevation, the middle panel represents remotely sensed grid cell level changes in albedo and the right panel represents hypothetical changes in temperature (T) related to inter-annual spring time steps t_1 and t_225

Figure 1-10: Elevational dependent landscape processes in rapidly warming sub-Arctic mountains: influences of snow, temperature and vegetation, thesis outline diagram.....26

Figure 2-1: Southwest Yukon study area showing the location of Environment Canada meteorology air temperature recording stations (black triangles) and air temperature and sky observation recording stations (black circles). Base Landsat mosaic of the Yukon was obtained from the Yukon Government, Department of Geomatics.....53

Figure 2-2: 2000 – 2008 temporally matched MODIS LST versus Environment Canada air temperature at Carmacks, Haines Junction, Whitehorse, and Burwash Landing stations. The solid line indicates the quadratic fit and the dashed line indicates the 1:1 line.....54

Figure 2-3: 2000 – 2008 temporally matched MODIS clear-sky LST versus Environment Canada air temperature at Whitehorse, and Burwash for ground based assessment of cloud content, but including all MODIS temperature quality flag information. “Clear” sky (top), “mainly clear” sky conditions (middle), and “mostly cloudy” sky conditions (bottom). The solid line indicates a quadratic fit; the dashed line indicates a 1:1 line.....55

Figure 2-4: 2000 – 2008 temporally matched MODIS clear-sky LST versus Environment Canada air temperature at Whitehorse for ground based cloud content assessment. “Clear” sky (top), “mainly clear” sky conditions (middle), and “mostly cloudy” sky conditions (bottom). The left column is MODIS LST with “good” quality flag values and the right column contains LST values of “unreliable or unquantifiable” quality. The solid line indicates a quadratic fit; the dashed line indicates a 1:1 line.....56

Figure 2-5: 2000 – 2008 temporally matched MODIS clear-sky LST versus Environment Canada air temperature at Burwash for ground based cloud content assessment. “Clear” sky (top), “mainly clear” sky conditions (middle), and “mostly cloudy” sky conditions (bottom). The left column is MODIS LST with “good” quality flag values and the right column contains LST values of “unreliable or unquantifiable”

quality. The solid line indicates a quadratic fit; the dashed line indicates a 1:1 line.....57

Figure 2-6: 2000 – 2008 temporally matched MODIS clear-sky LST versus Environment Canada air temperature at Whitehorse and Burwash for “good” quality “mainly clear” and “mostly cloudy” data from Figures 4 and 5. On these are the plotted quadratic fits found for “clear” sky and “good” quality data for each site (solid line). The dashed line is the RMS generated from the “clear” sky “good” quality data specific to each site. Any points falling below the bottom dashed line are likely cloud contaminated.....58

Figure 3-1: Southwest Yukon study area including the location of Environment Canada meteorology recording stations (Circles) and validation meteorology recording stations (Tundra–Triangles; Barren or Glacier–Pentagons). The light grey shaded region in the bottom left of the study area is Kluane National park. The darker shaded region within Kluane Park is the St. Elias Icefield. The four irregular polygons are Thiessen polygons derived from locations of Environment Canada meteorology stations.....85

Figure 3-2: Solar View Time for MODIS Terra LST (MOD11A1) observations from 18 April, 2008, covering the southwest corner of the Yukon Territory.....86

Figure 3-3: Mean Daily Surface Temperature (ICM) Algorithm flow diagram, describing how MODIS LST and air temperature records are combined to produce a mean daily surface temperature.....87

Figure 3-4: Air temperature between 8 AM and 2 PM at Whitehorse on 20 October 2008. The dashed line indicates the polynomial trend line and the solid line (270.9 K) indicates the average air temperature between 12:01 AM and 11:59 PM on 20 October 2008. Hour on the x axis indicates time in hours.....88

Figure 3-5: Modeled Mean Daily Surface Temperature (ICM) *versus* mean daily air temperature at non-vegetated glacier and rocky ridge locations in the flanks of the St. Elias Mountains and at vegetated sites (John Creek Station, Ruby Range North Station, and Pika Camp Station) east of Kluane Lake. The dashed lines indicate the 1:1 lines; the solid lines indicate the linear trends.....89

Figure 3-6: Daily mean Land Surface Temperature computed from maximum and minimum daily LST (MMM) compared to daily average air temperature calculated from hourly means at seven stations in the southwest Yukon (open circles and the solid line is the linear trend). The 8-day LST was computed from maximum and minimum daily values (closed circles, and the dotted line is the linear trend). The dashed line indicates the 1:1 line.....90

Figure 4-1: The southwest Yukon study area bounded by the thick black line. The grey portion is the glaciated region of Kluane National Park. The elevational gradient extends from the summit of Mt Logan (5959 m) to Kluane Lake (780 m), and some lower elevation drainages. Two Environment Canada meteorological monitoring stations are located within the study area at Haines Junction (655 m) and Burwash Landing (795 m). Nine additional meteorological monitoring stations are found on Permanent Snow & Ice and Sparse Vegetation & Barren land covers

(solid triangles).....117

Figure 4-2: Downscaled interpolated air temperature (SNAP) and downscaled NARR surface temperature plotted with MODIS Average Land Surface Temperature (LST) separated by snow fractions in 10% bins, for May through August 2008 monthly means. Six aggregated land cover classes decrease in elevation from a) Permanent Snow and Ice to f) Conifer forest. Error bars indicate standard error.....118

Figure 4-3: Downscaled interpolated air temperature (SNAP) and downscaled NARR surface temperature plotted with MODIS Maximum Land Surface Temperature (LST) separated by snow fractions in 10% bins, for May through August 2008 monthly means. Six aggregated land cover classes decrease in elevation from a) Permanent Snow and Ice to f) Conifer forest. Error bars indicate standard error.....119

Figure 4-4: Downscaled interpolated air temperature (SNAP) and downscaled NARR surface temperature plotted with MODIS Minimum Land Surface Temperature (LST) separated by snow fractions in 10% bins, for May through August 2008 monthly means. Six aggregated land cover classes decrease in elevation from a) Permanent Snow and Ice to f) Conifer forest. Error bars indicate standard error.....120

Figure 5-1: Characteristics of the six dominant vegetation types. a) Average broadband albedo during June, July and August 2012 (closed points) calculated for one hour before and after solar noon, compiled from 1-min averages for the six vegetation cover types; standard deviations for albedo measurements ranged from 0.001 to 0.006 indicating the standard errors are on the same order of size as the point symbols, thus no error bars are included. b) Photographs of the six sites. c) Spectral reflectance of the 6 sites on 15

August 2012. Areas in the scans affected by atmospheric water content have been removed. The depths of troughs at ~1000 nm and ~1200 nm (vertical lines) are indicative of Leaf Area Index (LAI), where deeper troughs indicate higher LAI. The two dotted horizontal lines at reflectance values of 10% and 30% are for reference.....146

Figure 5-2: Conceptual models of albedo change related to seasonal phenology and tundra vegetation. The potential for increasing growing season albedo in tundra landscapes has been attributed to advanced spring snowmelt (A) and delayed onset of snow at the end of summer (B). The darker areas represent the amount of increased heating attributed to a change in snow cover albedo and this influence will generally be much greater in spring compared to late summer because there is more solar incoming radiation earlier in the season (dashed line; W/m^2 , data calculated at $61.2^\circ N$; $138.3^\circ W$ for 70% cloud cover which was the decadal average cloud cover from 2000-2010 at this site). Based on our measurements in Figure 5-1, summer (2012) average albedo will be greatest near then end of the growing season (C; light blue), however the average increase in albedo over the snow free season has the potential to partially negate increased heating caused by advanced snowmelt or delayed onset when calculated for the entire snow free season.....147

Figure 5-3: Modeled daily average incoming solar radiation with no clouds (solid line) and with 70% cloud cover (dashed line) for 2012. Instrumental values (open circles) are shown for CM6b field measurements of daily average incoming solar radiation between June 21 and December 30, 2012.....148

Figure 6-1: Figure 6-1: The southwest Yukon study area bounded by the thick black line. The grey portion is the glaciated region of Kluane National Park, olive colour indicates sparse vegetation (tundra) and the green indicates conifer forest. The elevational gradient extends from the summit of Mt Logan (5959 m) to Kluane Lake (780 m), and some lower elevation drainages. An Environment Canada meteorological station is located at Burwash Landing and is referred to as Burwash (A).....172

Figure 6-2: Plots of May monthly average Maximum Land Surface Temperature (top panel), Downscaled North American Regional Re-analysis surface temperatures (second panel from top), MODIS snow fraction (third panel from top) and MODIS cloud fraction (bottom panel) for the years 2000 through 2008. The dark green trends indicate Conifer land cover, Olive indicates Tundra, and white indicates Icefield. The bottom panel uses the same colour scheme, except the black line indicates Permanent Snow & Ice. The polygons surrounding the trend lines indicate standard error. The black dots on the NARR panel (second from top) are air temperature averages measured at the Burwash Landing monitoring station. May 2008 was omitted because of missing data. Standard error for the air temperatures are encapsulated by the black dot.....173

Figure 6-3: June averages of maximum LST, average NARR, snow fraction and cloud fraction. The material is displayed in the same format as Figure 6-2.....174

Figure 6-4: July averages of maximum LST, average NARR, snow fraction and cloud fraction. The material is displayed in the same format as Figure 6-2.....175

Figures 6-5 to 6-13: (May 2000 to May 2008 respectively). Each figure is the four panel

plot of the distribution of Elevation, NARR temperature, Maximum LST, and Cloud fraction in 0.1 snow fraction bins, for the Tundra class within the elevation range of 1600 to 1700 m.....176-178

Figure 6-14: May average NARR temperature by 1,000 m elevation zone starting at 2,000 m for the icefield where average snow cover fraction was greater than 99% for all points.....179

Figure 6-15: Pacific Decadal Oscillation (PDO) for May (top) June (middle) and July (bottom) between 2000 and 2008.....180

CHAPTER ONE

The Relationship between Landscape Ecology, Climate and Snow Cover Decline in Altitudinal Tundra

Introduction

The air temperature in the Arctic is rising at a rate 2-3 times faster than the globe as a whole (IPCC, 2013), a phenomenon known as Arctic amplification. The 2014 Arctic Report Card (Overland et al., 2014) shows the annual average surface air temperature anomaly above 60 °N has become consistently warmer than the global average anomaly since 2000, such that the Arctic temperature signal has clearly decoupled from the lower latitude temperature trend. The global average temperature trend was believed to be in hiatus since 1998, largely due to the Pacific Ocean switching to the cold phase of the Pacific Decadal Oscillation (Dai et al., 2015). Recent evidence indicates that the hiatus was the result of observational biases, and that global surface temperature has continued increasing since 1998 (Karl et al., 2015). Globally, the air temperature trend shows an increase of 0.72 °C since 1950 (IPCC, 2013). Over the same period of time the Arctic temperature has risen at a rate greater than two times faster than global average (AMAP, 2012). Warming is coincident with North American snow cover reduction, with the pan-Arctic snow cover extent decreasing by 14% in May and 46% in June between 1967 and 2008 (Brown et al., 2010). Increasing air temperatures are the cause for changes in snow cover extent and duration (Euskirchen et al., 2006; Dye & Tucker, 2003).

Several studies have attempted to measure the surface warming that should be consistent with the large albedo decrease caused by a snow cover decrease (e.g., Chapin et al., 2005; Graversen et al., 2008). The local warming caused by snow cover loss is referred to as the Snow Albedo Feedback (SAF). The SAF is well established within the climate community. In fact General Circulation Models (GCM), which provide a mechanism through which our knowledge of climate dynamics is integrated and tested, include the snow albedo feedback, where albedo is usually parameterised as a monotonic function of snow age and depth (Bony et al., 2006). Output models show the northern hemisphere terrestrial SAF resulting from snow cover decrease are as important as that from sea ice decrease (Winton, 2006).

Research by mid-2000 couldn't produce conclusive evidence that Arctic amplification was an actual physical process in the polar cryosphere, indicating that it might have been the result of General Circulation Model imperfections (Serreze & Francis, 2006). At that time, the processes had not been completely resolved, but the weight of evidence suggested the effect was real (Serreze et al., 2009; Serreze & Barry, 2011). The uncertainty around Arctic amplification followed from two lines of evidence: (i) a high inter-model temperature variation and (ii) the low frequency climate variability over the observation record. The low frequency variability is seen in the climate record as warm events in the 1930's through 1950's (e.g. Jones & Moberg, 2003). Arctic amplification has been seen in climate models almost since their inception (Manabe & Bryan, 1969) and is very responsive to greenhouse gas forcing. The largest inter-model disagreement resulting from greenhouse gas forcing is found in northern high latitudes, where warming at the end of the 21st century ranges from 1.3 to 4 times

the global warming mean of surface air temperatures (Bony et al., 2006). Arctic climate warming is largely composed of two factors, meridional (latitudinal) heat transport and local heating (McGuire et al. 2006), and half of the temperature increase is related to increased heat transport from lower latitudes related to global warming (Langen & Alexeev, 2004).

The temperature rise in the Arctic since 2000 is convincing evidence for Arctic amplification. The current debate centres on the relative influences of local factors (i.e., SAF) versus external ones (i.e., latitudinal heat transport) in the magnitude of the amplification. There is an emerging trend in the literature that argues Arctic amplification is predominantly caused by heat transport from equatorial latitudes to high latitudes, and SAF plays only a minor role (e.g., Graversen et al., 2008). However, in the terrestrial Arctic the influence of local factors (such as snow cover decrease or vegetation change) on surface warming is still a matter of debate, largely because it is difficult to isolate local from external factors in observational data or reanalysis of modeled and downscaled data (Screen et al., 2012).

Arctic amplification partially results from positive feedbacks that are strongly linked to atmosphere and oceanic processes and warm air anomalies that are correlated to synoptic weather patterns. The water vapour transported from lower latitudes increases greenhouse warming in the Arctic, in addition to the intrinsic heat and momentum transfer. North of 55°N, Overland et al. (1996) found that large portions of the Boreal and low Arctic also export heat further north. Moreover, the temperature change resulting from the import of vapour in the Arctic is especially important during the winter because of the Arctic's relatively low concentration of water vapour. Additional

processes, such as the relatively stable Arctic winter climate, which typically displays a strong winter temperature inversion, are also important in Arctic amplification. The periodic advection of warm air from lower latitudes to the Arctic is often responsible for the major warm anomalies in the Arctic temperature record (McGuire et al., 2006). Enhanced westerly winds related to the positive phase of Arctic Oscillation/North Atlantic Oscillation is related to winter and spring warming of Siberia and Northern Europe (van Loon & Rogers, 1978). The Pacific North American pattern and Pacific Decadal Oscillation in positive phase can be used to explain some of the variability observed in the climate record and can also explain enhanced advection of warm air and winds into Alaska and Western Canada (McGuire et al., 2006). PDO is positive when the western Pacific, temperature anomalies north of 20 °N are cool and the east is warm, and the opposite geographic temperature anomaly regime is the negative phase. Over the last 40 years, ocean temperature indices have fluctuated, while the Arctic temperature trend has been predominantly positive, thus making a causal relationship between indices and warming tenuous.

Many feedback processes are at work in the climate system. Here we adopt the definition of a climate feedback as a process that dampens or amplifies the response of the climate to external forcing (NRC, 2003). Of these, the two most powerful are physical feedback processes, one positive and one negative. The balance between these two feedbacks plays a significant role in the stability of Arctic climate. The water vapour positive feedback is derived from the fact that as air temperature increases there is a non-linear associated increased capacity for water vapour. This effect is described by the Clausius-Clapeyron equation as the ability of the atmosphere to hold increasing

water vapour with increasing temperature and water vapour is efficiently absorbs longwave radiation. These two factors create a strong positive feedback between air temperature and atmospheric water vapour concentration (e.g., Dessler et al., 2008). The radiative feedback, which is negative, is caused by temperature increase, and is a direct result of the Stefan-Boltzmann equation and the earth's atmospheric greenhouse effect. Everything within the climate system, land cover and atmosphere alike, radiate to the fourth power of a body's temperature, modified by emissivity (or the black body correction). Thus, as surface temperature increases, the amount of long wave, radiation emitted increases to the fourth power. However, the atmosphere absorbs and redirects a fraction of this energy back to the earth's surface. Consequently, as the surface temperature increases, a dampening effect (or cooling at the top of atmosphere) caused by the increasing loss of radiation out of the atmosphere occurs.

In terms of physical feedbacks to the Earth's climate, water vapour increase, radiative cooling associated with temperature increase, troposphere lapse rate (dependent on the temperature of the atmosphere by altitude) , cloud, and surface albedo feedbacks are the largest in terms of magnitude (e.g., Dessler et al., 2008). The IPCC AR4 multi-model (GCM) mean and standard deviation for these global feedbacks integrated for the A1B emission scenario (approximately the doubling of equivalent CO₂ between 2000 and 2100) are $1.80 \pm 0.18 \text{ W m}^{-2} \text{ K}^{-1}$ for water vapour increase and radiative cooling for a temperature increase, $-0.84 \pm 0.26 \text{ W m}^{-2} \text{ K}^{-1}$ for lapse rate feedback, $0.69 \pm 0.38 \text{ W m}^{-2} \text{ K}^{-1}$ for cloud feedback and $0.26 \pm 0.08 \text{ W m}^{-2} \text{ K}^{-1}$ for albedo feedback (Soden and Held, 2006). By convention, a positive sign indicates an amplification of climate change, net energy flux is for the top-of-atmosphere (TOA),

and temperature is that of surface temperature change. The largest spread between models is for the lapse rate and cloud feedbacks, however all models show disagreement in the amount of feedback.

There are three reasons for the spread in climate model feedbacks (Bony et al., 2006). 1) Feedbacks are treated as partial derivatives in models that focus on global estimates, but the observations of feedbacks are not suitable for statistical isolation of single response variable because co-related variables cannot be kept constant. 2) Observation of feedbacks might not be directly, or wholly, responding to longer-term greenhouse gas forcing, where models are not constrained by such uncertainty. 3) The climate system is inherently complicated, with many variables at work simultaneously, including climate feedbacks. This complexity is not well encapsulated in climate models or our observation of the climate system. Regardless, GCMs are becoming more complicated and now incorporate many elements that are important to the Arctic, with better surface characterizations including biogeochemical and biogeographical elements, carbon cycle modelling and dynamic vegetation components (Bonan, 2008), but at relatively coarse resolutions.

Local heating in the Arctic

Any surface that is seasonally covered in snow, will also exhibit a large seasonal variation in reflected sunlight. When investigating surface energy budgets, broadband reflectance, or albedo, which is a unitless value between 0 and 1, is most commonly used. Albedo is defined as the ratio of outgoing short wave radiation to that of

incoming. Net shortwave radiation is the outgoing shortwave radiation subtracted from the incoming shortwave, or the amount of shortwave radiation that a surface absorbs, and is recorded in units of power per area. Shortwave radiation is the summation of all between the wavelengths of 0.1 μm to 5.0 μm , if widely defined, or between 0.2 μm and 3.0 μm if narrowly defined. The Earth and atmosphere both emit longwave radiation, which is usually defined as all energy between 4 μm to 40 μm , which is the range where the majority of the energy exists. However some energetic photons can still be detected up to 100 μm . Net radiation (Q^*) at the earth's surface is the incoming shortwave radiation minus the outgoing shortwave (K^*) plus the incoming longwave radiation minus the outgoing longwave (L^*). At the surface, three processes are largely responsible for dissipating Q^* . These are sensible heat (Q_H), latent heat (Q_E) and ground heat (Q_G) fluxes. Sensible heat is driven by the temperature differential between the surface and overlying air, where larger differentials lead to greater warming of the atmosphere. Latent heat is the energy required to change the phase of water and involves evaporation. Ground heat flux is the conductive heating of the Earth's surface, depending on a temperature gradient. In the Arctic and sub-Arctic the energy balance is strongly influenced by the seasonality of solar radiation. By the month of May, high latitudes receive more daily radiation than at mid-latitudes and the length of day is more important to total diurnal flux than maximum insolation (Eugster et al., 2000). The monthly average solar radiation for June near the Arctic Circle in Alaska and central Canada is 225-250 W m^{-2} (Eugster et al., 2000).

In the Arctic the large amounts of permanent snow and ice maintain a large albedo throughout the year (0.5 – 0.9), whereas the large amounts of tundra and inland lakes

show a massive range (0.1 – 0.9). Most of this range can be attributed to patchy snowmelt patterns where an area average includes both low albedo ground cover and high albedo snow. However a small amount of the spring snow albedo change is related to snow metamorphosis, which reduces the albedo of snow due to weathering and grain size change (Armstrong & Brun, 2008). The albedo decrease caused by spring snow melt can happen rapidly. Grenfell & Perovich (2004) report a spring tundra albedo decline of 0.8 to 0.15 over the period of two weeks. The conifer forests have year-round needle-leaved canopies that can partially mask snow-covered ground and typically have lower albedos decline (0.7 to 0.1) than annual or deciduous canopies. Albedo values are given in Thompson et al. (2004) and Eugster et al. (2000) and range between 0.155 – 0.19 for tundra to 0.10 – 0.11 for Spruce (*Picea*) conifer forest. Any reduction of terrestrial snow cover in the Arctic reveals a relatively low albedo ground surface regardless of its composition, which should lead to a strong snow-albedo feedback (SAF) with changing snow cover.

In terms of surface feedbacks, the most important are the snow and ice albedo feedbacks, but polar cloud processes, ocean heat and freshwater transport are also important aspects in cryosphere feedback processes. However the magnitudes of these processes are not yet fully quantified. The relative climate feedbacks of changing vegetation and snow-cover under climate change in northern latitudes are largely unknown, but some studies are starting to consider this topic (Chapin et al., 2005; Sturm et al., 2005). The model by Euskirchen et al. (2009) addresses the vegetation response to climate change. The model is driven by three global climate scenarios and three GCMs that provide a range of nine climate scenarios. The model demonstrates that

albedo decreases associated with snow cover loss is almost two orders of magnitude more important than albedo changes associated with increasing of above ground biomass. Further, summer warming in Alaska has been attributed to the increasing snow-free duration, where local heating of the atmosphere has increased by 3.3 W m^{-2} per decade (Chapin et al., 2005). The heating was attributed to snow cover decline because over the study period (1982-1999) cloud cover had been increasing in Alaska. Northern Hemisphere albedo feedback, which include changes from sea-ice cover and terrestrial snow cover, have been calculated as $0.3\text{-}1.1 \text{ W m}^{-2} \text{ K}^{-1}$, between 1979 and 2008 (Flanner et al., 2011). This range is larger than albedo feedback values presented by Soden & Held (2006) and those calculated from 18 CMIP3 models by Flanner et al. (2011).

The hydrology of Arctic tundra is strongly linked to snow. 40-80% of Arctic tundra's annual precipitation is derived from snow (Eugster et al., 2000), and growing season evapotranspiration is typically greater than growing season precipitation, leading to drying as the growing season progresses (Woo et al., 1992). After snowmelt the increase in Q_E/Q^* leads to the eventual decrease in soil moisture, which then reduces both Q_E/Q^* and increases albedo as the summer progresses (Eugster et al., 2000). The increased albedo causes a decrease in K^* and therefore a reduced Q^* . Exposed soil and sparsely vegetated tundra then transfer the remainder of Q^* into Q_H , because the transfer to Q_G is difficult because of reduced thermal conductivity of the dry soil. In deciduous vegetated tundra, a different energy portioning pathway is taken due to the larger portion of Q_E/Q^* throughout the growing season. As a general rule, for Arctic landscapes, the ratio of Q_E to Q^* decreases as the soil moisture gradient decreases and the ratio of Q_H to

Q^* increases as the soil moisture gradient decreases. Albedo also changes throughout the day, where the lowest value of albedo occurs slightly before solar noon and increases as solar elevation decreases (Eugster et al., 2000) and the diurnal progression of soil moisture (Ohmura, 1981). Vegetated tundra typically dampens this effect. Albedo increases as soils dry and standing water decreases, both of which are a common phenomenon observed in tundra over the course of the growing season.

Future summer time surface moisture is a largely a balance between precipitation and evaporative losses related to temperature increase during the longer, warmer, snow free period (e.g., Rouse et al., 1992; Rouse, 2000; Woo et al., 1992). A modelling study by Cook et al. (2014) has projected that large parts of the Arctic will likely become wetter this century, not drier like the majority of the middle latitude regions, because precipitation will outpace evaporative demand at high northern latitudes. However some studies have shown warming trends in some tundra areas are causing lakes to diminish in abundance and size (e.g., Smith et al., 2005; Andresen & Lougheed, 2015), indicating local factors such as permafrost degradation, may play a role in the future surface moisture balance in addition to changes in precipitation.

Snow depth in patchy Arctic tundra is a function of topography and vegetation cover. Thus as snow melts the thinnest snow melts first, exposing a dark albedo surface, whereas thicker snow packs found in wet tundra vegetation and shrubs, and leeward hill slopes persist later into the melt season (Liston, 1995). Snow trapping by shrubs (Sturm et al., 2001) creates local deep snow pockets. Sturm et al. (2005) quantified tundra albedo produced by thick stemmed shrub branches protruding above the snow surface caused a 30% reduction in albedo compared to snow surfaces. This value is significant

for winter and spring heating and snow pack evolution and is 2/3 the value of heating caused by a transition of tundra to forest. The increased abundance and height of shrubs in Polar Regions (Elmendorf et al., 2012) suggests that snow trapping will locally increase snow depth in a larger portion of the Arctic. Snow depth is difficult to detect remotely, especially in detail fine enough to detect snow depth resulting from vegetation patches and micro-topography, although snow cover is accessible. Some success has been achieved in recording snow water equivalent from passive microwave remote sensing. However this information is not particularly useful because no information about depth is available and the spatial resolution is typically coarse. In the field, snow is typically under-sampled by weather station snow sampling by 2-3 times due to wind redistribution and numerous trace events (Goodison, 1981; Woo et al., 1983).

Snow cover distribution in tundra is widely variable due to wind redistribution of snow (Liston and Sturm, 1998). Snow pack and resilient snow patch melting is a function of heat budget when snow occurs over permafrost – acts as a dampening agent because heat is extracted by the ground from overlying snow making snow cover persist longer than if covering a temperate surface (Marsh, 1991; Liston, 1995). Conversely, a reduction in snow and ice cover might reduce intensity of surface temperature inversions in the Arctic, resulting in warmer temperatures observed at ground level (McGuire et al., 2006).

Cloud Feedbacks

Clouds interact with the energy balance of the surface by blocking short wave radiation and through the emission of long wave radiation, with a net effect of cooling the planet. Cloud forcing on net radiation (Q^*) is largely related to L^* and can be either positive or negative depending on latitude. Latitudes greater than 50° display a negative cloud forcing, but L^* is affected much less at higher latitudes than in the tropical zone (Harrison et al., 1990). Increased cloud cover in the Arctic could mean an increase or decrease in Q^* . Regardless, the polar region is the most sensitive part of the globe to cloud forcing (Curry et al., 1996). A negative cloud forcing, which results in a cooling effect, results from low clouds, where high, ice-rich clouds, tend to trap long-wave radiation in amounts exceeding short-wave reduction, thus causing warming (Eugster et al., 2000). At present in the Arctic low-albedo summer surfaces tend to have negative cloud forcing, or increasing summer cloud reduces the amount of shortwave radiation more than the surface absorbs any increase in incident longwave, leading to a dampening of summer temperature increases (Wang & Key, 2003). However, there is still considerable debate about the sign and magnitude of cloud forcing on surface temperature, which is related to cloud albedo, optical depth, composition, and elevation. Comiso (2003) found that in the Arctic a 75% cloud fraction decrease using Advanced Very High Resolution Radiometer (AVHRR) derived infrared surface temperature by 0.5 K relative to clear sky. Varvov et al. (2004) found that model returns show a positive feedback associated with Arctic clouds, which accounted for approximately 40% of Arctic warming. Simulations by Holland & Bitz (2003) show similar results, with increase in Arctic cloud cover and Arctic amplification, especially in winter

months. Cloud cover in Arctic can affect the interpretation of satellite infrared surface temperature because snow-covered surfaces under cloud are warmer than under clear sky (Westermann et al., 2012).

Clouds also reduce minimum growing season albedo in tundra because diffuse light is more efficient penetrating into vegetation canopy and soil (Eugster et al., 2000, a reduction of approximately 0.02. Clouds also obscure the surface from remote observation, especially in perennially cloudy location such as the Arctic. Snow albedo is also slightly higher under cloudy skies, than clear (Armstrong & Brun, 2008).

Study Area

The northern tundra biome consists of two types: latitudinal and altitudinal. The latitudinal tundra biome covers an area of approximately 6,000,000 km² in a zone between the northern limits of the boreal forest and permanent seasonal ice cover (Lewis & Callaghan, 1976). This is in addition to the approximately 4,000,000 km² of vegetated altitudinal tundra (Körner, 2003) found at elevations below permanent snow-covered and non-vegetated areas above tree-line, of which a lesser amount is found in the sub-Arctic. My study site is located in the Kluane region of the southwest Yukon (Figure 1-1), which contains large amounts of permanent snow and ice and altitudinal tundra. The Yukon and Alaska, have warmed between 1 – 3 °C over the last 50 years (Arctic Climate Impact Assessment – ACIA, 2005; Snow, Water Ice, Permafrost in the Arctic - SWIPA, 2011). The southwest Yukon has seen declines in snow cover during both spring and fall. Between 1967 and 2007 Brown et al. (2010) found that snow cover

duration has been decreasing by approximately 12 days per decade averaged over both spring and fall in the study area.

Figure 1-2 shows the digital elevation map of Alaska, the Yukon and northern British Columbia. The study site is located near the end of North Pacific storm track (Blackmon, 1976), which exhibits a strong west to east direction. This is the predominant path which atmospheric water vapour enters northwest Canada (Smirnov et al., 1999). In recent years an increase in snow accumulation near Mount Logan has been attributed to secular changes in the Pacific Decadal Oscillation (Moore et al., 2002). The southwest Yukon is encapsulated within the St. Elias rain shadow, as can be seen by the massive decrease (greater than an order of magnitude) in total precipitation between the windward and leeward side of the St. Elias Icefield (Figure 1-3). The rain shadow is caused by the easterly atmospheric circulation of air masses, originating in the Arctic Ocean, Gulf of Alaska and the Bering Sea, which are controlled by the position of the Aleutian Low (Trenberth & Hurrell, 1994). One of the consequences of the small amount of precipitation and high topography is an absence of wet mesic tundra, which occupies flat, poorly drained sites, commonly found in more northern and coastal tundra.

Figure 1-4 shows a landscape classification (GLOBCOVER) completed in 2009 by the European Space Agency using MERIS 300 m resolution imagery (<http://due.esrin.esa.int/globcover/>) for Alaska, the Yukon and northern British Columbia. Of the 23 potential global land cover classes, 11 are found within the study area. These are Closed needle-leaved evergreen forest; Open needle-leaved deciduous or evergreen forest; Closed to open mixed broadleaved and needle-leaved forest; Mosaic

Forest-Shrubland/Grassland; Mosaic Grassland/Forest-Shrubland; Closed to open shrubland; Closed to open grassland; Sparse vegetation; Bare areas; Water bodies; Permanent snow and ice.

Of the 11 classes contained within the Kluane study area, three are of special importance because of their homogeneous nature and spring snow cover dynamics: Permanent snow and ice (Icefield), Sparse Vegetation (Tundra) and Open needle leaved deciduous or evergreen forest (Conifer). A representative picture of each is shown in Figures 1-5, 1-6, 1-7.

Although this area has seen tree-line advance over the past century (Danby & Hik, 2007), the extent of modern (< 40 years) vegetation change above tree-line has been small (Danby et al., 2011). In the past 20 years spruce beetles killed many of the mature low elevation spruce trees (Garbutt, 2007), however the density of the infestation was small, and the majority of the infestation was north and east of the Kluane study area. The Icefields are experiencing a large decline in glaciated area and volume (e.g., Berthier et al., 2010), but these differences are reflected in the snow cover used here. In terms of contemporary changes, the southwest Yukon has seen an increasing trend in spring temperature, but has at the same time has seen PDO values that alternate between negative and positive throughout the study period (Figure 1-8). The May air temperature trend has increased by 0.5 °C / decade between 1967 and 2014, and by 0.4 °C / year between 2000 and 2007 because May 2000 was one of the coldest on record and 2004 and 2005 the two warmest on record. The portion of the study area that is not glaciated is mostly in the Sporadic Discontinuous (10 – 50 %) permafrost zone.

Extensive Discontinuous (50 – 90 %) permafrost is found in a limited amount immediately north and east of Kluane Lake (permafrost.gov.yk.ca).

Observations & Measurements

The Arctic is expansive, largely hard to access and has a limited amount of heterogeneously placed meteorological observing stations. These lead to data scarcity and observational bias. The Kluane region of the southwest Yukon is no exception. Two of the 11 Environment Canada meteorological stations are found in the study region, both at valley bottom and at airports (Burwash Landing and Haines Junction). These stations, in addition to the stations found at Carmacks and Whitehorse provide hourly air temperature, plus ground observations of cloud cover.

Satellite remote sensing has become a key tool in observing the Arctic, but the short period of record, interpretation of imagery and inconsistency in observation (often due to cloud cover) are limitations. In this thesis we use satellite data originating from the MODerate resolution Imaging Spectroradiometer (MODIS), aboard the Aqua and Terra platforms. From these satellites we obtain snow cover, cloud cover and infrared Land Surface Temperature (LST). In the multi-sensor comparison of snow cover, Brown et al. (2010) conclude that the high-resolution MODIS snow cover was one of the best performing products. Downscaling of coarse resolution climate re-analysis products can also provide detailed regional information about difficult to access areas. Two independent temperature downscaling methodologies were used for this thesis,

dynamical and statistical. The technical details regarding the generation and processing of the data streams appear in the following chapters.

Objectives

The overarching objective of this thesis was to measure the strength of albedo temperature feedbacks at the surface in the mountainous Kluane and St. Elias region of southwest Yukon. The experimental design exploits the large elevational gradient found in the study area to differentiate the influence vegetation, snow cover, cloud cover and elevation had on temperature change; Figure 1-9 represents this objective as conceptual diagram. In the left panel of Figure 1-9, the elevational distribution of land cover in the southwest Yukon is displayed, where permanent snow and ice (a) occupy the highest elevation, tundra (b) the middle and conifer forest (c) the bottom. Incoming shortwave radiation is modulated by daytime cloud cover, such that the strength of the snow albedo feedback is also affected. The middle panel is the planometric view of elevational cross section, which is divided into generalized grid cells consistent with remote sensing of snow cover or surface temperatures. Time one (t_1) and time two (t_2) are the repeat visualisations of the landscape units and represents successive spring seasons. The lowest elevation land covers are largely devoid of snow earlier in the spring, unlike alpine land covers, and the highest elevation land cover (Ice field) is permanently covered in snow and ice. This differential pattern in spring snow cover is exploited to identify the influence of snow cover changes over successive years, where a simultaneous comparison of temperature can be conducted for land covers that have no snow cover, complete and unchanging snow cover and changing snow cover. This

design provides a mechanism to separate the external forcing from the local feedbacks related to snow cover change. The right panel is the spatially integrated temperature time series for the landscape units previously described where the capital T represents a measure of surface temperature. The top right and bottom right trends are hypothesised to increase at an equivalent rate as neither is displaying snow cover change. The middle right trend shows a rapidly increasing temperature trend caused by the large decrease in albedo related to snow cover decline in tundra land cover.

A schematic outline of this thesis is presented in Figure 1-10. Chapter One presented background material, provided an overview of the experimental design and introduced the southwest Yukon study site. Chapter Two is an error analysis of MODIS infrared thermal Land Surface Temperature related to cloud cover and snow cover. Chapters Three and Four provide validation of the temperature products used in this thesis, especially for the high elevation areas. These chapters are necessary because few examples of high elevation validation occur in the literature. Chapter Five is a field experiment on the albedo dynamics of tundra vegetation. This chapter is required to discriminate the albedo differences produced from snow cover change from those of vegetation phenology. Chapter Six is an assessment of the snow cover decline feedback to climate using the previously discussed experimental design and validated temperature products. Chapter Seven serves as a conclusion and discussion of further work.

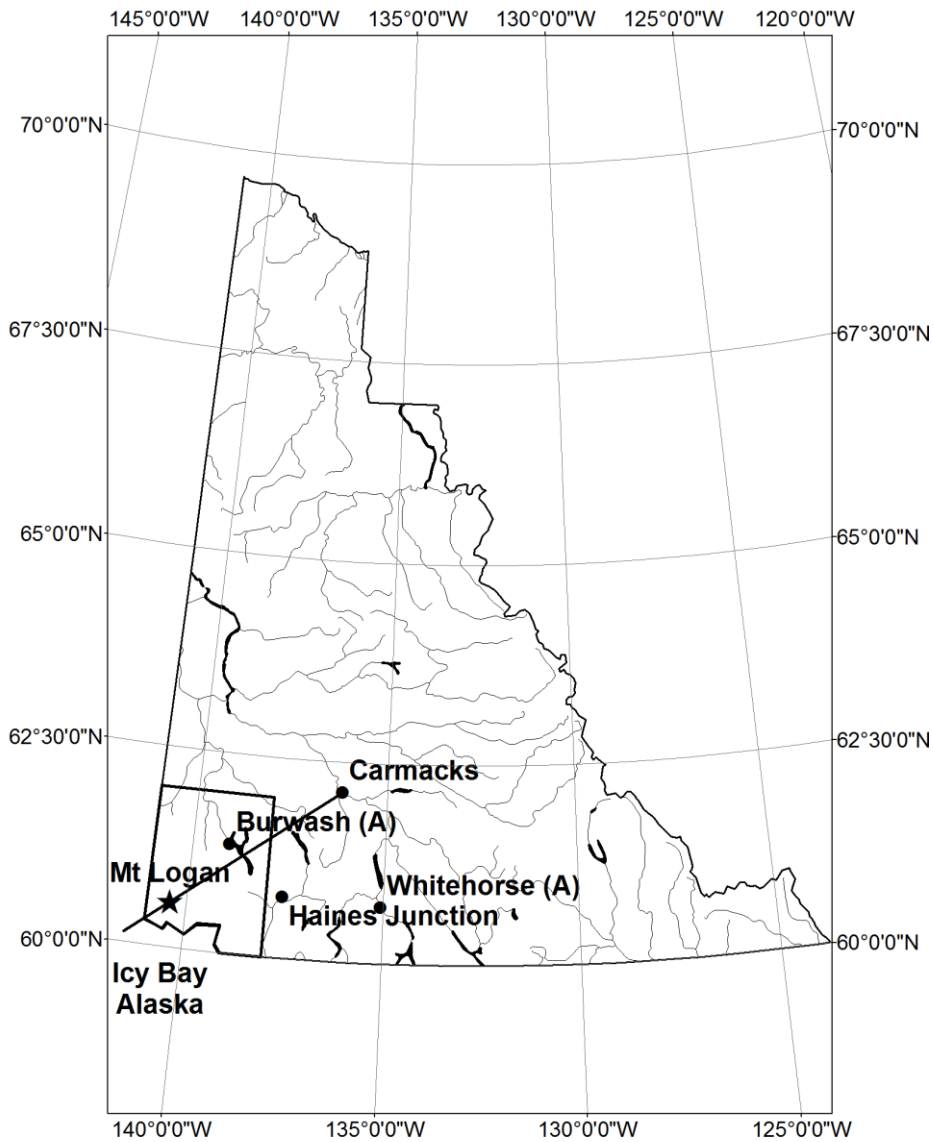


Figure 1-1: The Yukon Territory, Canada, including major rivers and lakes. The smaller outline in the bottom left of the figure (southwest) is the Kluane study area. The star marks Mount Logan and the dendritic shape marks Kluane Lake. The line marks a cross sectional elevation profile, between sea-level at Icy Bay, Alaska, and Carmacks, Yukon (see Figure 1-3). Solid circles indicate locations of Environment Canada meteorological monitoring stations.

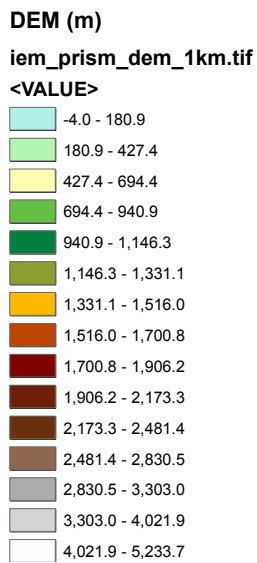
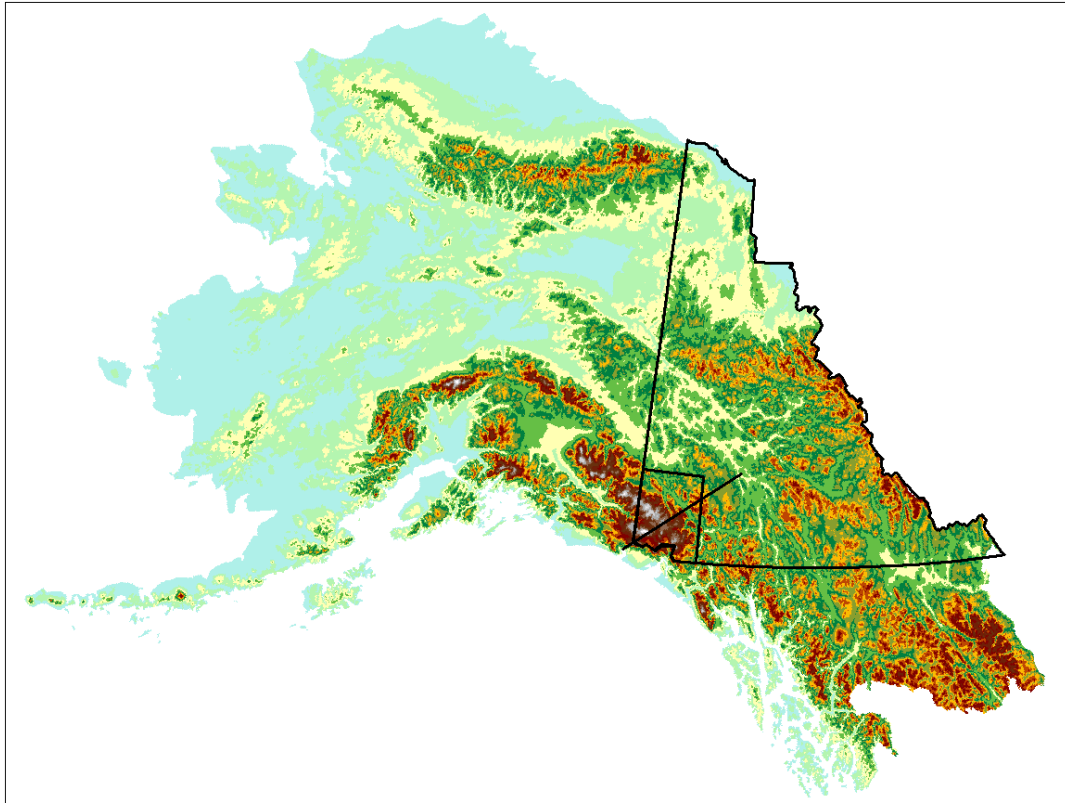


Figure 1-2: Digital Elevation Map (m) covering Alaska, the Yukon and northern British Columbia. The smaller outline in the bottom right of the figure (southwest) is the Kluane study area. The line marks a cross sectional elevation profile displayed in Figure 1-3.

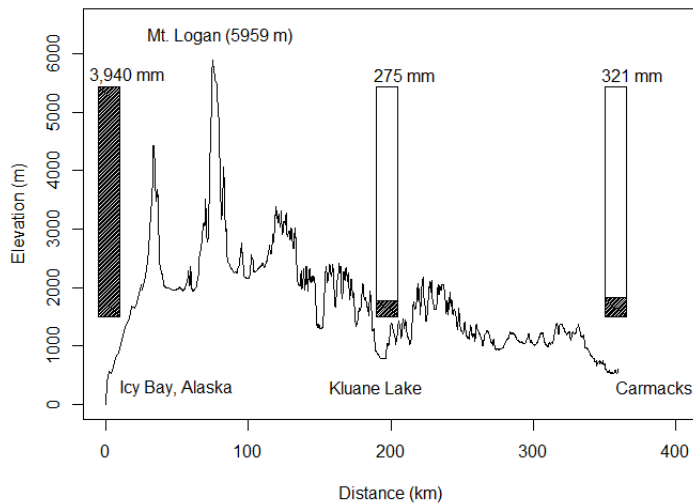
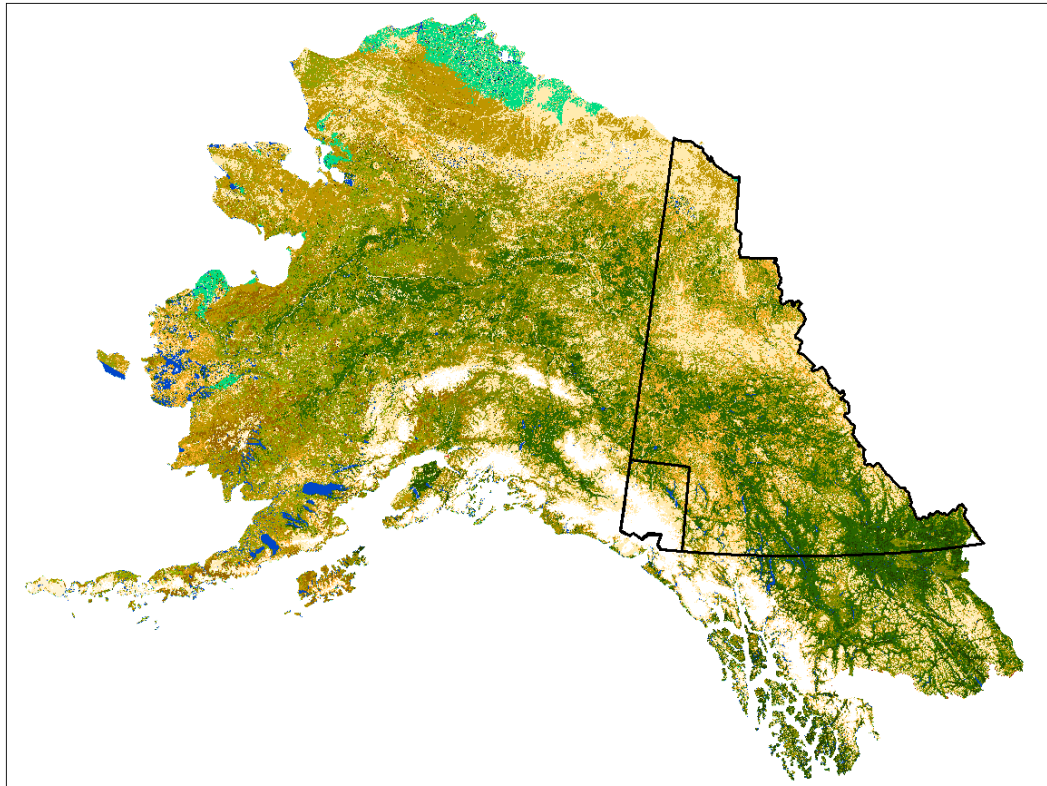


Figure 1-3: Elevation transect between Icy Bay Alaska and Carmacks Yukon. Annual average total precipitation is also included. Precipitation for Icy Bay was recorded at Yakutat, Alaska (approximately 100 km south east) where an average of 3,940 mm of total precipitation occurred. Kluane lake precipitation was measured at the Burwash Landing. The Carmacks precipitation was measured at Pelly Crossing (approximately 90 km north). The precipitation is demarked as the shaded region areas in the bars of the total that falls at Icy Bay (shaded plus open for Kluane Lake and Carmacks). The precipitation data originate with the National Ocean and Atmospheric Administration (NOAA) and are 1981 – 2010 averages.



Legend

- 11 - Irrigated croplands
- 14 - Rainfed croplands
- 20 - Mosaic Croplands/Vegetation
- 30 - Mosaic Vegetation/Croplands
- 40 - Closed to open broadleaved evergreen or semi-deciduous forest
- 50 - Closed broadleaved deciduous forest
- 60 - Open broadleaved deciduous forest
- 70 - Closed needleleaved evergreen forest
- 90 - Open needleleaved deciduous or evergreen forest
- 100 - Closed to open mixed broadleaved and needleleaved forest
- 110 - Mosaic Forest-Shrubland/Grassland
- 120 - Mosaic Grassland/Forest-Shrubland
- 130 - Closed to open shrubland
- 140 - Closed to open grassland
- 150 - Sparse vegetation
- 160 - Closed to open broadleaved forest regularly flooded (fresh-brackish water)
- 170 - Closed broadleaved forest permanently flooded (saline-brackish water)
- 180 - Closed to open vegetation regularly flooded
- 190 - Artificial areas
- 200 - Bare areas
- 210 - Water bodies
- 220 - Permanent snow and ice
- 230 - No data

Figure 1-4: GLOBCOVER land cover product covering Alaska, the Yukon and northern British Columbia. The Yukon and the smaller Kluane study area are marked by the black outlines.



Figure 1-5: Sparse vegetation dry tundra in the Ruby Range. Note the snow patches and clouds in the background.



Figure 1-6: Low elevation conifer (*Picea glauca*) near Kluane Lake Research Station at the south end of Kluane Lake looking east into the Ruby Range. Note the snow cover at higher elevation in the Ruby Range.



Figure 1-7: Mount Logan, the highest peak (5,959 m) in the St. Elias Mountains. This image represents the GLOBCOVER Permanent Snow & Ice category.

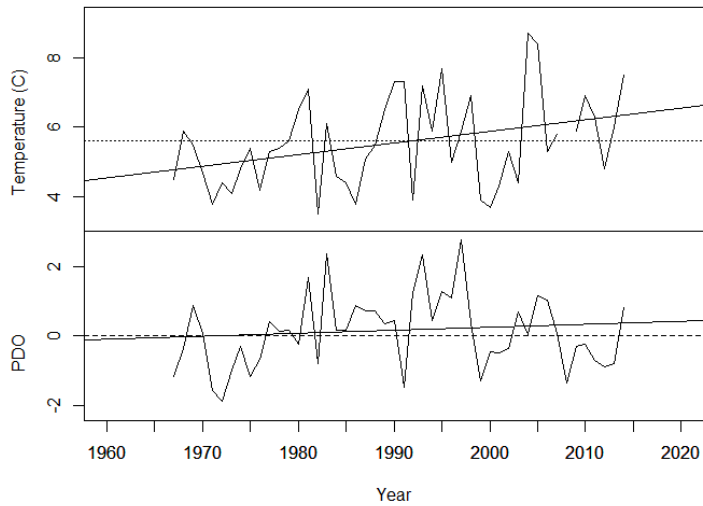


Figure 1-8: May average air temperature recorded at Burwash Landing Environment Canada Station. The lower plot shows May monthly averages of Pacific Decadal Oscillation (PDO). The horizontal dotted line in the Temperature plot is the 1967-2014 May average air temperature (5.6 °C). The May air temperature trend has increased by 0.5 °C / decade between 1967 and 2014. The May air temperature trend has increased by 0.4 °C / year between 2000 and 2007. The solid lines indicate the trend. Note that PDO is evenly distributed between positive and negative phases between 2000 and 2008.

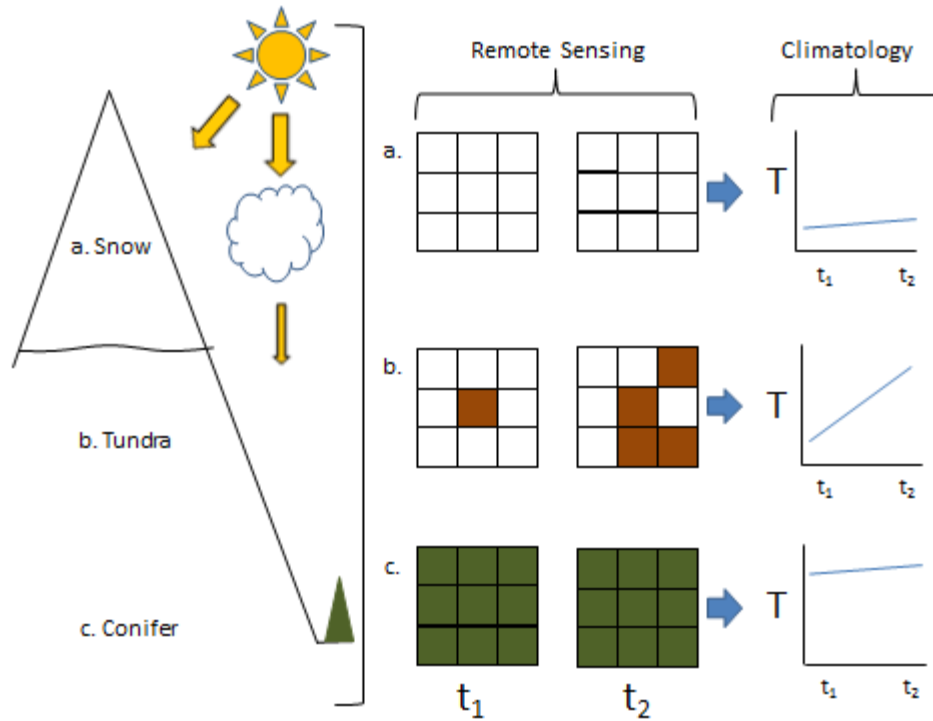


Figure 1-9: Conceptual diagram of elevational dependent landscape processes related to spring snow cover derived albedo change for a) Permanent Snow and Ice, b) Tundra, and c) Conifer forest. The left panel represents the land cover related to elevation, the middle panel represents remotely sensed grid cell level changes in albedo (due to snow cover) and the right panel represents hypothetical changes in temperature (T) related to annual spring time steps t_1 and t_2 . The rate of temperature increase is the same for the land covers at the top and bottom and is a measure of external heat import only because there are no surface albedo changes. The temperature curves are offset as a function of the adiabatic lapse rate. The middle Tundra land cover is experiencing snow cover loss,, suggesting that the temperature response will be a function of both external forcing and local feedback.

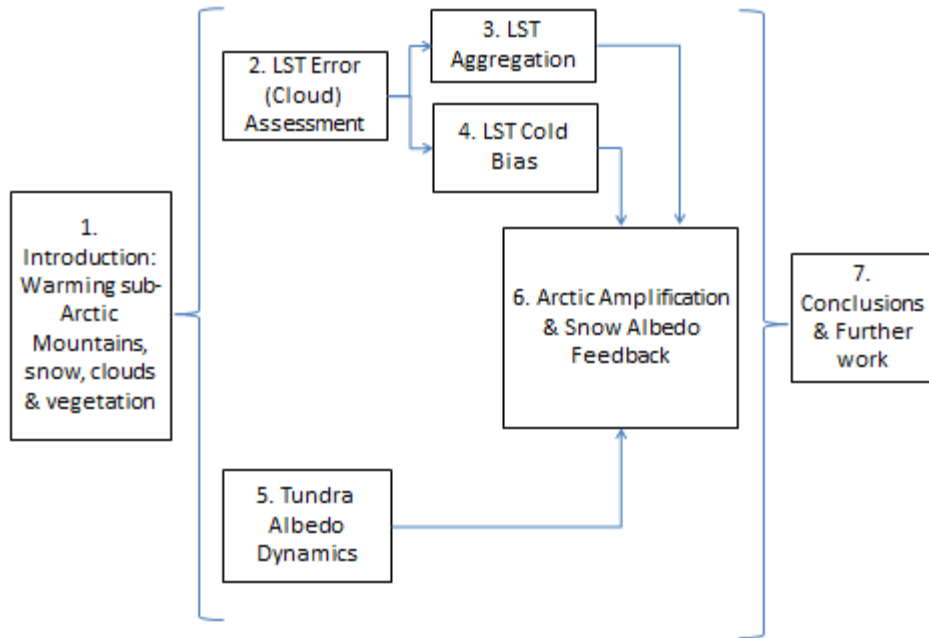


Figure 1.10: The conceptual relationship among the seven chapters in this thesis, which collectively explore the processes of elevation dependent landscape processes in rapidly warming sub-Arctic mountains, by examining the influences of snow, temperature and vegetation. LST refers to MODIS-derived Land Surface Temperature.

References

- ACIA (Arctic Climate Impact Assessment) Report. (2005). Impacts of a warming Arctic. UK: Cambridge University Press 146 pp.
- AMAP (Arctic Monitoring and Assessment Programme). (2012). SWIPA overview report. In: Arctic Climate Issues 2011: Changes in Arctic Snow, Water, Ice and Permafrost (eds. Shearer, R., Wrona, F., Klint, M., Larsen, H., Skovgaard, O., Mahonen, O., Jensson, H., Dovle, P., Tsaturov, Y., Lundeberg, T., Armstrong, T., Solbakken, J.-I., pp. 30-40. Oslo, Norway.
- Andresen, C.G., & Lougheed, V.L. (2015). Disappearing Arctic tundra ponds: Fine-scale analysis of surface hydrology in drained thaw lake basins over a 65 year period (1948-2013). *Journal of Geophysical Research Biogeosciences*, **120**, 466-479.
- Armstrong, R. L. & Brun, E. (editors). (2008). Snow and Climate. Cambridge University Press, Cambridge, U.K.
- Beringer, J., Chapin F. S., Thompson C. C., & McGuire, A. D. (2005). Surface energy along a tundra-forest transition and feedbacks to climate. *Agricultural and Forest Meteorology*, **131**, 143-161.
- Berthier, E., Schiefer, E., Clarke, G. K. C., Menounos, B., & Remy, F. (2010). Contribution of Alaskan glaciers to sea-level rise derived from satellite imagery. *Nature Geoscience*, **3**, doi:10.1038/NGEO737.
- Blackmon, M. L. (1976). Climatological spectral study of 500 Mb geopotential height of northern hemisphere. *Journal of Atmospheric Science*, **33**, 1607-1623.
- Bonan, G. B. (2008). Forests and Climate Change: Forcings, Feedbacks, and the Climate Benefits of Forests. *Science*, **320**, 1444-1449.

- Bony, S., Colman, R., Kattsov, V. M., Allan, R. P., Bretherton, C. S., Dufresne, J. L., Hall, A., Hallegatte, S., Holland, M. M., Ingram, W., Randall, D. A., Soden, B. J., Tselioudis, G., & Webb, M. J. (2006). How well do we understand and evaluate climate change feedback processes? *Journal of Climate*, **19**, 3445-3482.
- Brown, R., Derksen, C., & Wang, L. (2010). A multi-dataset analysis of variability and change in Arctic spring snow cover extent. *Journal of Geophysical Research*, **115**, D16111, doi:10.1029/2010JD013975.
- Chapin, F. S., Sturm, M., Serreze, M. C., McFadden, J. P., Key, J. R., Lloyd, A. H., McGuire, A. D., Rupp, T. S., Lynch, A. H., Schimel, J. P., Beringer, J., Chapman, W. L., Epstein, H. E., Euskirchen, E. S., Hinzman, L. D., Jia, G., Ping, C.-L., Tape, K. D., Thompson, C. D. C., Walker, D. A., & Welker, J. M. (2005). Role of land-surface changes in Arctic summer warming. *Science*, **310**, 657-660.
- Comiso J. C. (2003). Warming trends in the Arctic from clear sky satellite observations. *Journal of Climate*, **16**, 3498-3510.
- Cook, B.I., Smerdon, J.E., Seager, R., & Coats, S. (2014). Global warming and 21st century drying. *Climate Dynamics*, **43**, 2607-2627.
- Curry, J. A., Rossow, W. B., Randall, D., & Schramm, J. L. (1996). Overview of Arctic cloud and radiation characteristics. *Journal of Climate*, **9**, 1731-1764.
- Dai, A., Fyfe, J.C., Xie, S.-P., & Dai, X. (2015). Decadal modulation of global surface temperature by internal climate variability. *Nature Climate Change*, doi: 10.1038/NCLIMATE2605.
- Danby, R. K., & Hik, D. S. (2007). Variability, contingency and rapid change in recent subArctic alpine tree line dynamics. *Journal of Ecology*, **95**, 352-363.

- Danby, R.K., Koh, S., Hik, D.S., & Price, L.W. (2011). Four decades of plant community change in the alpine tundra of southwest Yukon, Canada. *AMBIO* **40**, 660-671.
- Dessler, A. E., Zhang, Z., & Yang, P. (2008). Water-vapor climate feedback inferred from climate fluctuations, 2003-2008. *Geophysical Research Letters*, **35**, doi: 10.1029/2008GL035333.
- Dye, D.G., & Tucker, C.J. (2003). Seasonality and trends in snow-cover, vegetation index, and temperature in northern Eurasia. *Geophysical Research Letters*, **30**, 1405, doi:10.1029/2002GL016384.
- Elmendorf, S. C., Henry, G. H., Hollister, R. D., Björk, R. G., Boulanger-Lapointe, N., Cooper, E. J., ... & Wipf, S. (2012). Plot-scale evidence of tundra vegetation change and links to recent summer warming. *Nature Climate Change*, **2**, 453-457.
- Eugster, W., Rouse, W. R., Pielke, R. A., McFadden, J. P., Baldocchi, D. D., Kittel, T. G. F., Chapin, F. S., Liston, G. E., Vidale, P. L., Vaganov, E., & Chambers, S. (2000). Land-atmosphere energy exchange in Arctic tundra and boreal forest: available data and feedbacks to climate. *Global Change Biology*, **6**, 84-115.
- Euskirchen, E. S., McGuire, A. D., Chapin, F. S., Yi, S., & Thompson, C. C. (2009). Changes in vegetation in northern Alaska under scenarios of climate change, 2003-2100: implications for climate feedbacks. *Ecological Applications*, **19**, 1022-1043.
- Euskirchen, E. S., McGuire, A. D., Kicklighter, D. W., Zhuang, Q., Clein, J. S., Dargaville, R. J., Dye, D. G., Kimball, J. S., McDonald, K. C., Melillo, J. M., Romanovsky, V. E., & Smith, N. V. (2006). Importance of recent shifts in soil thermal

- dynamics on growing season length, productivity, and carbon sequestration in terrestrial high-latitude ecosystems. *Global Change Biology*, **12**, 731-750.
- Flanner, M. G., Shell, K. M., Barlage, M., Pervich, D. K., & Tschudi, M. A. (2011). Radiative forcing and albedo feedback from the Northern Hemisphere cryosphere between 1979 and 2008. *Nature Geoscience*, **4**, 151-155.
- Garbutt, R. (2008). Yukon Forest Health Report 2007. Government of Yukon, Energy, Mines and Resources, Forest Management Branch. ISSN: 1708-9360.
- Goodison, B. E. (1981). Compatibility of Canadian snowfall and snow cover data. *Water Resources Research*, **17**, 893-900.
- Graversen, R., Mauritsen, T., Tjernström, M., Källén, E., & Svensson, G. (2008). Vertical structure of recent Arctic warming. *Nature*, **451**, 53-56.
- Grenfell, T. C., & Perovich, D. K. (2004). Seasonal and spatial evolution of albedo in a snow-ice-land-ocean environment. *Journal of Geophysical Research*, **109**, C01001, doi:10.1029/2003JC001866.
- Harrison, E. F., Minnis, P., Barkstrom, B. R., Ramanathan, V., Cess, R. D. & Gibson, G. G. (1990). Seasonal variation of cloud radiative forcing derived from the Earth Radiation Budget Experiment. *Journal of Geophysical Research*, **95**, 18687-18703.
- Holland, M. M., & Bitz, C. M. (2003). Polar amplification of climate change in coupled models. *Climate Dynamics*, **21**, 221-232.
- Houghton, J. T., Ding, Y., Griggs, D. J., Noguera, M., van der Linden, P. J., Dai, X., Maskell, K., & Johnson, C. A., Eds., 2001: Climate Change 2001: The Scientific Basis. Cambridge University Press, 944 pp.

- Intergovernmental Panel on Climate Change (IPCC) (2013). Fifth Assessment Report. In: Climate Change 2013 – Working Group 1: The Physical Science Basis (eds Stocker TF, Qin D, Plattner G-K, Tignor M, Allen SK, Boschung J, Nauels A, Xia Y, Bex V, Midgley PM), pp.130-194; 1257-1258. Cambridge University Press, Cambridge, UK.
- Jones, P. D., & Moberg, A. (2003). Hemispherical and large scale surface air temperature variations: an extensive revision and an update to 2001. *Journal of Climate*, **16**, 206-223.
- Karl, T.R., Arguez, A., Huang, B., Lawrimore, J.H., McMahon, J.R., Menne, M.J., Peterson, T.C., Vose, R.S., & Zhand, H.-M. (2015). Possible artifacts of data biases in the recent global surface warming hiatus. *Science*, **348**, 1469-1472.
- Körner, C. (2003). *Alpine plant life: functional plant ecology of high mountain ecosystems; with 47 tables*. Springer Science & Business Media.
- Langen, P. L., & Alexeev, V. A. (2004). Multiple equilibria and asymmetric climates in the CCM3 coupled to an oceanic mixed layer with thermodynamic sea ice. *Geophysical Research Letters*, **31**, doi: 10.1029/2003GL019039.
- Lewis, M. C., & Callaghan, T. V. (1976). Tundra. Vegetation and the Atmosphere. Vol. 2. J. L. Monteith, Ed. Academic Press, 399-433.
- Liston, G. E. (1995). Local advection of momentum, heat, and moisture during the melt of patchy snow covers. *Journal of Applied Meteorology*, **34**, 1705-1715.
- Liston, G. E., & Sturm, M. (1998). A snow-transport model for complex terrain. *Journal of Glaciology*, **44**, 1705-1715.

- Manabe, S., & Bryan, K. (1969). Climate calculations with a combined ocean-atmosphere model. *Journal of Atmospheric Science*, **26**, 786-789.
- Marsh, P. 1991. Water flux in melting snow covers. In: *Advances in Porous Media* (ed. Corapcioglu MY), Vol. 1, pp. 61-124. Elsevier, Amsterdam.
- McGuire, A. D., Chapin F. S., Walsh, J. E., & Wirth, C. (2006). Integrated Regional Changes in Arctic Climate Feedbacks: Implications for the Global Climate System. *Annual Review of Environment and Resources*, **31**, 61-91.
- Moore, G. W. K, Holdsworth, G., & Alverson, K. (2002). Climate change in the North Pacific region over the past three centuries. *Nature*, **420**, 401-403.
- Murphy, J., Sexton, D., Barnett, D., Jones, G., Webb, M., Collins, M., & Stainforth, D. (2004). Quantification of modelling uncertainties in a large ensemble of climate change simulations. *Nature*, **430**, 768-772.
- National Research Council – of the National Academics (NRC). (2003). *Understanding Climate Change Feedbacks*. National Academic Press, 152pp.
- Ohmura, A. 1981. *Climate and Energy Balance of Arctic Tundra*. Zürcher Geographische Schriften/ETH Zürich, Switzerland.
- Overland, J. E., Turet, P., & Oort, A. H. (1996). Regional variation of moist static energy flux into the Arctic. *Journal of Climate*, **9**, 54-65.
- Overland, J., Hanna, E., Hanssen-Bauer, I., Kim, S.-J., Walsh, J., Wang, M., & Bhatt, U. S. (2014). Arctic Report Card 2014 – Air Temperature.
www.Arctic.noaa.gov/reportcard/
- Polyakov, I. D., Alekseev, G. V., Bekryaev, R. V., Bhatt, U., Colony, R., Johnson, M. A., Karklin, V. P., Makshtas, A. P., Walsh, D., & Yulin, A. V. (2002). Observationally

- based assessment of polar amplification of global warming. *Geophysical Research Letters*, **29**, doi:10.1029/2001GL011111.
- Rouse, W. R. (2000). The energy and water balance of high latitude wetlands: controls and extrapolations. *Global Change Biology*, **6**, 59-68.
- Rouse, W. R., Carlson, D. W., & Weick, E. J. (1992). Impacts of summer warming on the energy balance of wet tundra. *Climate Change*, **22**, 305-326.
- Screen, J.A., Deser, C., & Simmonds, I. (2012). Local and remote controls on observed Arctic warming. *Geophysical Research Letters*, **39**, L10709, doi:10.1029/2012GL051598.
- Serreze, M. C., & Francis, J. A. (2006). The Arctic amplification Debate. *Climate Change*, **76**, 241-264.
- Serreze, M. C., Barrett, A., Stroeve, D., Kindig, D., & Holland, M. (2009). The emergence of surface-based Arctic amplification, *Cryosphere*, **3**, 11-19.
- Serreze, M., & R. Barry. (2011). Processes and impacts of Arctic amplification: A research synthesis. *Global and Planetary Change*, **77**, 85-96.
- Smirnov, V. V., & Moore, G. W. K. (1999). Spatial and temporal structure of atmospheric water vapor transport in the Mackenzie River basin. *Journal of Climate*, **12**, 681-696.
- Smith, L.C., Sheng, Y., MacDonald, G.M., & Hinzman, L.D. (2005). Disappearing arctic lakes. *Science*, **308**, 1429.
- Snow, Water, Ice, Permafrost in the Arctic (SWIPA) (2011) Accessed 22 April 2013, <http://amap.no/swipa>.

- Soden, B. J. & Held, I. M. (2006). An assessment of climate feedbacks in coupled ocean-atmosphere models. *Journal of Climate*, **19**, 3354-3360.
- Stainforth, D. A., Aina, T., Christensen, C., Collins, M., Faull, N., Frame, D. J., Kettleborough, J. A., Knight, S., Martin, A., Murphy, J. M., Piani, D., Sexton, D., Smith, L. A., Spicer, R. A., Thorpe, A. J., & Allen, M. R. (2005). Uncertainty in predictions of the climate response to rising levels of greenhouse gases. *Nature*, **433**, 403-406.
- Sturm, M., Racine, C., & Tape, K. (2001). Climate change: increasing shrub abundance in the Arctic. *Nature*, **411**, 546-547.
- Sturm, M., McFadden, J. P., Liston, G. E., Chapin F. S., Racine, C. H., & Holmgren, J. (2001). Snow – Shrub Interactions in Arctic Tundra: A Hypothesis with Climactic Implications. *Journal of Climate*, **14**, 336-344.
- Sturm, M., Douglas, T., Racine, C., & Liston, G. E. (2005). Changing snow and shrub conditions affect albedo with global implications. *Journal of Geophysical Research*, **110**, doi: 10.1029/2005JG000013.
- Thompson, C., Beringer, J., Chapin, F. S., & McGuire, A. D. (2004). Structural complexity and land-surface energy exchange along a gradient from Arctic tundra to boreal forest. *Journal of Vegetation Science*, **15**, 397-406.
- Trenberth, K.E., & Hurrell, J.W. (1994). Decadal atmosphere-ocean variability in the Pacific. *Climate Dynamics*, **9**, 303–309.
- Van Loon, H., & Rogers, J. C. (1978). The seesaw in winter temperatures between Greenland and northern Europe. Part I: General description. *Monthly Weather*

Review, **106**, 296-310.

Varvus, S. (2004). The impact of cloud feedbacks on Arctic climate under greenhouse gas forcing. *Journal of Climate*, **17**, 603-615.

Wang, X. & Key, J. R. (2003). Recent trends in Arctic surface, cloud, and radiation properties from space. *Science*, **299**, 1725-1728.

Westermann, S., Langer, M., & Boike, J. (2012). Systematic bias of average winter-time land surface temperatures inferred from MODIS at a site on Svalbard, Norway. *Remote Sensing of Environment*, **118**, 162-167.

Winton, M. (2006). Amplified Arctic climate change: What does surface albedo feedback have to do with it? *Geophysical Research Letters*, **33**, L03701, doi:10.1029/2005GL025244.

Woo, M. K., Heron, R., Marsh, P., & Steer, P. (1983). Comparison of weather station snowfall with winter snow accumulation in high Arctic basins. *Atmosphere-Oceans*, **21**, 312-325.

Woo, M. K., Lewkowicz, A. G., & Rouse, W. R. (1992). Response of the Canadian permafrost environment to climatic change. *Physical Geography*, **134**, 287-317.

CHAPTER TWO

Evaluating cloud contamination in clear-sky MODIS Terra daytime Land Surface Temperatures using ground-based meteorology station observations¹

Introduction

Infrared derived Land Surface Temperature (LST) is a key variable for understanding many surface processes, which makes the accurate determination of LST values from satellites a major goal. However, the accurate detection of LST with passive remote sensing is often modified by cloud contamination. The Moderate Resolution Imaging Spectroradiometer (MODIS) on board the Terra and Aqua satellites is less susceptible to cloud contamination than previous sensors because of the high frequency of coverage, 36 relatively narrow spectral bands and relatively high spatial resolution (250 m, 500 m or 1000 m depending on the spectral band). MODIS uses 14 spectral band radiance values to evaluate atmospheric contamination and determine whether scenes are affected by cloud shadow (Ackerman et al., 1998). In general, cloud contamination of MODIS imagery is largely related to cloud edges, optically thick aerosols and difficult identifying cloud types, such as thin clouds (e.g., Ackerman et al., 1998; Platnick, et al., 2003). The MODIS Collection 5 cloud detection algorithm has

¹ A version of this chapter was published in the *Journal of Climate* as: Williamson, S. N., Hik, D. S., Gamon, J. A., Kavanaugh, J. L., & Koh, S. (2013). Evaluating cloud contamination in clear-sky MODIS Terra daytime land surface temperatures using ground-based meteorology station observations. *Journal of Climate*, 26(5), 1551-1560.

been assessed against lidar sensor returns by Ackerman et al. (2008) with a high (~85 %) degree of success. Similar levels of success in cloud detection have been reported for daytime MODIS cloud mask when compared to Multi-angle Imaging Spectroradiometer (MISR) data over the Arctic (Shi et al., 2007). The imperfect cloud detection indicates there is undetected cloud contamination in “clear-sky” MODIS imagery.

Validation for the MODIS LST product has been conducted on Collection 4 nighttime data (Wang et al., 2008). The use of nighttime data reduces scaling issues related to discrete thermal measurements made within the MODIS grid cell. The effects of relative humidity, wind speed, soil moisture, air temperature and sensor view zenith angle on LST has been explored by Wang et al. (2008) for nighttime temperatures. Sensor view zenith angle showed a weak influence on error generation of swath data; the other variables showed no influence. Wan (2008) found that collection 5 MODIS LST products have accuracy better than 1 K in 39 of 47 cases that were compared to in-situ observations; the RMS of differences is reported to be 0.7 K for the full suite of cases. Langer et al. (2010) compared thermal infrared images collected in the field within 10 minutes of MODIS LST observations, over wet polygonal tundra, located at 72° 22' N in Siberia, using up to 18 daily swaths from Aqua and Terra for July to September 2008. They concluded that sub-pixel water bodies have a moderating impact on growing season daytime LST and must be accounted for in determining LST over tundra, and improved cloud cover masking and gap filling techniques are required to improve the performance of MODIS LST. Strong negative deviation of MODIS LST values (5 – 15 K) compared to thermal camera images indicates cloud top temperatures

were contaminating some MODIS LST values.

Here we show that sampled air temperature, used in conjunction with collection 5 MODIS tile LST, can reproduce daytime clear-sky land surface temperatures with sufficiently high accuracy to identify cloud contaminated grid cells missed by the standard MODIS cloud-masking algorithms. We first define the relationship between MODIS LST and air temperature (T_{air}) recorded at four Environment Canada weather stations located between 542-807 m.a.s.l. in the southwest Yukon (Figure 2-1). T_{air} is recorded on the hour between 2000 and 2008. These measurements were matched to daytime MODIS Terra LST values that were recorded within 12 minutes of the hour. We subsequently used ground-based sky cloud content information recorded on the hour at two of the four stations to determine how sky cloud content affects the LST to T_{air} relationship. The sky cloud content gathered at weather stations provides a means to examine how increased cloud content correlates with increased cloud contamination in MODIS LST. We refine the LST to T_{air} relationships for each of the sky cloud coverage using the MOD11A1 quality flag. Lastly, we compare “good” quality confirmed “clear” sky relationships to “good” quality “mainly clear” and “mostly cloudy” sky relationships to identify cloud contamination missed by the MODIS quality flag in the latter two data sets.

Study Area

The southwest Yukon study area is bounded by the Yukon – Alaska border (141°W) on the west and southwest, the Yukon – British Columbia border on the south

(60°N), 134°W on the east, and 62.5°N on the north. This section of the Yukon contains four Environment Canada meteorology monitoring stations (Figure 2-1), all of which are situated near airfields at low elevation. This region is affected by the St. Elias Mountains rain shadow, and annual precipitation is 30-80 cm. Although not typically considered to be a semi-arid or arid landscape (a type known to impede the function of the MODIS LST algorithm (Wan, 2002)), the effect that relatively dry portions of this landscape might have on emissivity determination has not been quantified. The Environment Canada weather station sites at Burwash Landing, Haines Junction, and Carmacks are largely covered by homogeneous boreal forest (beyond the confines of the airports where the stations are situated), with a small area of open water from the Yukon River contained in the Carmacks MODIS LST grid cell. The Whitehorse MODIS grid cell contains several land cover classes, including urban, roads and forest. Cloud cover is frequent throughout the year in this part of the Yukon.

Data

The daily MODIS Land Surface Temperature (MOD11_L2) product is dependent on several parameters related to the satellite platform and sensor, and is generated using the Product Generation Executive (PGE16) code. The MOD11_L2 is in swath format and collected sequentially on a single overpass. The swath is composed of several products, including geolocation, sensor radiance, atmospheric temperature and water profiles, cloud mask, quarterly land cover, and snow cover. Several MODIS land surface temperature products are produced at daily, eight day or monthly intervals at a

gridded resolution of 1 km and 6 km and on a 0.05° grid. The MOD11A1 product used here is produced by mapping daily single clear-sky observation MOD11_L2 swath data onto 1 km tiled grids in sinusoidal projection. MODIS Terra satellite and its sister satellite Aqua, are in sun-synchronous near-polar orbits, with Aqua in an ascending orbit and Terra in a descending orbit. The orbital structures dictate equatorial crossings at 10:30 AM for Terra and 1:30 PM for Aqua (local solar time). Because of the near-polar orbit, there is progressively more swath overlap at locations greater than 30° latitude, thus producing multiple daily observations in these regions.

MODIS (MOD11A1) Terra Collection 5 clear-sky daytime Land Surface Temperatures (LST)

The MODIS LST data used in this study are the MOD11A1 h11 tile data acquired daily under daytime clear-sky conditions, using reprocessing Collection 5 (henceforth “LST”) and refer to the MOD11A1 Collection 5 clear-sky daytime data set. The MOD11A1 tile data are generated from the MOD11_L2 swath data. The MOD11A1 data contain single observations in each grid cell rather than averaged observations. MODIS data were downloaded from the Land Processes Distributed Active Archive Center – LPDAAC (<https://lpdaac.usgs.gov/>). The basic 1 km gridded MODIS land surface temperature is produced with a split window technique that uses MODIS bands 31 and 32 (10.78 – 11.28 μm and 11.77 – 12.27 μm , respectively) and is detailed by Wan and others (2002). This technique uses a global land surface classification-based emissivity look-up table (Snyder et al., 1998) to estimate emissivity

values in these two bands. A split window technique is used to produce the 1km LST product whereas the 5km LST product uses the day/night algorithm. The split window class of techniques uses the difference in water-vapor absorption that exists between band 31 and band 32 to determine surface temperature. Cloud contamination is known to cause LST error in the split window temperature extraction method (Jin and Dickinson, 2000).

Nishida et al. (2003) employed the MOD11A1 quality control flag for cloud screening, an approach we also employ here. The quality flag information relating to Collection 5 of the MODIS land Surface Temperature products is found in the product Users' guide found at http://www.ices.ucsb.edu/modis/LstUsrGuide/MODIS_LST_products_Users_guide_C5.pdf. The MODIS quality flag used in this study is the Daytime LSTE quality control layer. The first bit indicates whether the produced LST is of good quality and does not require further inspection of the quality flags; or if the LST was produced but that the quality is unreliable or unquantifiable and further quality flag inspection is required. Inspection of the all MODIS quality flags produced for the unreliable or unquantifiable quality first bit provides differentiation of the average temperature quality flags as ≤ 3 K, ≤ 2 K and ≤ 1 K which is the nominal (or minimum) level; the > 3 K average temperature quality flag wasn't assigned to any of the data considered in this study. Grid cells with the MODIS quality flags raised related to emissivity and sub-pixel cirrus cloud presence were eliminated from this study; these affected less than 5 % of the total data set.

MODIS data pre-processing

The MOD11A1 tile data were subset to the study area, as defined above. MOD11A1 LST and the coincident local solar View Time (VT) from 2000 through 2008 were reprojected from sinusoidal projection to 1 km gridded geotiff Albers Equal Area Projection, North American Datum 83 (NAD83) using nearest neighbour resampling. This processing step was batch run using the MODIS Reproject Tool (MRT) (Dwyer and Schmidt, 2006) available from the LPDAAC. These LST product layers were converted to local solar time and temperature using the conversions factors provided at <http://lpdaac.usgs.gov/modis>. The view times in the MOD11A1 product are in local solar time, which are defined as the MODIS observation time in UTC + longitude in degrees at the 1km grid cell divided by 15. MODIS view times are converted from local solar time to local time to enable comparison to meteorological station data.

Meteorology station air temperature and weather observations

Air temperature data used in this study were collected on the hour at four long-term Environment Canada meteorology monitoring stations. Hourly air temperature data and weather observations were downloaded from Environment Canada's National Climate Archive (http://www.climate.weatheroffice.gc.ca/Welcome_e.html). Ground based cloud observations are only available from non-automated observation weather stations, which include two of the four stations in the study region (Burwash and Whitehorse stations). The sky observation total cloud amount is recorded in tenths

when no visibility obstruction (e.g. smoke) occurs. Cloud observations are grouped into four categories: “Clear” (0 tenths obstructed); “Mainly clear” (1 to 4 tenths); “Mostly cloudy” (5 to 9 tenths); “Cloudy” (10 tenths). Table 2-1 provides information regarding the location, elevation and other characteristics of the four meteorology stations.

MODIS and Meteorology data intersection

Daily MODIS layers containing LST values and each grid cells’ associated view time (time of LST capture) were matched with the four Environment Canada meteorology station locations (Whitehorse, Carmacks, Haines Junction, Burwash Landing) using nearest neighbour sampling. The MODIS data used extend from March 2000 to the end of 2008. Only MODIS LST values that were recorded within 12 minutes of the hour (air temperature is recorded on the hour) were retained for analysis. The positions of each meteorology station within the 1 km by 1 km grid cell are different for each location.

Statistical Analysis

At warmer temperatures ($> 0\text{ }^{\circ}\text{C}$) the MODIS LST and air temperatures reported here displayed a slight departure from a linear relationship. We fitted the MODIS LST - air temperature relationship for all sites with a linear model and again with a quadratic model. We compared the values of the residuals generated from both statistical fits at each sampling period with a matched pair t-test to determine whether the two models

were significantly different from each other (Zar, 2009).

We compared the departure from the predicted linear fit for the MODIS LST – air temperature relationship at all sites for three levels of average temperature quality flag (≤ 1 K, ≤ 2 K, ≤ 3 K). The data were $\log(x+1)$ transformed to a normal distribution thus compensating for a positive skew. Preliminary analyses indicated that the within-group variances of the three quality groups were not equal, so we proceeded to analyse the data with Welch’s ANOVA (Zar, 2009). The quality flags we used are associated with temperature uncertainty; all other quality flags, such as errors associated with cirrus clouds, occurred infrequently and were removed from analysis throughout.

We compared the mean temperature associated with each average temperature quality flag. If assignment of the quality flags occurred randomly throughout the year and are based on MODIS spectral thresholds, the mean temperature associated with each error code should not be significantly different between groups. Data were square root transformed and then reflected to correct a negative skew in distribution (Zar, 2009). Preliminary analyses indicated that the within-group variances of the three groups were not equal so we proceeded to analyse the data with Welch’s ANOVA.

Results

The four sites studied here produce similar curves of LST versus T_{air} and display a slight positive curvature. Strong quadratic correlations between MODIS LST and instrumental air temperatures (R^2 of 0.95 - 0.96) are observed at the four Environment Canada meteorology stations (Figure 2-2). The Whitehorse, Carmacks, Burwash

Landing and Haines Junction monitoring station locations are found at different elevations and are located at different positions within the LST grid cell. The results are similar to those of Comiso (2003) for matching air temperature to AVHRR LST data for air temperatures below 0 °C. Furthermore, the relationships are consistent with findings by Karlsen & Elvebakk (2003) where the differences between subsurface temperature and air temperature start to appear above 0 °C and are greatest for the warmest temperatures. When the pooled MODIS LST – T_{air} relationship was fitted with a quadratic equation (to compensate for the departure from linearity), the increase in fit from $R^2 = 0.942$ (ANOVA, $F_{1,1023} = 1666$, $p = 0.00001$) for the linear fit to $R^2 = 0.954$ (ANOVA, $F_{2,1022} = 10652$, $p = 0.00001$) for the quadratic fit was strongly insignificant (matched pairs $t_{2291} = 0.021$, $p = 0.9826$). View angle, relative humidity (Carmacks' relative humidity data was unavailable), amount of time between recording of air temperature and LST (to a maximum of 12 minutes) and wind speed did not produce statistically significant results for the variation between LST and T_{air} for the polynomial fits. The magnitude in the difference from the predicted quadratic fit for MODIS LST – T_{air} was significantly different among the three groups of average temperature quality flags (Welch's ANOVA ($F_{2,137.56} = 7.7111$, $p = 0.0007$)). The mean departure (untransformed data) in Kelvin from the predicted fit was lowest for average temperature quality flag ≤ 3 K ($n = 49$, mean \pm standard error = $1.75 \text{ K} \pm 0.36 \text{ K}$) compared to quality flag ≤ 1 K ($n = 771$, mean \pm S.E. = $2.75 \text{ K} \pm 0.087 \text{ K}$) and quality flag ≤ 2 K ($n = 933$, mean \pm S.E. = $2.87 \text{ K} \pm 0.079 \text{ K}$).

Langer et al. (2010) found that the largest differences in LST for tundra land cover classes, including water, were found for the highest values of net radiation. The

MODIS LST values used here were collected under conditions of daytime ‘clear-sky’ when the land surface is experiencing the higher end of the daily range of net radiation. Thus large water bodies found within the MODIS LST grid cell will be moderated by the relatively high heat capacity of water. The slightly greater linearity and higher R^2 value found at Carmacks (Figure 2-2) is likely related to the moderating effect of water from the Yukon River, which is contained within the southwest 10% - 15% of the LST grid cell. The 5% uncertainty in the previously stated range of areal water coverage is estimated using the 50 m at nadir MODIS geolocation accuracy (Wolfe et al., 2002). None of the other three MODIS LST grid cells contains large water bodies; the Whitehorse grid cell containing the Environment Canada meteorology station did not cover the Yukon River.

The mean LST grouped by three temperature error codes differed significantly (Welch’s ANOVA ($F_{2,285.16} = 1403.4077$, $p = 0.001$)). The mean temperature for quality flag ≤ 3 K was significantly lower ($X = \text{mean} \pm \text{S.E.} = 242.89 \text{ K} \pm 0.67 \text{ K}$) compared to both Error Code ≤ 1 K ($X = \text{mean} \pm \text{S.E.} = 281.59 \text{ K} \pm 0.56 \text{ K}$) and Error Code ≤ 2 K ($X = \text{mean} \pm \text{S.E.} = 276.53 \text{ K} \pm 0.45 \text{ K}$). This indicates the LST associated with the ≤ 3 K quality flag originated from the colder portion of the data set ($< 0^\circ \text{C}$).

Constraining the LST to T_{air} relationship at Whitehorse and Burwash with ground-based sky observations of “clear” sky (zero cloud cover), “mainly clear” and “mostly cloudy” sky conditions decreases the correlation coefficient for a quadratic model and causes a progressively more negative y-intercept (Figure 2-3). The use of the quadratic model for this section of analysis shows that some of the curvature in the LST to T_{air} relationships reported here is related to cloud cover. Figure 4 shows quadratic

relationships displayed in Figure 2-3 for the Whitehorse meteorological station, but separated by the MODIS quality flag of “good” quality (left column) and “unreliable or unquantifiable” quantity. Figure 2-5 shows quadratic relationships displayed in Figure 2-3 for the Burwash meteorological station, but separated by the MODIS quality flag of “good” quality (left column) and “unreliable or unquantifiable” quantity. The quadratic equations of fit for Figures 2-4 and 2-5 shows the y-intercept decreases as sky cloud content increases (from top to bottom panels). Plotting the “good” quality confirmed “clear” sky trend on ensemble good quality “mainly clear” and “mostly cloudy” for each location shows that 13 % (Whitehorse) and 17 % (Burwash) LST values appear below the lower bound of the trend lines as defined by the root mean square (RMS) value for the confirmed uncontaminated trend (Figure 2-6). These values are consistent with the estimates for unidentified cloud contamination of MODIS data (Ackerman et al., 2008; Shi et al., 2007). Four data points in the Burwash ensemble good quality “mainly clear” and “mostly cloudy” were removed from this analysis because they were colder than any data point in the “good” quality confirmed “clear” sky data.

Discussion

Approximately 15 % of cloud-contaminated grid cells are not being detected by the MODIS cloud mask (Ackerman et al, 2008). For the AVHRR sensor, an increase in cloud coverage as viewed from the ground correlates with a diminished confidence that the sensor is viewing clear sky (Ackerman et al., 1998). Here we extend this principle to include surface air temperature as a way to identify undetected cloud contamination

in MODIS LST data. Thus an increasing amount of sky cloud content observed from the ground (a portion of which contains a MODIS grid cell that encompasses an air temperature monitoring stations) correlates with colder LST values when compared to temporally matched air temperature recordings. The confirmed “clear” sky, “good” quality relationships (upper left panels in Figures 2-4 and 2-5) displayed the highest correlation coefficients using a quadratic fit. If “good” quality flagged MODIS grid cells were truly free of contamination, we would expect that the relationships found for “clear”, “mainly clear” and “mostly cloudy” would be similar. The consistent reduction of y-intercept from the LST to T_{air} relationships, progressively constrained by ground based sky observations of “clear” to “mostly cloudy” indicates the relationship in the “good” quality flagged MODIS grid cells are increasingly contaminated with cloud (left panels in Figures 2-4 and 2-5). Indeed if the right panels in Figures 2-4 and 2-5 (unreliable or unquantifiable quality) are considered, a clear trend to more cloud contamination from “clear” to “mostly cloudy” is observed as expected. We conclude that this technique provides a semi-quantitative method to determine daytime MODIS LST cloud contamination by plotting any daytime LST to T_{air} intersection against the quadratic fit for confirmed clear sky, good quality data. LST values found below the RMS error of the trend line are considered contaminated.

Some variation in the LST to T_{air} relationship trends might be related to the ≤ 12 minute discrepancy between air temperature recording and LST capture. However, we showed this variation was statistically non-significant, likely because air temperature reacts slowly compared to LST following short-lived perturbations (i.e., cloud shadow) over a 1 km grid cell, especially in comparison to cloud contamination in the LST grid

cell. Findings by Wang and others (2008) indicated no seasonal bias in nighttime field LST measurements and MODIS LST. Furthermore Bartlett and others (2006) found that snow cover exerts only a minor influence on the annual tracking of subsurface and air temperature. We found that the ≤ 3 K quality flag originated from the below 0°C portion of the LST data set exclusively, suggesting that the assignment of this quality flag is sensitive to a specific set of atmospheric and land cover conditions.

The LST versus T_{air} equations of fit for Whitehorse are bounded by the equations of fit for Burwash Landing and Haines Junction which have simpler and more homogeneous forested land cover class compared to multiple land cover classes found at the Whitehorse airport where air temperature is recorded (Figure 2-2). This suggests that the MODIS LST at 1 km adequately integrates landscape variability (and thus emissivity variation) within the grid cell, regardless of the placement of the monitoring station, well enough to identify the influence of cloud contamination missed by the MODIS cloud mask. Furthermore, there is likely an influence on the relationships found here from cloud shadow, but this was assumed to be small compared to that from cloud contamination, because view angle didn't show a statistically significant influence on the LST to T_{air} relationship. The view capture angles of MODIS LST ($<55^{\circ}$) likely make the cloud shadow effect small compared to the effect of cloud contamination, especially in relation to air temperature.

The degree of cloud contamination in the MODIS grid cells appears to be responsible for the major part of observed variation in LST, manifested as the systematic bias towards a colder-than-true values. This phenomenon will likely have a moderating effect on apparent LST trends, if contamination is not identified or cloud content is not

fully considered (e.g. Liu et al., 2008). In the larger context of infrared derived LST, the findings of this study indicate that more accurate trends will be produced if cloud contamination is further reduced. Therefore we argue that all available means for the identification of cloud contamination, including using meteorological stations in a coordinated approach to produce validated satellite data, should be employed.

Further work is required to identify the type and degree of cloud contamination in MODIS land surface temperature. A re-evaluation of the MODIS cloud mask could be completed using the technique outlined in this paper in conjunction with more precise observations, such as LiDAR, to further refine spectral thresholds for cloud contamination detection.

Conclusions

In this study we compared MODIS (MOD11A1 – Collection 5) Terra clear-sky daytime Land Surface Temperatures (LST) to temporally matched Environment Canada meteorological station air temperatures in the southwest Yukon to identify cloud contamination missed by the MODIS cloud mask. Using qualitative ground based sky condition observations and coincident MODIS quality flag information available at two stations we further refined the MODIS LST to air temperature relationships. The relationships constrained by ground observations of “clear” sky conditions showed less variability than those found under “mainly clear” and “mostly cloudy” sky conditions. Furthermore there was a systematic decrease in the y-intercept of the quadratic equations indicating a systematic bias of unidentified cloud contamination (not detected

by the MODIS cloud-screening methods) on the MODIS “good” quality LST product. The trend of an increasing cloudy sky decreasing the LST to air temperature y-intercept is largely consistent with the MODIS LST quality flag information. However, the assignment of the ≤ 3 K quality flag was biased to temperatures below 0 °C suggesting the degree of temperature contrast between cloud and target needed for discrimination of cloud contamination is greater than 2 K. The amount of unidentified cloud was determined to be 13 % at Whitehorse and 17 % at Burwash, values that are consistent with other published studies on unidentified cloud contamination in MODIS data. The clear sky “good” quality LST to air temperature relationship provided here could be used to provide further cloud discrimination of MODIS data especially if used in concert with other cloud detection methods.

Table 2-1: Station information for the four Environment Canada locations in the southwest Yukon.

Station	Latitude; Longitude	Elevation (m.a.s.l.)	Description
Whitehorse (A)	60.71°N; 135.07°W	706	Environment Canada Monitoring and Observation Station
Haines Junction	60.77°N; 137.58°W	599	Environment Canada Monitoring Station
Carmacks	62.12°N; 136.19°W	542	Environment Canada Monitoring Station
Burwash (A)	61.37°N; 139.05°W	807	Environment Canada Monitoring and Observation Station

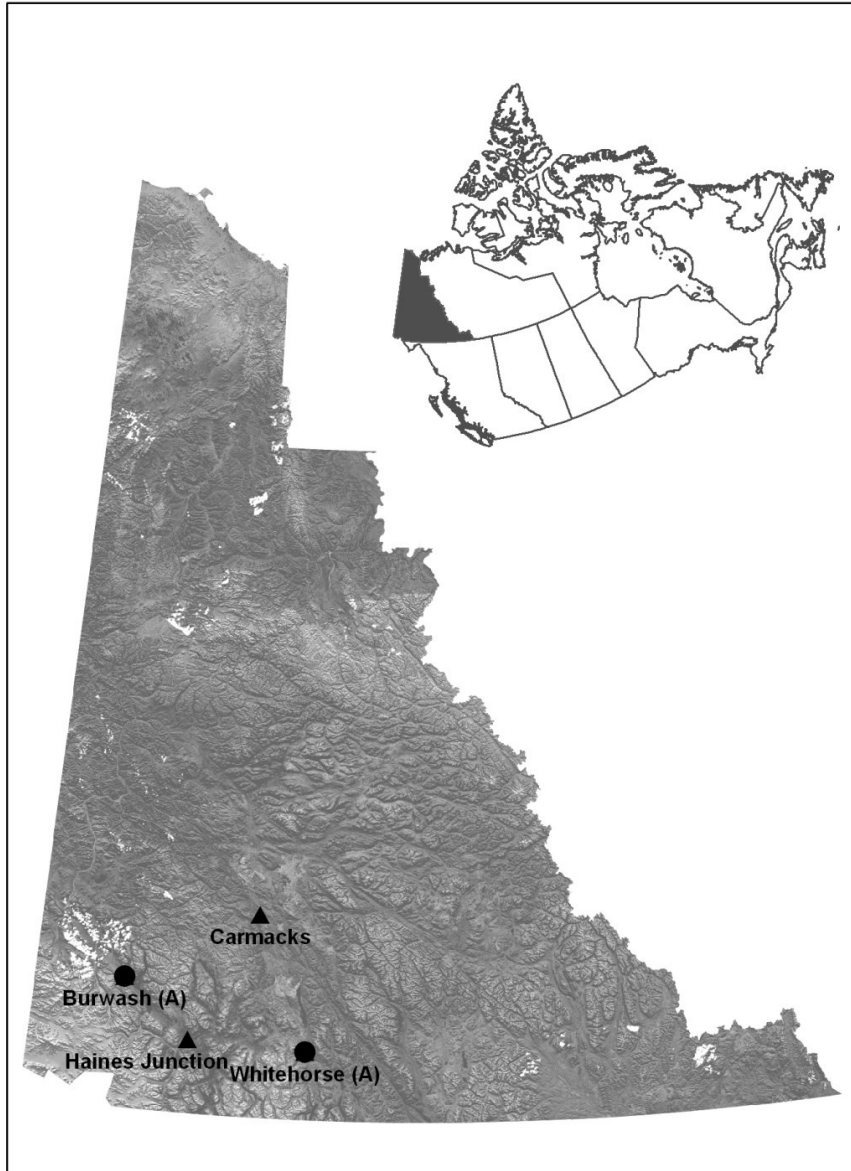


Figure 2-1: Southwest Yukon study area showing the location of Environment Canada meteorology air temperature recording stations (black triangles) and air temperature and sky observation recording stations (black circles). Base Landsat mosaic of the Yukon was obtained from the Yukon Government, Department of Geomatics.

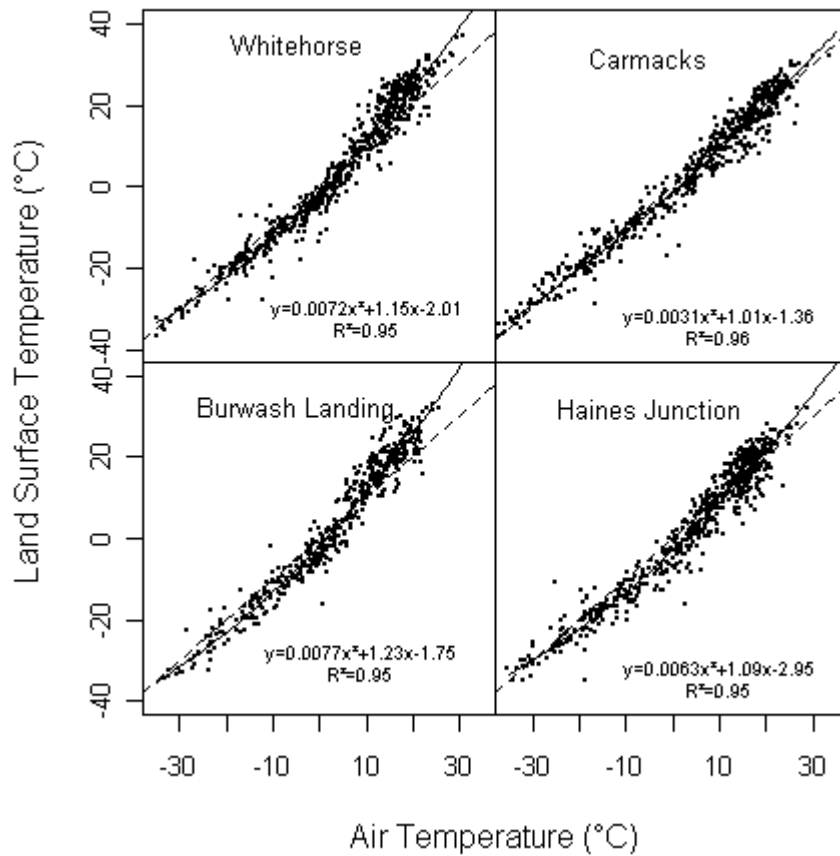


Figure 2-2: 2000 – 2008 temporally matched MODIS LST versus Environment Canada air temperature at Carmacks, Haines Junction, Whitehorse, and Burwash Landing stations. The solid line indicates the quadratic fit and the dashed line indicates the 1:1 line.

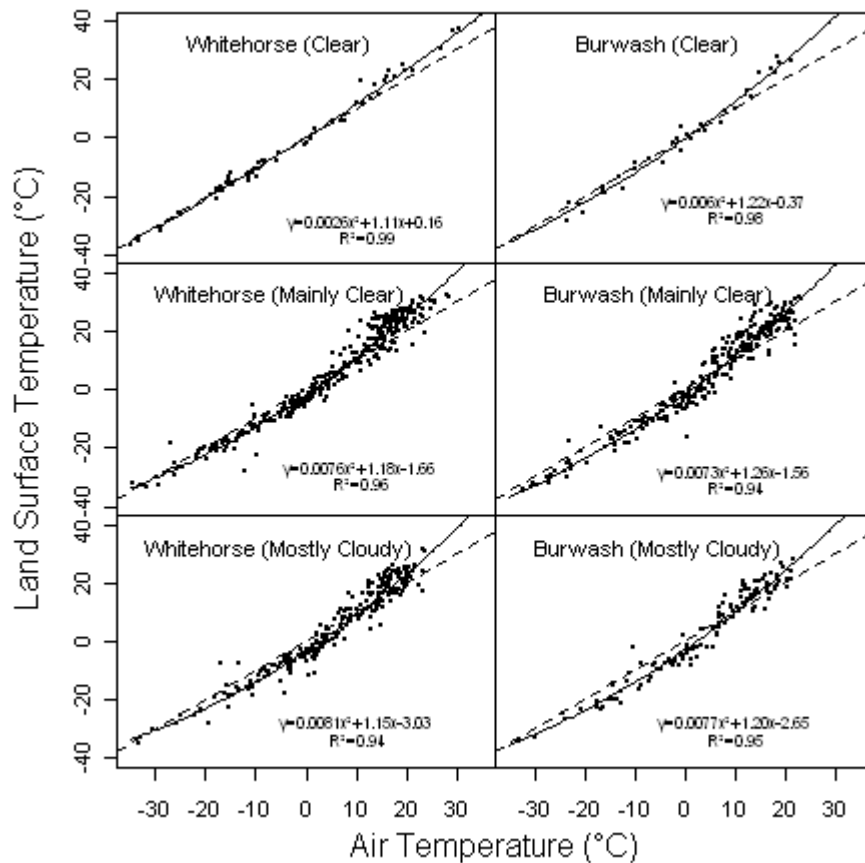


Figure 2-3: 2000 – 2008 temporally matched MODIS clear-sky LST versus Environment Canada air temperature at Whitehorse, and Burwash for ground based assessment of cloud content, but including all MODIS temperature quality flag information. “Clear” sky (top), “mainly clear” sky conditions (middle), and “mostly cloudy” sky conditions (bottom). The solid line indicates a quadratic fit; the dashed line indicates a 1:1 line.

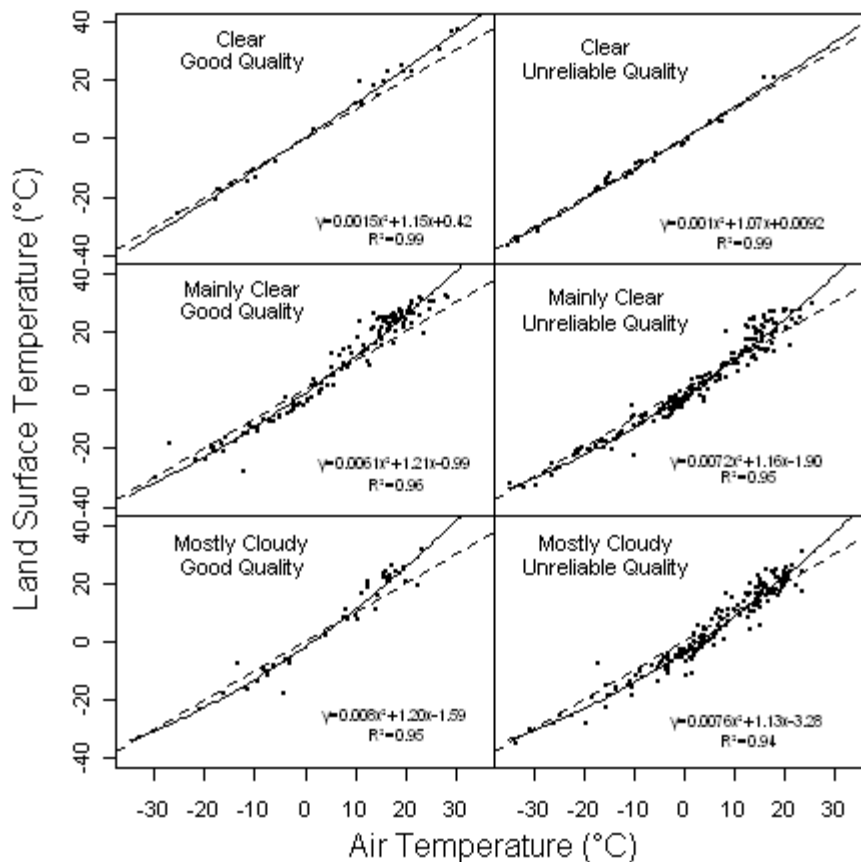


Figure 2-4: 2000 – 2008 temporally matched MODIS clear-sky LST versus Environment Canada air temperature at Whitehorse for ground based cloud content assessment. “Clear” sky (top), “mainly clear” sky conditions (middle), and “mostly cloudy” sky conditions (bottom). The left column is MODIS LST with “good” quality flag values and the right column contains LST values of “unreliable or unquantifiable” quality. The solid line indicates a quadratic fit; the dashed line indicates a 1:1 line.

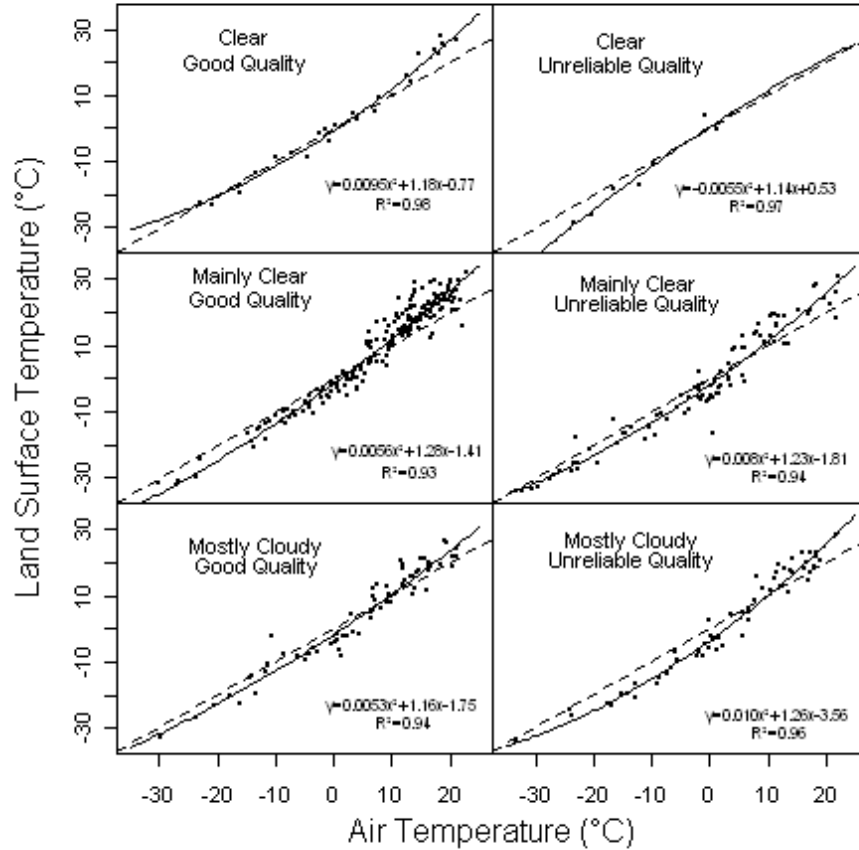


Figure 2-5: 2000 – 2008 temporally matched MODIS clear-sky LST versus Environment Canada air temperature at Burwash for ground based cloud content assessment. “Clear” sky (top), “mainly clear” sky conditions (middle), and “mostly cloudy” sky conditions (bottom). The left column is MODIS LST with “good” quality flag values and the right column contains LST values of “unreliable or unquantifiable” quality. The solid line indicates a quadratic fit; the dashed line indicates a 1:1 line.

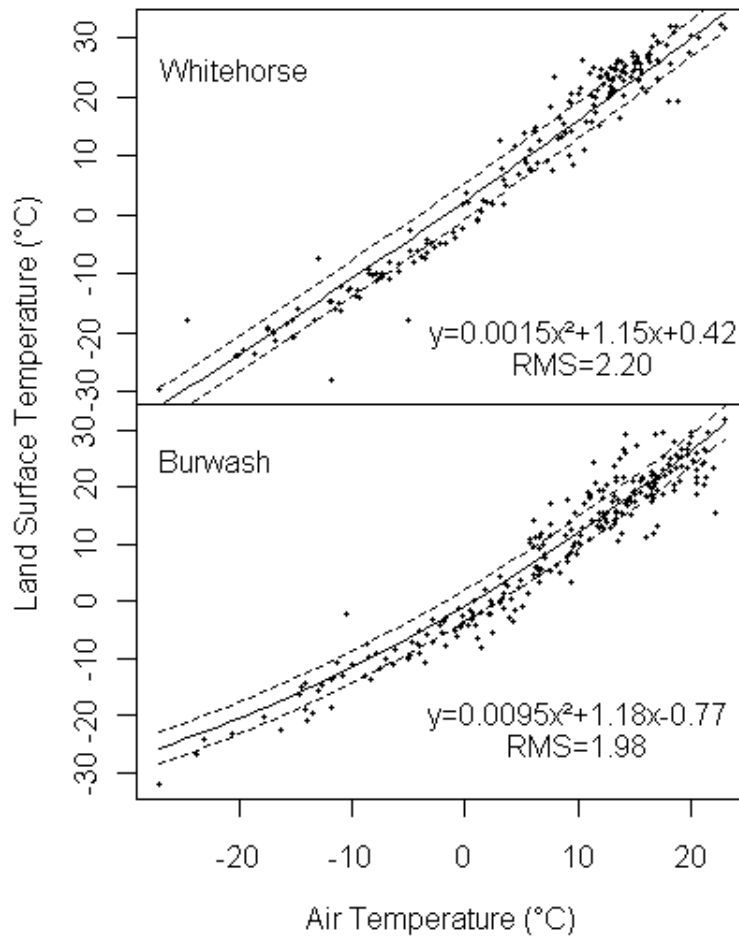


Figure 2-6: 2000 – 2008 temporally matched MODIS clear-sky LST versus Environment Canada air temperature at Whitehorse and Burwash for “good” quality “mainly clear” and “mostly cloudy” data from Figures 4 and 5. On these are the plotted quadratic fits found for “clear” sky and “good” quality data for each site (solid line). The dashed line is the RMS generated from the “clear” sky “good” quality data specific to each site. Any points falling below the bottom dashed line are likely cloud contaminated.

References

- Ackerman, S. A., Strabala, K. I., Menzel, W. P., Frey, R. A., Moeller, C. C., & Gumley, L. E. (1998). Discriminating clear sky from clouds with MODIS. *Journal of Geophysical Research*, **103**, 32141-32157.
- Ackerman, S. A., Holz, R. E., Frey, R., Eloranta, E. W., Maddux, B. C., & McGill, M. (2008). Cloud detection with MODIS. Part II: Validation. *Journal of Atmosphere and Oceanic Technology*, **25**, 1073-1086.
- Bartlett, M. G., Chapman, D. S., & Harris, R. N. (2006). A decade of ground-air temperature tracking at Emigrant Pass observatory, Utah. *Journal of Climate*, **19**, 3722-3731.
- Comiso, J. C. (2003). Warming trends in the Arctic from clear sky satellite observations. *Journal of Climate*, **16**, 3498-3510.
- Dwyer, J., & Schmidt, G. (2006). The MODIS reprojection tool. In J. J. Qu, W. Gao, M. Kaftos, R. E. Murphy, & V. V. Salmonson, Eds., *Earth science satellite remote sensing*, Berlin Heidelberg: Springer Berlin Heidelberg, 162-177.
- Jin, M., & Dickinson, R. E. (2000). A generalized algorithm for retrieving cloudy sky skin temperature from satellite thermal infrared radiances. *Journal of Geophysical Research - Atmosphere*, **105**, 27037-27047.
- Karlsen, S. R., & Elvebakk, A. (2003). A method using indicator plants to map local climactic variation in the Kagerlussuaq/Scoresby Sund area, East Greenland. *Journal of Biogeography*, **30**, 1469-1491.

- Langer, M., Westermann, S., & Boike, J. (2010). Spatial and temporal variations of summer surface temperatures of wet polygonal tundra in Siberia – implications for MODIS LST base permafrost monitoring. *Remote Sensing of Environment*, **114**, 2059-2069.
- Liu, Y., Key, J. R., & Wang, X. (2008). The influence of changes in cloud cover on recent surface temperature trends in the Arctic. *Journal of Climate*, **21**, 705-715.
- Nishida, K., Nemani, R. R., Glassy, J. M., & Running, S. W. (2003). Development of an Evapotranspiration Index From Aqua/MODIS for Monitoring Surface Moisture Status. *IEEE Transactions Geoscience and Remote Sensing*, **41**, 493-501.
- Platnick, S., King, M. D., Ackerman, S. A., Menzel, W. P., Baum, B. A., Riedi, J. C., & Frey, R. A. (2003). The MODIS Cloud Products: Algorithms and Examples From Terra. *IEEE Transactions Geoscience and Remote Sensing*, **41**, 459-473.
- Shi, T., Clothiaux, E. E., Yu, B., Braverman, A. J., & Groff, D. N. (2007). Detection of daytime Arctic clouds using MISR and MODIS data. *Remote Sensing of Environment*, **107**, 172-184.
- Snyder, W.C., Wan, Z., Zhang, Y., & Feng, Y. Z. (1998). Classification-based emissivity for land surface temperature measurement from space. *International Journal of Remote Sensing*, **19**, 2753-2774.
- Wan, Z., Zhang, Y., Zhang, Q., Li, Z. (2002). Validation of the land-surface temperature product retrieved from Terra Moderate Resolution Imaging Spectroradiometer data. *Remote Sensing of Environment*, **83**, 163-180.

- Wan, Z. (2008). New refinements and validation of MODIS land-surface temperature/emissivity products. *Remote Sensing of Environment*, **112**, 59-74.
- Wang, W., Liang, S., & Meyers, T. (2008). Validating MODIS land surface temperature products using long-term nighttime ground measurements. *Remote Sensing of Environment*, **112**, 623-635.
- Wolfe, R. E., Nishihama, M., Fleig, A. J., Kuyper, J. A., Roy, D. P., Storey, J. C., & Patt, F. S. (2002). Achieving sub-pixel geolocation accuracy in support of MODIS land science. *Remote Sensing of Environment*, **83**, 31-49.
- Zar, J. H. (2009). *Biostatistical Analysis*, 5th Edition. Prentice Hall, Upper Saddle River, New Jersey, 944pp.

CHAPTER THREE

Estimating Temperature Fields from MODIS Land Surface Temperature and Air Temperature Observations in a Sub-Arctic Alpine Environment²

Introduction

High latitudes in the Northern Hemisphere have experienced significant recent warming, with Yukon and parts of Alaska experiencing the greatest warming of sub-Arctic environments over the last 50 years (SWIPA, 2011; ACIA, 2004). This warming trend is expected to continue throughout the Arctic (IPCC, 2007). Temperature changes will affect many aspects of northern alpine ecosystems and the associated cryosphere, including snow extent, tundra land cover composition and distribution, permafrost, net ecosystem productivity, and population dynamics of animals and plants (Post et al., 2009).

Mean surface temperature provides a fundamental measure for understanding change occurring in Arctic, sub-Arctic and alpine land surface processes. However, the absence of fine scale, continuous temperature monitoring over large geographical areas makes identifying climate induced changes difficult. Air temperature is commonly measured hourly at ground-based monitoring stations which are usually sparsely located in valley bottoms, and thus the lower end of the elevation gradient in alpine regions. For example, in Yukon, Canada, which has an area of 483,450 km², there are only eleven

² A version of this chapter was published in Remote Sensing as: Williamson, S. N., Hik, D. S., Gamon, J. A., Kavanaugh, J. L., & Flowers, G. E. (2014). Estimating temperature fields from MODIS land surface temperature and air temperature observations in a sub-Arctic Alpine environment. *Remote Sensing*, 6(2), 946-963.

meteorological stations maintained by Environment Canada

(<http://www.climate.weatheroffice.gc.ca>). Furthermore, in the mountainous southwest Yukon the highest elevation station is 807 m above sea level. Spatial interpolation of air temperature data can lead to considerable uncertainties in the resulting temperature fields (Vincent & Mekis, 2006), especially at higher elevation.

An increasingly common method for tracking surface temperature trends in the Arctic involves the use of infrared satellite measurements of surface temperature (Comiso, 2003). Polar and near polar orbiting satellites exhibit progressively overlapping swaths, thus at high latitudes many ground surface observations are available each day. However, the swath overlap of near polar orbiting satellites over sub-polar regions is often insufficient to construct diurnal temperature curves because of cloud cover, thus necessitating a robust gap filling method to convert single daily observations to daily averages.

Land surface temperature (or skin temperature) is likely a better descriptor than air temperature for processes that are strongly linked to the ground surface such as low stature Arctic vegetation growth, permafrost dynamics, and gas fluxes. Terrestrial ecosystems are often described in terms of their characteristic annual and seasonal temperature and precipitation patterns (Holdridge, 1967; Lugo et al., 1999). The distribution and abundance of Arctic vegetation is dictated to a large extent by summer temperature, which can be characterised by satellite derived land surface temperature metrics (Raynolds et al., 2008; Bhatt et al., 2013).

MODIS Terra and Aqua satellites are in sun-synchronous near polar orbits, with Aqua in an ascending orbit and Terra in a descending orbit with equatorial crossings at

10:30 AM for Terra and 1:30 PM for Aqua (local solar time). Both satellites require approximately 90 min to complete an Earth orbit. MODIS Terra data became available in February 2000 and Aqua data became available in July 2002. At the latitude of our study site (60°N), Aqua coverage coincided with dawn and predawn. MODIS is in a low altitude orbit (705 km), and has 36 spectral bands thus improving the cloud detection ability of MODIS over previous satellites.

The daily record of LST observations is limited to those from the MODIS Terra platform between 2000 and 2002, which halves the amount of daily observations provided by the Terra and Aqua ensemble. Validation of MODIS land surface temperature products has emphasised the nighttime product (Wang et al., 2008; Wan, 2008), which is easier to validate. The effects of relative humidity, wind speed, soil moisture, air temperature and sensor view zenith angle on night time land surface temperatures have been investigated, of which only sensor view zenith angle showed a weak influence on LST error propagation (Wang et al, 2008).

Analysis of thermal images and up to 18–20 daily MODIS LST returns collected over wet polygonal tundra in Siberia (Langer et al., 2010) and high Arctic tundra in Svalbard (Westermann et al., 2011) indicated that several improvements regarding the performance of MODIS LST over tundra should be considered: (i) improved cloud cover masking and gap filling techniques; (ii) accounting for water bodies; (iii) accounting for snow cover and soil properties. The acquisition of daily satellite observations is complicated by extensive cloud cover commonly experienced in the Arctic, and summer cloud cover has been shown to be increasing in the circumpolar Arctic (Wang & Key, 2003). Cloud contamination, due to a failure of the cloud

detection algorithm, is a known cause of LST error in the split window temperature extraction method (Jin & Dickinson, 2000). However, cloud contamination continues to be an issue with MODIS LST data where approximately 15% of data contain unidentified cloud contamination (Ackerman et al., 2008; Williamson et al., 2013).

Due to the spatial and temporal autocorrelation of thermal infrared satellite temperatures, spatial distances of 100–300 km and temporal intervals of up to two days were sufficient to represent missing data (Jin, 2000). Furthermore, the diurnal cycle of LST could be modeled with solar geometry and two daily LST data points (Jin & Treadon, 2003). Maximum air temperature can be modelled with the diurnal cycle, cloud fraction and minimum air temperature derived from night-time LST (Vancutsem et al., 2010). The use of a generic modelled diurnal cycle in the interpolation of surface temperature to a diurnal cycle has also been proposed (Jin & Dickinson, 1999), where maximum daily LST, under clear sky conditions will correspond to peak solar insolation, with a small adjustment for phase lag (Jin & Dickinson, 1999) related to the period of time required for net radiation to reach zero. Minimum LST will correspond to around the time of sunrise (Sellers, 1965). It is important when aggregating LST observations in high latitudes to pay close attention to daytime length, satellite tile area and over pass time. These factors will contribute to the magnitude of within scene and between scene measurements, especially for observations on the continental scale.

A strong linear correlation between AVHRR LST and air temperature has been reported for temperatures $< 0^{\circ}\text{C}$ (Comiso, 2003). Many recent studies have found strong linear correlations between MODIS LST (maximum, minimum and average) and air temperatures for many land cover types in Africa (Vancutsem et al., 2010), in

Portugal (Benali et al., 2012), on the Tibetan Plateau (Zhu et al., 2013) and over the conterminous United States (Crosson et al., 2012). Steps have been taken to compare MODIS LST with much coarser spatial resolution passive microwave surface temperatures (Sun et al., 2012) and climate reanalysis products (Soliman et al., 2012). The typical range of errors when correlating LST to air temperature is approximately 2–3 °C (Zaksek & Schroedter-Homscheidt, 2009) irrespective of the methodology, spatial or temporal resolutions.

This study was conducted to assess the viability of using an interpolated air temperature curve and a single day time LST value for the purpose of extending the daily average LST in a mountainous sub-Arctic region when (1) persistent cloud cover often reduces LST acquisition to a single daily value and (2) for early years of Terra data acquisition, when MODIS Aqua was not operational. We produced a Interpolated Curve Mean Daily Surface Temperature (ICM) product by combining single daily tiled day-time MODIS LST observations (regardless of acquisition time during the day) with the daily average air temperature and daily air temperature curve, using data from 2008. We then compared daily average temperatures from seven independent meteorology stations to daily average LST created from minimum and maximum LST values (MMM) produced from both MODIS Aqua and Terra swath data. We compared both models to daily average air temperature from the seven independent meteorology stations located on glacier, barren and tundra land covers. Lastly, we aggregated the MMM model to 8-days and compared the result to similarly aggregated air temperature to assess the consequences of aggregating LST data. The methods outline above identify limitations in previous approaches by (i) incorporating air temperature observations with

LST, to bolster limited LST observations, instead of trying to convert LST to air temperature; and (ii) requiring the use of information about the diurnal curve and data availability for improving LST aggregation.

Study Area

The southwest Yukon study site (Figure 3-1) is bounded by the Yukon–Alaska border (141°W) on the west and southwest, the Yukon–British Columbia border on the south (60°N), 134°W on the east and 62.5°N on the north. Eastern portions of the study area are situated in the rain shadow of the St. Elias Mountain range caused by the easterly atmospheric circulation of air masses, originating in the Arctic Ocean, Gulf of Alaska and the Bering Sea, all of which are controlled by the position of the Aleutian Low (Trenbreth & Hurrell, 1994). However, this area receives enough annual precipitation (approximately 30–80 cm) that the semi-arid and arid landscape impediment to the function of the MODIS LST algorithm (Wan et al., 2002) is likely negligible. This region of the Yukon contains four Environment Canada meteorology monitoring stations situated near airports or airfields and located at elevations between 599 m and 807 m (Table 3-1). These stations provided diurnal temperature curves, which when used in conjunction with MODIS LST, were used to predict mean daily LST. Seven validation meteorological monitoring stations are located on barren, tundra and glaciated land cover at elevations between 1408 m and 2319 m (Table 3-1).

Methods

MODIS Version 5 Clear Sky Daytime Land Surface Temperatures (LST)

The MODIS LST data used in this study are the 1 km gridded clear-sky reprocessing version 5 MOD11A1 h11 v02 tile (ICM method) and MODIS Terra and Aqua (MOD11L2 and MYD11L2) LST swath data (MMM method). The 1 km gridded MODIS land surface temperature is produced using the split window technique (Wan et al., 2002) that uses MODIS bands 31 and 32 (10.78–11.28 μm and 11.77–12.27 μm respectively). This technique uses a global land surface emissivity derived look-up table (Snyder et al., 1998) to correct emissivity variations. MODIS data were downloaded from the Land Processes Distributed Active Archive Center–LPDAAC (<https://lpdaac.usgs.gov/>). The MOD11A1 data are produced from Land Surface Temperature (MOD11L2) swath data, which are dependent on several parameters related to the satellite platform and sensor and is generated using the Product Generation Executive (PGE16) code. The MOD11L2 data are comprised MODIS L1B calibrated and geolocated radiances, geolocation, cloud mask, atmospheric profiles, land and snow cover. The MOD11A1 product used in this study is produced by mapping daily single clear sky observation MOD11L2 swath data onto 1 km tiled grids in sinusoidal projection with an accuracy of 0.02 K.

Pre-Processing of MODIS Terra Tile and Terra and Aqua Swath Data

The version 5 MOD11A1 reprocessing data contain single observations in each grid cell, rather than averaged swath observations (averaged observations were contained in earlier reprocessing versions) where multiple inputs to grid cells from overlapping swaths occur. MODIS LST (MOD11A1) tile data can contain non-sequential and temporally disparate surface temperature data. Spatial subsets matching the study area were extracted from the 2008 MOD11A1 tile data. MOD11A1 LST and the coincident local solar View Time (VT) were reprojected from sinusoidal projection to 1 km gridded geotiff Albers Equal Area Projection, (WGS84) using nearest neighbour resampling (Dwyer & Schmidt, 2006). View time is extracted because surface temperature (and thus LST) is critically dependent on solar azimuth, and thus the time of day. These LST product layers were converted to local solar time and temperature using the conversion factors provided at <http://lpdaac.usgs.gov/modis>. The conversion of spatial subsets of the MODIS native local solar VT to local standard time requires longitude information for each grid cell. To facilitate conversion of view time from local solar time to local time, the view time layers were subdivided into 1° longitude bands, across which uniform time conversion was assigned. This procedure introduces error in local time, which is at a maximum of 2 min at whole number lines of longitude and decreases to zero at the half way line between whole number lines. Since the local solar time to local time conversion is dependent upon the day of year, a new conversion is required for each day of the year. Thus a different time conversion is applied to each daily one degree of longitude subset.

Lastly, LST was filtered for cloud contamination. We adopted an approach similar to that used by Reynolds *et al.* (2008) on AVHRR LST data for cloud masking of MODIS LST data. However we made several changes to complement the more robust cloud masking and better spatial resolution of MODIS LST data. If the MODIS LST grid cell in question was >4 K lower than the surrounding grid cells, it was eliminated from the analysis. Daily differencing was also applied to the ICM product. A difference of >5 K between the day in question and surrounding days determined elimination. This masking was implemented beyond the normal cloud mask to eliminate any anomalous values, such as those resulting from optical leaks (Benali *et al.*, 2012).

LST view time in the MOD11A1 tiles forms irregular temporal patterns (an example is presented in Figure 3-2) resulting from multiple daily imaging of the study area. Cloud cover is a frequent phenomenon in this part of the Yukon and results in areas with no data in the MODIS products (*i.e.*, the NoData values in Figure 3-2 largely result from cloud cover). For our study area between 1 April and 31 October 2008 the number of daily grid values containing no data compared to the total number of grids averaged $61\% \pm 26\%$ (1 standard deviation).

The 2008 MYD11L2 and MOD11L2 swath data were reprojected from sinusoidal projection to 1 km gridded geotiff Albers Equal Area Projection (WGS 84) using nearest neighbour resampling from separate geolocation and LST data files. This processing step was batch run using MODIS Swath Reprojection Tool available from the LPDAAC.

Meteorology Station Air Temperature Data

The 2008 air temperature data used to provide diurnal curves for the ICM model were recorded on the hour at four long-term Environment Canada meteorology monitoring stations (Figure 3-1) and were obtained from Environment Canada's National Climate Archive (http://www.climate.weatheroffice.gc.ca/Welcome_e.html). Seven meteorology monitoring stations located in the southwest Yukon (Figure 3-1) provided the validation data set and collect air temperature as hourly averages of measurements recorded on five minute intervals, except the Pika Camp station which collected air temperature on the hour. Three stations were located in altitudinal tundra, two stations on non-vegetated rocky outcrops, and two stations on glaciers (Figure 3-1). Air temperature was measured with Campbell Scientific HMP45 sensors (Campbell Scientific Inc., Logan, Utah). Air temperature was typically recorded at 2 m above ground to an accuracy of ± 0.1 °C. The validation data covered the 1 April to 31 October 2008 study period, except the Ruby Range North Station and John Creek Station data, which covered the period from 15 July to 31 October 2008. Table 3-1 provides information regarding the location, elevation and other characteristics of the four reference and seven validation meteorology station sites.

Interpolated Curve Mean Daily Surface Temperature (ICM)

Air temperatures recorded at Environment Canada stations in the southwest Yukon (2000 to 2008) were constrained in previous work to within 12 min of MODIS Terra LST observations from 8AM to 2PM local time; these produced strong linear

correlations between LST (MOD11A1) and measured air temperature relationships ($0.94 \leq R^2 \leq 0.96$) (Williamson et al., 2013). The time of daytime LST capture did not affect the LST to air temperature relationship, nor did the season in which it was collected. The strong linear correlations between daytime LST and air temperatures provide the theoretical basis for production of the Interpolated Curve Mean Daily Surface Temperature (ICM) model through the spatial interpolation of diurnal air temperature curve shape.

The ICM was constructed using daily air temperature curves from each of the four Environment Canada meteorology stations and spatially intersected MODIS LST and view time between 1 April and 31 October 2008. This procedure was composed of three steps (Figure 3-3), outlined in detail below. The first step created daily daytime air temperature curves that facilitated the conversion of daily LST to daily average LST values. The second step created a spatial interpolation of the four sets of curves and converted time of LST capture to a ratio of what the air temperature should be at that time to the daily air temperature average. The third step created the ICM product.

Step 1: Air temperature curves for each of the four Environment Canada meteorology station were produced from air temperatures, recorded on the hour, between 8 h and 14 h (Pacific Standard Time) for the days between 1 April and 31 October. This interval includes multiple MODIS Terra swaths which results in a wide range of LST capture times found within the MOD11A1 tile. Only those air temperature curves displaying a polynomial fit of $R^2 = 0.95$ or greater were retained (see Figure 3-4 for an example). These curves were fit with a polynomial curve between 2nd and 5th order, in a successive manner starting at 2nd order and working towards 5th order. The range of polynomial

curves was required because the 8 h to 14 h time interval produced curves with a range of inflection points and local troughs and peaks. The process of curve fitting stopped when the curve showed an R^2 value greater than or equal to 0.95. Due to abnormal atmospheric conditions (e.g., inversions), approximately 10% of the period indicated previously did not have curves greater than or equal to $R^2 = 0.95$, and so were omitted from this study.

Step 2: Four Thiessen polygons (polygons that are defined by one internal point each, where the sides of each polygon are closest to each internal point in relation to the other points) were created around the four Environment Canada stations (Figure 3-1). In each Thiessen polygon, the corresponding daily air temperature curve was used to determine what the air temperature should be at the time of LST capture for each MODIS grid cell contained within the Thiessen polygon. This value was then used to create a normalized dimensionless value by dividing into average daily air temperature (see Figure 3-4 for an example).

Step 3: The daily unitless values created in Step 2 were multiplied by the corresponding MODIS LST grid value to produce the ICM, which retained the same spatial resolution as the input MODIS LST data. MODIS LST over the study area was collected during the overpass time, not specifically on the hour as the Environment Canada station air temperature was. Therefore, to fully exploit the MODIS LST data, the curves in step one are required.

*Mean Daily Surface Temperature Calculated from Maximum and Minimum LST
(MMM)*

Daily mean LST was calculated as the average of maximum and minimum LST and retained the same spatial resolution as the input MODIS LST data. Maximum LST was determined through the following steps: (1) MODIS Aqua and Terra swaths that corresponded to within 1 h before and after solar noon at 61°N and 139.5°W were identified; (2) Images were processed as outlined in Section 3.2; (3) The maximum value from multiple daily images (2 to 4 depending on how the 90 min repeat orbital corresponds to the 2 h interval around solar noon) was selected for each 1 km grid cell. Minimum LST was determined through the following steps: (1) MODIS Aqua swaths that correspond to 2 h before dawn to dawn were selected. Due to orbital configurations only MODIS Aqua imaged the study area for the two predawn hours; (2) Image processing was undertaken as outlined in Section 3.2; (3) The minimum value for daily images was selected for each 1 km grid cell. Depending on how the satellite repeat orbit of ~90 min corresponds to the two hour dawn interval, 1 to 2 Aqua images were available with which to determine the minimum value. Minimum values were calculated for the period of 1 May to 31 August, as this is the period when two hours before dawn to dawn intersect with satellite coverage. During the remainder of the year at this latitude, dawn occurred too late in the day to coincide with MODIS Aqua coverage. Cloud contamination masking was performed in a similar manner to that for the ICM model as detailed in Section 3.2. A daily average was produced if both maximum and minimum values occurred on the same day. Lastly, the daily MMM product was aggregated to 8-day averages and compared to the coincident 8 day averages of air

temperature. An 8-day average was produced if at least one minimum and one maximum value occurred during the 8-day period, but not necessarily on the same day.

All GIS analysis and data manipulation was conducted with ESRI's ArcGIS 9.2. Statistical analysis was conducted using the R statistical software package (R Development Core Team, 2008).

Results

ICM validation showed statistically significant strong linear correlations ($0.72 \geq R^2 \geq 0.85$) with mean daily air temperature (Figure 3-5; Table 3-2). RMS errors ranged between 4.09 and 4.90 K (Table 3-2), which were approximately 1 to 2 K larger than typical when compared to air temperatures (Zaksek & Schroedter-Homscheidt, 2009). Variations in R^2 values did not correlate with distance of the interpolated diurnal curve form (Table 3-1) indicating factors other than spatial interpolation were playing a dominant role in correlation variability. The strength of the R^2 values correlated to land surface structure, with the largest R^2 values corresponding with glacier and sparsely vegetated surfaces, and the lowest R^2 values corresponding with sites with large relief in topography, tall shrubs and complex vegetation canopies (Tables 3-1 and 3-2). The steepest slopes and largest y-intercepts most consistently occurred on glaciers, and to a lesser degree on exposed rock (barren) that displayed high topographic relief. All of the validation data sets were contained in the Burwash Landing Thiessen polygon (Figure 3-1) for the ICM method and all are above tree-line.

The MMM show statistically significant strong linear correlations ($R^2 = 0.90$, RSME = 2.67 K) with mean daily air temperature (Figure 3-6; Table 3-2). However, only 44 out of a possible 1575 LST observations intersecting the seven air temperature monitoring stations, had maximum and minimum values originating on the same day (Table 3-3). The majority of the observations were from the predawn over the icefields, whereas the number of observations was roughly equal further to the east over the lower elevation tundra. Aggregating to 8-day averages had little effect on the number of LST values correlated to air temperature (Table 3-4). However, the aggregation did have a noticeable effect on the linear regression ($R^2 = 0.84$, RSME = 1.54 K), where the slope become flatter than the 1:1 line and the y-intercept became positive and increased by 1.6 °C compared to the daily MMM result. The RMS error reported here for daily and aggregated MMM method is similar to that reported elsewhere (Zaksek & Schroedter-Homscheidt, 2009).

Discussion

The simple process of temperature curve shape interpolation applied across large geographic areas defined by Thiessen polygon allocation produced Mean Daily Temperatures. The interpolation of diurnal air temperature curve at distances of 45–62 km from Burwash (A) station, is supported by spatial auto-correlation of LST values across distances of 100–300 km (Jin, 2000). The reduced requirement of LST data (e.g., one point instead of two or more daily points) in the ICM is important for regions where extensive cloud cover is a perennial concern and where the number of daily overpasses is reduced compared to high latitude locations. Although the average LST calculated

from minimum and maximum LST values (MMM method) provided better agreement with daily air temperature averages, the very small number of daily averages indicated that direct calculation of average LST was not always feasible for the study area. The ICM model should find application in many instances of land surface monitoring where available daily LST observations are insufficient represent measurements at dawn and solar noon. Regardless of which of the two above methods are considered, both methods require independent observations of air temperature and surface thermal infrared temperature, which cannot replace each other, even though they are strongly correlated.

The LST diurnal temperature curve is mostly, but not wholly, composed of absorbed radiation and atmospheric interactions (Jin & Dickinson, 1999; Trenbreth, 1984). The high measurement accuracy of the air temperature and MODIS LST is very small compared to RMSE values presented here, which indicates that the variability in the results is a function of a time lag difference in processes that affect LST and air temperature differently and not measurement error. The difference between ICM and daily average air temperature was likely the combination of several factors, including:

(1) Cloud contamination or surface cloud shadow likely contributed to variation in the ICM values because this method uses a single daily input compared to two inputs required for the MMM method, which has been shown to increase correlation to air temperature (Benali et al., 2012). Variation in LST was likely influenced by cloud contamination, which likely disproportionately affected the ICM product because of its dependence on observations of maximum LST (Ackerman et al., 1998). Furthermore, cloud shadow can cause differences in LST (Wang et al., 2008) across spatial and

temporal scales and might also contribute to the influence of cloud contamination in LST.

(2) Decoupling of air temperature and LST at higher temperatures, caused by low albedo vegetation cover, was likely playing a role in the high RMS error reported here, especially for the ICM product because its sole input originates from the warmest part of the day. This interpretation was supported by the two non-vegetated sites (glaciers) displaying the lowest RMSE values for the ICM. Meltwater ponds at the glacier sites are small compared to the LST grid cell. However the air temperature which was recorded over glacier, snow and ice was contained within a LST grid cell which contains high percentages of talus, is the probable reason for the large y-intercepts. As expected the MMM LST product had a lower RMS error likely due to the moderating effect of the minimum temperature. However, the daytime MODIS LST product has a larger confidence in identifying daytime cloud cover cloud mask compared to the night-time mask (Ackerman et al., 1998), which should act to minimize cloud contamination in the ICM product compared to the MMM product.

Error could include the moderating effect on LST caused by surface water in tundra environments (Langer et al., 2010) or soil heat or soil water storage (Westermann et al., 2011; Jin & Dickinson, 1999). Neither the validation sites, nor the Haines Junction Environment Canada monitoring site contained large bodies of water within the MODIS grid cells. Nevertheless, the effects of small and ephemeral surface water bodies on soil heat or water storage remain unaccounted for in both models. Another error could be the larger error in daytime LST caused by angular anisotropy (Pinheiro et al., 2004) when compared with night time LST. The larger RMS error values reported for the ICM

product (compared to the MMM which included pre-dawn minimum LST values) likely accentuates angular effects, where the MMM minimizes them.

The differences in slope and y-intercept values between the daily average and the 8-day aggregation results from cloud cover influence of LST observations used in the 8-day period. The daily MMM values are calculated from the same day that has both clear sky minimum and maximum values, which suggests there is little cloud influence compared to the 8-day aggregation. Because the majority of values used in the 8-day aggregation did not have matching daily maximum or minimum values, we can deduce that cloud cover is influencing the LST value to a greater extent than the MMM method. This interpretation is supported by the 8-day values being warmer than the daily values when the temperature was below 0 °C and colder than the daily values when the temperature was above 0 °C. This effect should be considered when aggregating LST values for comparison to air temperature.

Application of the two models presented here can provide a relatively high-resolution (1 km) spatial/climatic product with which to evaluate the glacier surface processes and tundra dynamics in the sub-Arctic, either on their own or in conjunction with other modelled products in a gap filling capacity. For low statured Arctic vegetation, LST is documented relationships between leaf temperature and photosynthesis of Arctic tundra plants (Chapin, 1983).

Although improvements in cloud masking will reduce the negative effects of cloud contamination in LST data as a whole, the cost in terms of the reduction of data availability and quality could be significant in areas of the cryosphere that experience large amounts of cloud cover. Future work should be devoted to the identification of

cloud contaminated LST data and the degree to which contaminated LST values are affected. By quantifying the degree of contamination, data volume will be preserved and quality improved. Furthermore, the effect that different LST aggregation schemes have on the aggregated products should also be investigated with consideration being given to land cover and regional climate. Statistical techniques such should be investigated to make the most use of limited ground station data. The implementation of the ICM method for every LST observation could provide a powerful technique to fill gaps and aggregate LST data. Integration with interpolated air temperature products or other forms of surface temperature, such as passive microwave, could provide other sources of data. However, mismatches in spatial and temporal scale will pose challenges, especially when trying to mitigate the influence of persistent cloud cover.

Conclusions

Mean Daily Surface Temperature modelled from (1) MODIS LST tile data and interpolated daily air temperature curve shape (ICM) and (2) MODIS maximum and minimum data were compared to mean air temperatures from seven alpine locations covering tundra, talus and glacier land cover and elevations between 1408 m and 2319 m. The correlations at the seven locations for the ICM method were strong (R^2 values between 0.72 and 0.85) and all the correlations displayed positive slopes and y-intercepts. RMS errors ranged between 4.09 and 4.90 °C. The average LST calculated from the MMM algorithm had an even stronger correlation with air temperature ($R^2 = 0.90$) and smaller variability (RMSE = 2.67 K) compared with the ICM. However, very few daily averages were produced with the MMM method because of almost continuous

cloud cover over the study area. The aggregation of MMM to 8-day LST averages produced similar results as the daily averages ($R^2 = 0.84$; RMSE = 1.54 K), but had a warmer y-intercept and flattened slope, which is most likely the result of the insulating effect of clouds. Our results indicate that the ICM is a viable gap filling technique for situations where only single observations of day-time LST are available, but the daily average of maximum and minimum LST values produce a better result compared to air temperature. Finally, the common practice of aggregation of daily LST values to 8-day averages requires further research to determine the effect of cloud cover and land cover on this product and how it is applied.

Table 3-1: Description and location of meteorology stations in southwest Yukon.

Station	Elevation (m)	Lat./Long.	Description	Measurement Frequency	Distance to Burwash (km)
Whitehorse (A)	706	60.71°N; 135.07°W	Environment Canada Monitoring Station	On the Hour	NA
Haines Junction	599	60.77°N; 137.58°W	Environment Canada Monitoring Station	On the Hour	NA
Carmacks	542	62.12°N; 136.19°W	Environment Canada Monitoring Station	On the Hour	NA
Burwash (A)	807	61.37°N; 139.05°W	Environment Canada Monitoring Station	On the Hour	NA
John Creek	1408	61.20°N; 138.25°W	Grass meadow surrounded by tall shrubs in large patches, little exposed bedrock	Hourly average of 5 minute readings	47.1
Ruby Range – North	1926	61.25°N; 138.19°W	Sparse vegetation, much exposed bedrock, no shrubs	Hourly average of 5 minute readings	48.5
Pika Camp	1635	61.21°N; 138.28°W	Grass and sparse low shrub, little exposed rock	On the Hour	45.0
Transect Canada Creek	2184	60.88°N; 138.97°W	Sparse vegetation, much exposed bedrock, no shrubs	Hourly average of 5 minute readings	55.4
Transect Duke River	2214	60.94°N; 138.90°W	Sparse vegetation, much exposed bedrock, no shrubs	Hourly average of 5 minute readings	49.0
South Glacier	2280	60.82°N; 139.13°W	Glacier	Hourly average of 5 minute readings	61.8
North Glacier	2319	60.91°N; 139.16°W	Glacier	Hourly average of 5 minute readings	51.2

Table 3-2: Coefficient of determination (R^2), root mean square error (RMSE) and skew between daily air temperature averages and modeled mean daily surface temperature (ICM & MMM).

Station - Model	R^2	RMSE (K)
South Glacier – ICM	0.86	4.09
North Glacier – ICM	0.82	4.13
Transect Duke River – ICM	0.72	4.62
Transect Canada Creek – ICM	0.76	4.90
John Creek – ICM	0.72	4.36
Ruby Range North – ICM	0.77	4.15
Pika Camp – ICM	0.80	4.53
All Stations – MMM	0.90	2.67
All Stations – MMM (8 day Composite)	0.84	1.54

Table 3-3: Number of daily minimum and maximum values observed and calculated (mean) for seven meteorology stations for period between May 1 and August 31, 2008.

Station	Maximum Count	Minimum Count	Mean Count
South Glacier	4	42	2
North Glacier	7	50	3
Transect Duke River	12	50	7
Transect Canada Creek	7	60	5
John Creek	25	27	12
Ruby Range North	25	23	6
Pika Camp	20	31	9

Table 3-4: Number of 8-day composite values observed and calculated (mean) for seven meteorology stations for period between May 1 and August 31, 2008.

Station	Maximum Count	Minimum Count	Mean Count
South Glacier	2	14	2
North Glacier	4	16	4
Transect Duke River	6	16	6
Transect Canada Creek	5	16	5
John Creek	12	13	11
Ruby Range North	11	13	9
Pika Camp	15	12	11

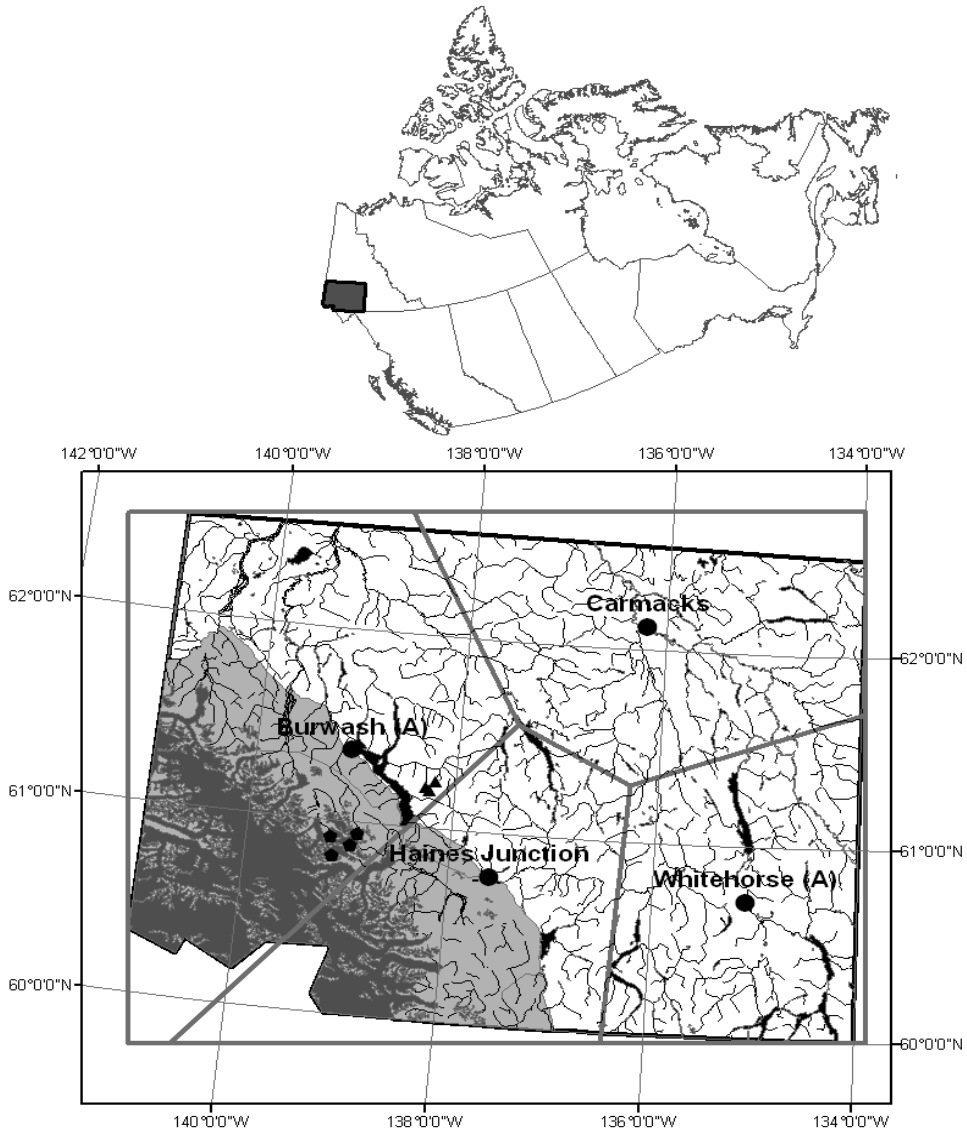


Figure 3-1: Southwest Yukon study area including the location of Environment Canada meteorology recording stations (Circles) and validation meteorology recording stations (Tundra–Triangles; Barren or Glacier–Pentagons). The light grey shaded region in the bottom left of the study area is Kluane National park. The darker shaded region within Kluane Park is the St. Elias Icefield. The four irregular polygons are Thiessen polygons derived from locations of Environment Canada meteorology stations.

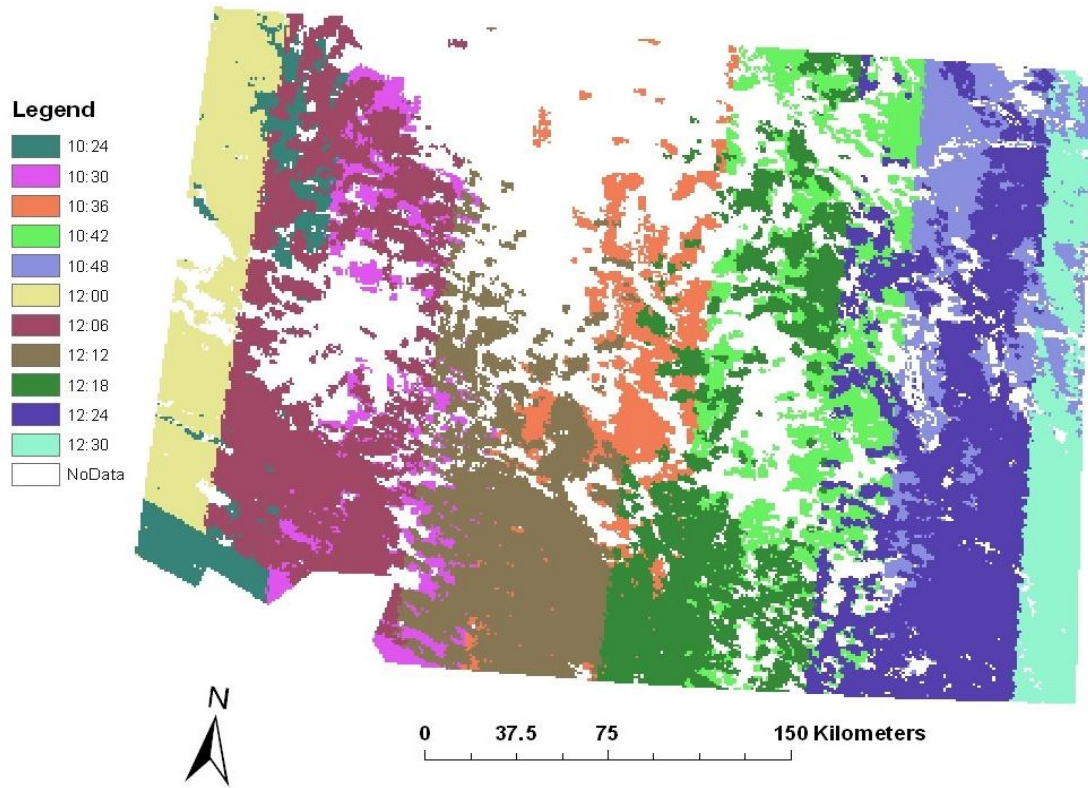


Figure 3-2: Solar View Time for MODIS Terra LST (MOD11A1) observations from 18 April, 2008, covering the southwest corner of the Yukon Territory.

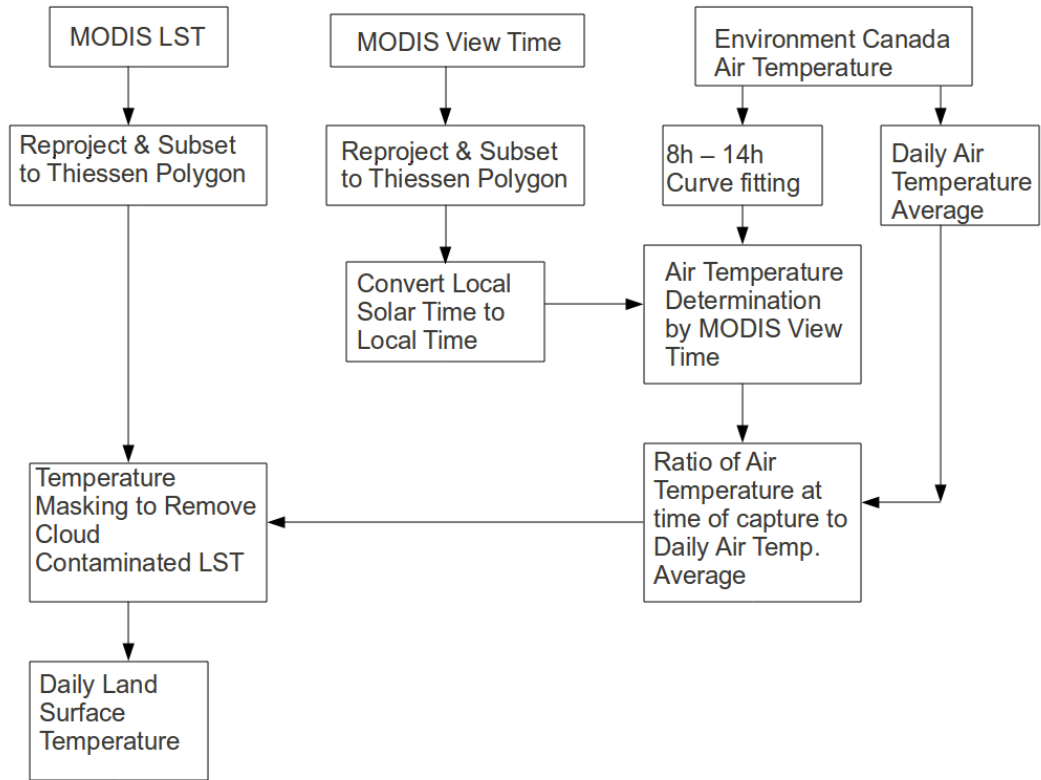


Figure 3-3: Mean Daily Surface Temperature (ICM) Algorithm flow diagram, describing how MODIS LST and air temperature records are combined to produce a mean daily surface temperature.

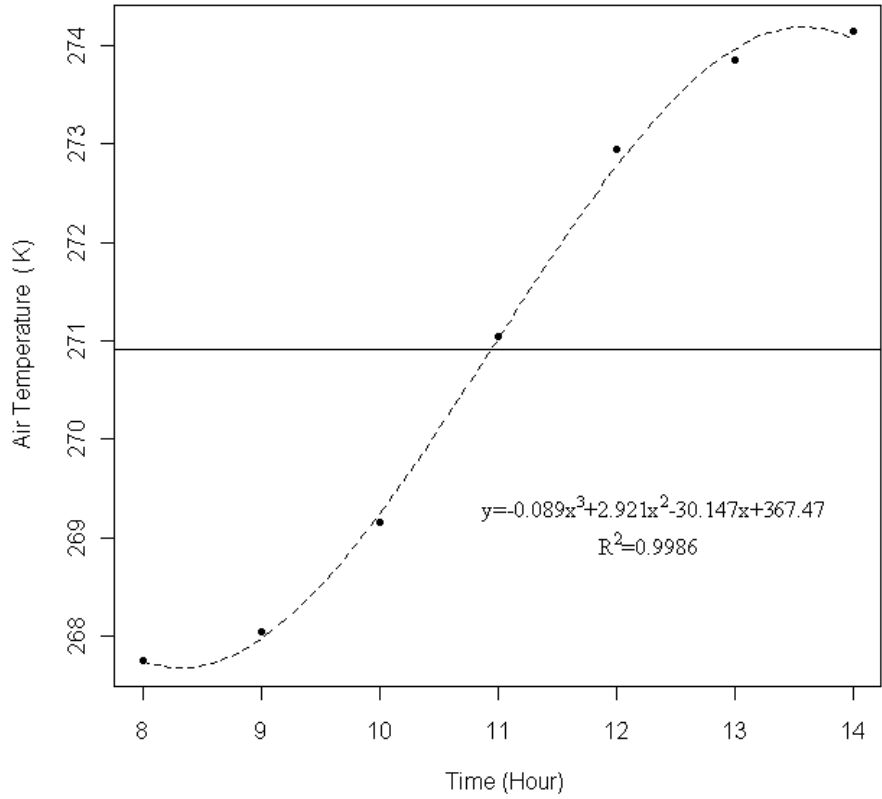


Figure 3-4: Air temperature between 8 AM and 2 PM at Whitehorse on 20 October 2008. The dashed line indicates the polynomial trend line and the solid line (270.9 K) indicates the average air temperature between 12:01 AM and 11:59 PM on 20 October 2008. Hour on the x axis indicates time in hours.

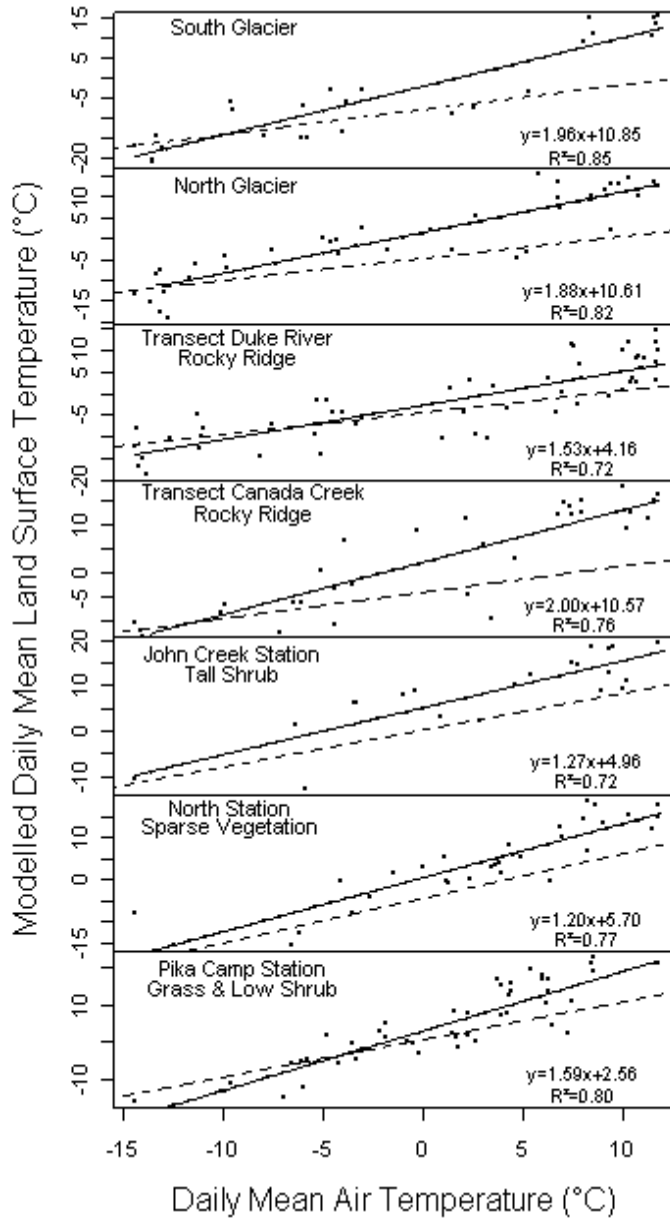


Figure 3-5: Modeled Mean Daily Surface Temperature (ICM) *versus* mean daily air temperature at non-vegetated glacier and rocky ridge locations in the flanks of the St. Elias Mountains and at vegetated sites (John Creek Station, Ruby Range North Station, and Pika Camp Station) east of Kluane Lake. The dashed lines indicate the 1:1 lines; the solid lines indicate the linear trends.

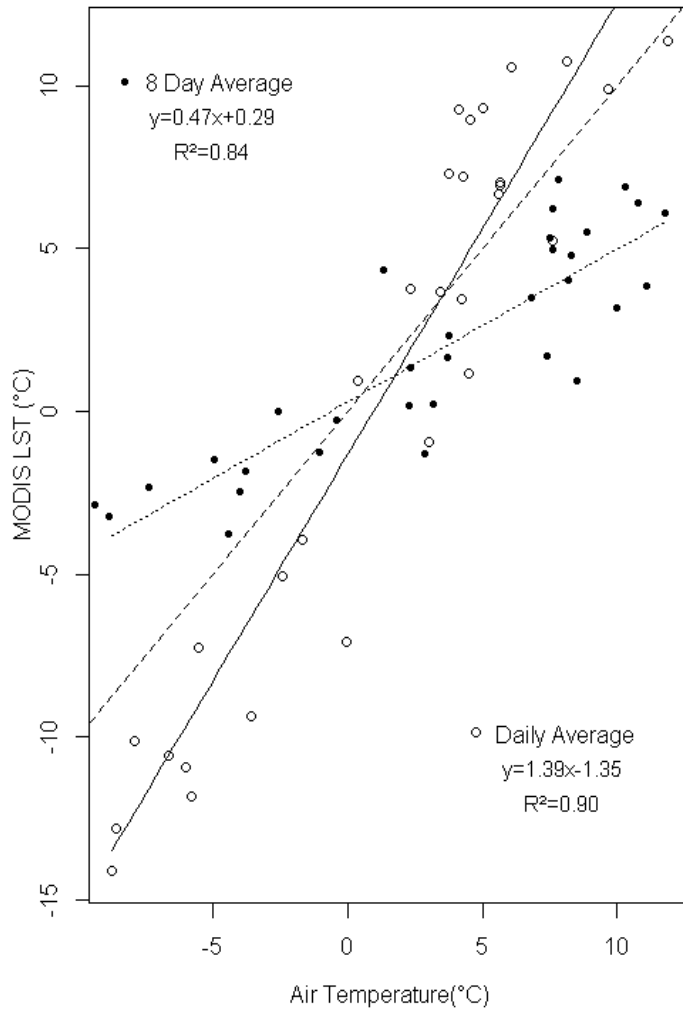


Figure 3-6: Daily mean Land Surface Temperature computed from maximum and minimum daily LST (MMM) compared to daily average air temperature calculated from hourly means at seven stations in the southwest Yukon (open circles and the solid line is the linear trend). The 8-day LST was computed from maximum and minimum daily values (closed circles, and the dotted line is the linear trend). The dashed line indicates the 1:1 line.

References

- ACIA (Arctic Climate Impact Assessment). *Impacts of a warming Arctic–Arctic Climate Impact Assessment*; Cambridge University Press: Cambridge, United Kingdom, 2004. Available online: <http://www.acia.uaf.edu> (accessed on 22 April 2013).
- Ackerman, S.A., Strabala, K.I., Menzel, W.P., Frey, R.A., Moellerand C.C., & Gumley, L.E. (1998). Discriminating clear sky from clouds with MODIS. *Journal of Geophysical Research*, **103**, 32141–32157.
- Ackerman, S.A., Holz, R.E., Frey, R., Eloranta, E.W., Maddux, B.C., & McGill, M. (2008). Cloud detection with MODIS. Part II: Validation. *Journal of Atmospheric and Oceanic Technology*, **25**, 1073–1086.
- Benali, A., Carvalho, A.C., Nunes, J.P., Carvalhais, N., & Santos, A. (2012). Estimating air surface temperature in Portugal using MODIS LST data. *Remote Sensing of Environment*, **124**, 108–121.
- Bhatt, U.S., Walker, D.A., Reynolds, M.K., Bieniek, P.A., Epstein, H.E., Comiso, J.C., Pinzon, J.E., Tucker, C.J., & Polyakov, I.V. (2013). Recent declines in warming and vegetation greening trends over pan-Arctic tundra. *Remote Sensing*, **5**, 4229–4254.
- Chapin, F.S. (1983). Direct and indirect effects of temperature on Arctic plants. *Polar Biology*, **2**, 47–52.
- Comiso, J.C. (2003). Warming trends in the Arctic from clear sky satellite observations. *Journal of Climate*, **16**, 3498–3510.

- Crosson, W.L., Al-Hamdan, M.Z., Hemmings, S.N.J., & Wade, G.M. (2012). A daily merged MODIS Aqua-Terra land surface temperature data set for the conterminous United States. *Remote Sensing of Environment*, **119**, 315–324.
- Dwyer, J., & Schmidt, G. (2006). The MODIS Reprojection Tool. In *Earth Science Satellite Remote Sensing*, Qu, J.J., Gao, W., Kaftos, M., Murphy, R.E., Salmonson, V.V., Eds., Springer Berlin Heidelberg: Berlin Heidelberg, Germany, pp. 162–177.
- Grace, J., Berninger, F., & Nagy, L. (2002). Impacts of climate change on the tree line. *Annals of Botany*, **90**, 537–544.
- Holdridge, L.R. (1967). *Life Zone Ecology*, Tropical Science Center: San Jose, Costa Rica.
- Intergovernmental Panel on Climate Change (IPCC). *Summary for policy makers*. In Solomon, S. and 7 others (Eds.) *Climate change 2007: the physical science basis. Contribution of Working Group I to the Fourth Assessment Report of the Intergovernmental Panel on Climate Change*. Cambridge, etc., Cambridge University Press, 2007.
- Jin, M. (2000). Interpolation of surface radiation temperature measured from polar orbiting satellites to a diurnal cycle. 2. Cloudy pixel treatment. *Journal of Geophysical Research*, **105**, 4061–4076.
- Jin, M., & Dickinson, R.E. (1999). Interpolation of surface radiative temperature measured from polar orbiting satellite to a diurnal cycle. Part 1: Without clouds. *Journal of Geophysical Research*, **104**, 2105–2116.

- Jin, M., & Dickinson, R.E. (2000). A generalized algorithm for retrieving cloudy sky skin temperature from satellite thermal infrared radiances. *Journal of Geophysical Research*, **105**, 27037–27047.
- Jin, M., & Treadon, R.E. (2003). Correcting orbit drift effects of AVHRR on Skin Temperature Measurements. *International Journal of Remote Sensing*, **24**, 4543–4558.
- Langer, M., Westermann, S., & Boike, J. (2010). Spatial and temporal variations of summer surface temperatures of wet polygonal tundra in Siberia—implications for MODIS LST base permafrost monitoring. *Remote Sensing of Environment*, **114**, 2059–2069.
- Lugo, A.E., Brown, S.L., Dodson, R., Smith, T.S., & Shugart, H.H. (1999). The Holdridge life zone of the conterminous United States in relation to ecosystem mapping. *Journal of Biogeography*, **26**, 1025–1038.
- Pinheiro, A.C.T., Privette, J.L., Mahoney, R., & Tucker, C.J. (2004). Directional effects in a daily AVHRR land surface temperature dataset over Africa. *IEEE Transactions on Geoscience and Remote Sensing*, **42**, 1941–1954.
- Post, E., Forchhammer, M.C., Bret-Harte, M.S., Callaghan, T.V., Christensen, T.R., Elberling, B., Fox, A.D., Glig, O., Hik, D.S., Hoye, T.T., *et al.* (2009). Ecological dynamics across the Arctic associated with recent climate change. *Science*, **325**, 1355–1358. doi:10.1126/science.1173113.
- R Development Core Team. (2008). R: A language and environment for statistical computing. R foundation for Statistical Computing: Vienna, Austria. ISBN 3-

900051-070-0. Available online: <http://www.R-project.org> (accessed on 30 October 2013).

Raynolds, M.K., Comiso, J.C., Walker, D.A., & Verbyla, D. (2008). Relationship between satellite-derived land surface temperatures, Arctic vegetation types, and NDVI. *Remote Sensing of Environment*, **112**, 1884–1894.

Sellers, W.D. (1965). *Physical Climatology*, University of Chicago Press: Chicago, IL, USA, p. 272.

Snyder, W.C., Wan, Z., Zhang, Y., & Feng, Y.Z. (1998). Classification-based Emissivity for land surface temperature measurement from space. *International Journal of Remote Sensing*, **19**, 2753–2774.

Snow, Water, Ice, Permafrost in the Arctic (SWIPA). (2011). Available online: <http://amap.no/swipa/> (accessed on 20 April 2013).

Soliman, A., Duguay, C., Saunders, W., & Hachem, S. (2012). Pan-Arctic land surface temperature from MODIS and AASTR: Product development and intercomparison. *Remote Sensing*, **4**, 3833–3856.

Sun, J., Salvucci, G.D., & Entekhabi, D. (2012). Estimates of evapotranspiration from MODIS and AMSR-E land surface temperature and moisture over the Southern Great Plains. *Remote Sensing of Environment*, **127**, 44–59.

Trenberth, K.E. (1984). Some effects of finite sample size and persistence on meteorological statistics, II, Potential predictability. *Monthly Weather Review*, **112**, 2369–2379.

Trenberth, K.E., & Hurrell, J.W. (1994). Decadal atmosphere-ocean variability in the Pacific. *Climate Dynamics*, **9**, 303–309.

- Vancutsem, C., Ceccato, P., Dinku, T., & Connor, S.J. (2010). Evaluation of MODIS land surface temperature data to estimate air temperature in different ecosystems over Africa. *Remote Sensing of Environment*, **114**, 449–465.
- Vincent, L.A., & Mekis, E. (2006). Changes in daily and extreme temperature and precipitation indices for Canada over the twentieth century. *Atmosphere-Ocean*, **44**, 177–193.
- Wan, Z., Zhang, Y., Zhang, Q., & Li, Z. (2002). Validation of the land-surface temperature product retrieved from Terra Moderate Resolution Imaging Spectroradiometer data. *Remote Sensing of Environment*, **83**, 163–180.
- Wan, Z. (2008). New refinements and validation of MODIS land-surface temperature/emissivity products. *Remote Sensing of Environment*, **112**, 59–74.
- Wang, W., Liang, S., & Meyers, T. (2008). Validating MODIS land surface temperature products using long-term nighttime ground measurements. *Remote Sensing of Environment*, **112**, 623–635.
- Wang, X., & Key, J.R. (2003). Recent trends in Arctic surface, cloud, and radiation properties from space. *Science*, **299**, 1725–1728.
- Wenbin, Z., Aifeng, L., & Shaofeng, J. (2013). Estimation of daily maximum and minimum air temperature using MODIS land surface temperature products. *Remote Sensing of Environment*, **130**, 62–73.
- Westermann, S., Langer, M., & Boike, J. (2011). Spatial and temporal variations of high-Arctic tundra in Svalbard—Implications for MODIS LST based permafrost monitoring. *Remote Sensing of Environment*, **115**, 908–922.

Williamson, S.N., Hik, D.S., Gamon, J.A., Kavanaugh, J.L., & Koh, S. (2013).

Evaluating cloud contamination of clear-sky MODIS Terra daytime Land Surface Temperatures using ground-based meteorology station observations. *Journal of Climate*, **26**, 1551–1560.

Zaksek, K., & Schroedter-Homscheidt, M. (2009). Parameterization of air temperature in high temporal and spatial resolution from a combination of SEVIRI and MODIS instruments. *ISPRS Journal of Photogrammetry and Remote Sensing*, **4**, 414–421.

CHAPTER FOUR

Night-Time Cloud Cover over Snow Covered Mountainous Terrain Produces an Inherent Cold Bias in MODIS LST when compared to Average Air Temperature

Introduction

Northern Hemisphere high latitudes, particularly in Yukon and Alaska, have warmed on average between 1 – 3 °C over the last 50 years (Arctic Climate Impact Assessment – ACIA, 2005; Snow, Water Ice, Permafrost in the Arctic - SWIPA, 2011). This warming is coincident with North American snow cover reduction and amplified warming at high latitudes (Serreze et al., 2009). Instrumental air temperature measurements are commonly used for trend estimation and validation of downscaled and remote sensing products. This method suffers from several limitations which include sparse or sporadic instrumental measurements and heterogeneously placed monitoring locations, typically at valley bottom in mountainous terrain (Vincent & Mekis, 2006; Robeson, 1995). The generation of continuous spatial temperature products from point measurement requires interpolation, after which downscaling can be applied to produce a higher spatial resolution product. The interpolation and subsequent downscaling of air temperature measured at stations throughout western Canada is becoming common, with several groups recently providing similar products for much of western North America {e.g., Scenarios Network for Alaska and Arctic Planning (SNAP) – <http://www.snap.uaf.edu/> }.

Interpolated surface temperature products are important climate metrics as they

have a relatively long time period compared to the modern satellite record of surface temperature using infrared temperature or passive microwave. Downscaled air temperature interpolation can be produced at much higher spatial resolution than passive surface temperature measurement (infrared and microwave) and are not reliant on emissivity correction or, more importantly, clear sky. The use of high spatial resolution infrared derived satellite measurements of surface temperature (e.g., Comiso, 2003) is an increasingly common method for trend analysis due to the progressively longer period over which these measurements have been acquired. The launch of the MODerate resolution Imaging Spectroradiometer (MODIS) in early 2000s marked a change toward an increase in data quality and quantity of thermal data, which will fundamentally change the measurement of surface temperature. This is especially true as Earth observing satellites have proliferated since the introduction of MODIS. The new sensors and satellite platforms are better equipped to provide an improved treatment of many longstanding problems, such as orbital drift, cloud contamination, emissivity assessment and poor spatial resolution that made (and still make) the interpretation of satellite imagery difficult, especially in relation to air temperature (Jin & Dickenson, 2010).

Infrared satellite observations are ‘clear sky’ which provides a version of surface temperature that is skewed to a specific set of atmospheric and surface illumination conditions. Furthermore, infrared satellite observations of the Earth are dependent on the time of capture, and require conversion to more generalised metrics such as daily averages to increase their utility. Jin and Dickinson (1999) indicated that maximum daily infrared temperature under clear sky conditions will correspond to peak solar

insolation with a small adjustment for phase lag. Thus maximum surface temperature will occur when the post solar noon incoming radiation is balanced by outgoing radiative loss, or zero net radiation, and might occur up to several hours after solar noon. Satellite surface infrared temperature values acquired several hours after solar noon will provide the highest correlations to air temperature because of the radiative surface heating and upward heat fluxes (Oke, 1987); minimum surface infrared temperature will occur near sunrise (Sellers, 1965). Westermann et al. (2012) found that on Svalbard the incorporation of winter time minimum LST into longer-term averages caused a cold bias compared to thermal infrared measurements made in-situ at ground level. This phenomenon is caused by cloud cover increasing the average minimum surface temperature, compared to the clear sky satellite observations of infrared MODIS Land Surface Temperature.

Much recent work has focused on defining the relationship between air temperature and infrared surface temperature although they are in fact separate physical entities that respond to the same forcing over different time scales (Jin & Dickensen, 2010). Strong correlations between infrared surface temperature (Land Surface Temperature or LST) and air temperatures for many vegetated land cover types typically produce an error between LST and air temperature of approximately 2-3 °C (Zaksek et al., 2009) irrespective of the methodology, spatial or temporal resolutions. Limited comparisons between satellite remote sensing of infrared surface temperature and NARR are available (Royer and Poirier, 2010), indicating a 1 °C warm bias in NARR compared to microwave surface temperature for snow free conditions. Both the microwave surface temperatures and NARR were conducted at a coarse spatial

resolution of 25 and 32 km grid cells respectively.

MODIS provides a measure of snow cover using an algorithm based on the normalised difference snow index (NDSI), normalised difference vegetation index for forested areas, a thermal mask and cloud mask (Hall et al., 2002). The snow cover product used in this study is the MODIS Terra daily fractional snow cover product produced at 500 metre resolution (MOD10A1) determined through regression equations of NDSI and fractional snow cover (e.g., Salomonson & Appel, 2004). The MODIS sensor on the AQUA platform uses band 7 in the NDSI algorithm instead of band 6 as used on MODIS Terra. This causes some poorer accuracy in the AQUA snow products (Hall & Riggs, 2007), but the detection of thin snow (< 1 cm) is also problematic for the MODIS sensor in general. The average root mean square error for MODIS Terra derived fractional snow cover across four mountain ranges is 5% and retrieval seems to be mostly insensitive to solar zenith angle (Painter et al, 2009). In alpine meadows, where the forest canopy is minimal, MODIS fractional snow cover is almost identical to *in situ* estimates of snow cover and higher spatial resolution satellite estimates, however forest canopies obscure the ground and cause an observed value of snow fraction to be less than true values (Raleigh et al., 2013). At high elevation sites in the Tibetan Plateau, MODIS snow cover shows a 90% overall accuracy when related to *in situ* measurements (Pu et al., 2007).

Our objective was to identify the differences between monthly average infrared LST and two types of downscaled temperature fields for the southwest Yukon region. The relationships between these measures of temperature are investigated in relation to land cover, elevation, snow cover and number of LST measurements for each month

during May to August in 2008. Downscaled temperatures and maximum and minimum LST values were also compared to nine high elevation meteorological stations that were not used in the production of any of the above temperature products.

Study Area

The southwest Yukon study site (Figure 4-1) is bounded by the Yukon – Alaska border on the west (141 °W) and southwest, Yukon – British Columbia border on the south (60°N), 138 °W on the east and 62 °N on the north. The southeast portion of the study area is bounded between the points 60 °N, 138 °W and 60.3 °N, 136.5 °W. The north east side of the study area is bounded between the points 62 °N, 141 °W and 62.5 °N, 138.5 °W. The study area, which encompasses 10,558 2 km by 2 km grid cells, has a large negative west to east elevation gradient of ~5,000 m over ~120 km resulting in diverse land-cover types. The geographical extent of the study area was chosen to minimise the effect of differences in solar illumination and duration across the longitudinal and latitudinal extent of a MODIS swath, and thus keep the measurements of LST close to solar noon and dawn.

A world-wide landscape classification (GLOBCOVER) was completed in 2009 by the European Space Agency using MERIS 300 m resolution imagery (<http://due.esrin.esa.int/globcover/>). This land cover product was used to subset the study area. Of the 23 potential global land cover classes, 11 exist within the study area. These are Closed needleleaved evergreen forest; Open needleleaved deciduous or evergreen forest; Closed to open mixed broadleaved and needleleaved forest; Mosaic

Forest-Shrubland/Grassland; Mosaic Grassland/Forest-Shrubland; Closed to open shrubland; Closed to open grassland; Sparse vegetation; Bare areas; Water bodies; Permanent snow and ice. These classes were reduced to six by aggregating similar classes in terms of stature and functional type and removing water bodies. The six classes, including areal extent in parentheses, retained for analysis are: 1) Closed and Open needleleaved and needleleaved deciduous forest (6,844 km²); 2) Closed to Open mixed broadleaved and needleleaved forest(1,956 km²); 3) Mosaic Forest-Shrubland/grassland – Mosaic Grassland/Forest-Shrubland – Closed to open shrubland (4,108 km²); 4) Closed to open grassland (5,040 km²); 5) Sparse vegetation – Bare areas (13,420 km²); 6) Permanent snow and ice (10,268 km²). These six classes generally increase in average elevation from conifer dominated class 1 at 936 m, through 1,114 m (class 2), 1,186 m (class 3), 1,165 m (class 4), 1,655 m (class 5) and 2,325 m (class 6).

The study area contains two Environment Canada meteorology monitoring stations which provide data to the public and are situated at airfields at Burwash Landing and Haines Junction within Conifer land cover (Closed and open needleleaved forest) and located at elevations of 807 m and 599 m, respectively. Nine independent meteorological stations (Table 4-1) are located within the study located between elevations of 1408 – 2690 m, on Barren or Permanent Snow and Ice land covers provide hourly air temperature measurements which are compared to the intersecting temperature product grid cell.

LST is measured by the MODIS sensor on the Terra and Aqua platforms. These satellites are in near polar orbits, which dictate a swath overlap at latitudes greater than 30°, and thus produce progressively more daily observations toward each pole. MODIS

data became available in February 2000 for Terra and July 2002 for Aqua. A full earth sun-synchronous, near-polar, circular orbit for both platforms requires 90 minutes to complete, with the Terra descending orbit's equatorial crossing at 10:30 AM local time and Aqua's ascending orbit crossing the equator at 1:30 PM local time. The orbitals dictate both Terra and Aqua over pass the southwest Yukon during solar noon, whereas Aqua over passes before dawn. The choice of May through August was determined by the MODIS Aqua satellite, because this is the only period where observations coincided with 2 hours before dawn to dawn. In the months after August to the winter solstice the time of dawn progressively occurs later in the day, meaning that the observations by the Aqua satellite are occurring earlier than dawn because dawn is occurring later each day. The Terra and Aqua satellite overpasses overlap within 1 hour of solar noon in the study area latitudinal and longitudinal range. Using the 1 hour of solar noon provides a maximum overpass density, while minimising the daily variability in LST values. Although we call this value maximum LST, it is likely slightly less than the actual daily maximum which will occur when the net radiation at surface reaches zero. The timing of the daily maximum will vary by day but likely occurs after the Aqua overpass, which images the ground up to an hour later in the day than Terra.

Methods

Processing MODIS data

The MODIS LST data used in this study are the 1 km gridded clear-sky reprocessing MODIS Terra and Aqua (MOD11L2 and MYD11L2) LST swath data.

The 1 km gridded MODIS land surface temperature is produced using the split window technique (Wan et al. 2002; Wan 2008) that uses MODIS bands 31 and 32 (10.78 – 11.28 μm and 11.77 – 12.27 μm respectively). This technique uses a global land surface emissivity derived look-up table (Snyder et al. 1998) to correct for atmospheric and emissivity variations. MODIS data were downloaded from the Land Processes Distributed Active Archive Center – LPDAAC (<https://lpdaac.usgs.gov/>). The MOD11L2 data are composed of geolocation, sensor radiance data, atmospheric temperature and water profile, cloud mask, quarterly land cover, and snow cover MODIS products. Our use of the daytime MODIS LST product results from the larger confidence in the daytime cloud mask compared to the night-time mask (Ackerman et al. 1998), which reduces the potential for cloud contamination.

The LST was filtered for grid cells that showed anomalous values, caused by cloud or cloud shadow contamination or large view angles (Benali et al., 2012). We adopted an approach similar to that used by Reynolds et al. (2008) on AVHRR LST data for cloud masking of MODIS LST data. If a MODIS LST grid cell was <5 K than the average of the surrounding values within 2 km radius, or >3 K different than the standard deviation, it was eliminated from the analysis.

The 2008 MYD11L2 and MOD11L2 swath data were reprojected from sinusoidal projection to 1 km Albers Equal Area Projection (WGS84) using nearest neighbour resampling. This processing step was batch run using MODIS Swath Reprojection Tool available from the LPDAAC.

Calculating mean monthly surface temperature from daily maximum and minimum LST

Daily mean LST was calculated as the average of maximum and minimum LST and retained the spatial resolution of the input MODIS LST data. Maximum LST was determined (i) by identifying MODIS Aqua and Terra swaths that corresponded to within 1 h before and after solar noon at 61° N and 139.5° W; and (ii) selecting the maximum value from multiple images for a given day (2 to 4 depending on how the 90 minute repeat orbital corresponds to the 2 hour interval around solar noon) for each 1 km grid cell. Minimum LST was determined (i) by identifying MODIS Aqua swaths that correspond to the 2 hours before dawn. Due to orbital configurations only MODIS Aqua imaged the study area for the two predawn hours; and (ii) selecting the minimum value for daily images for each 1 km grid cell. Depending on how the satellite repeat orbit of ~90 minutes corresponds to the two hour predawn interval, 1 to 2 Aqua images were available with which to determine the minimum value. Minimum values were calculated for the period of 1 May to 31 August, as this is the period when two hours before dawn to dawn intersect with satellite coverage. During the remainder of the year at this latitude, dawn occurred too late in the day to coincide with MODIS Aqua coverage. Monthly averages maximum and minimum were calculated from available values, after which the data was resampled to 2 km grid cells using an arithmetic average.

MODIS Snow cover

Daily snow cover was derived from the MODIS Terra 500 m fractional snow

cover (MOD10A1) and resampled to 2 km grid cells using an arithmetic average of the 16 possible values, ignoring missing values. The daily maps of 2 km snow cover were aggregated to monthly averages showing a value of 0-100% for each aggregated grid cell for each month.

Scenarios Network for Alaska + Arctic Planning (SNAP) air temperature

The SNAP air temperature product applies the delta method of statistical downscaling (Prudhomme et al., 2002) to 1910 – 2009 CRU data (Climate Research Unit – University of East Anglia) using the 1961-1990 Parameter-Regression on Independent Slopes Model (PRISM) model (Daly et al., 1994) data as the baseline climate. The monthly mean air temperature is gridded at a 2 km resolution for the southwest Yukon.

NCEP North American Regional Re-analysis (NARR) downscaling

An alternative downscaling method uses an interpolation scheme that reconstructs vertical temperature profiles from a North American Regional Reanalysis (NARR) and does not require meteorological station measurements for tuning. NARR is produced by the National Center for Environmental Prediction (NCEP), and makes use of surface, radiosonde, and satellite data, which are combined in the Eta forecasting system (Mesinger et al., 2006). This method was developed by Jarosch et al. (2012) for western Canada, with the specific intent of producing a temperature product that is more

accurate than other products for high elevation, high vertical relief glaciated areas. This product, which is a mix of statistical and dynamical downscaling methods applied to NARR 500 mbar air temperature, uses two-part, piece-wise fitting to NARR vertical air profiles and subsequent interpolation of those fitting parameters to a 200 m grid for prediction of temperature at arbitrary elevation. These data were resampled to 2 km grids using cubic convolution and averaged to monthly time scale. Jarosch et al. (2012) report a mean bias of 0.5 °C for areas with high vertical relief, for the data set encompassing 1990 to 2008. Furthermore, a mean absolute error of no more than 2 °C for monthly averages was found when compared against station temperatures.

Statistical analyses

All GIS analysis and data processing was conducted with ESRI's ArcGIS 10. Statistical analysis and visualisation was conducted using the R statistical software package (R Development Core Team, 2008).

Results

Monthly averages of LST and two downscaled temperature products for May through August 2008, for grid cells for the six land cover groups are plotted against snow cover fractions in Figure 4-2. The land cover classes are displayed in decreasing average elevation (top to bottom), where Permanent Snow & Ice is located at the top of the elevation set. The temperature measures, displayed as a function of snow cover, increase from May to July and then decrease in August. As expected the snow fractions

in the Permanent Snow & Ice class decrease from May to July as snow melting exposes bare ground. For the low elevation classes where permanent snow and ice are not present, the maximum snow cover fraction decreases from ~50 – 70 % in May towards the July minimum. Downscaled air temperatures overlap, or are very close to, the average LST values plus or minus standard error, for the snow fractions <10 % for the Conifer land cover class (where the Environment Canada meteorological stations are situated). The two downscaled products are very similar and display an offset, where the statistically downscaled SNAP temperature product is consistently warm in comparison to the downscaled NARR product. Furthermore the NARR product is more sensitive to snow cover than the SNAP product for the Sparse Vegetation class and shows a strong negative relationship with snow cover. However, where treed canopies occur the negative relationship to snow cover for both downscaled products is much less distinct. The monthly average of MODIS fractional snow cover at the two grid cells that intersect with the Environment Canada meteorological stations at Burwash Landing and Haines Junction ranges between 0% and 0.48% for May through August. The exception to this range occurs for Burwash Landing for August where the snow cover fraction is 1.7%. The very small snow cover fractions that occur at the meteorological stations suggest that snow-free temperature trends are being interpolated to higher elevation snow covered sites in the SNAP product.

Average LST is consistently and progressively colder than SNAP and NARR temperatures for snow fractions greater than ~40%. The higher elevation land cover classes, which had high snow fractions (>90 %), displayed LSTs 5-7 °C colder for the two downscaled temperature products. The difference between downscaled NARR

temperatures and average LST is smaller than that of downscaled SNAP and closer in absolute values, indicating that downscaling of NARR in remote, high elevation, glaciated terrain is a likely a better estimate of true temperature in these locations. Inspection of the Permanent Snow & Ice and the Sparse Vegetation & Barren classes indicate that the difference between average LST and the downscaled interpolated products increases slightly from May to August. Figure 4-3 displays maximum monthly average LST in relation to SNAP and NARR monthly averages by snow fraction. Figure 4-4 shows minimum monthly average LST. Maximum monthly average LST displays a large decrease in temperature by $\sim 20^{\circ}\text{C}$ over the range of snow covers from 10 % to 100 %. At the 80 % - 100 % range of snow cover, the maximum LST has values slightly below 0°C , and tends to be similar to the downscaled temperature products. Minimum monthly average LST is uniformly colder than the downscaled products by $\sim 10^{\circ}\text{C}$ for all snow cover fractions. Maximum LST shows a much stronger negative relationship to snow cover than minimum LST.

Table 4-2 shows the average number of monthly maximum and minimum LST measurements and standard deviation in a month for each 10% category of snow cover for each point in Figure 4-2. The number of monthly maximum LST measurements is stable across all four months and varies between 2.2 to 11.8 with an average of 5.5. The number of monthly minimum LST measurements varies considerably by land cover (a proxy for elevation) and month, and ranges between 3.1 and 14.0 with an average of 8.4. For the higher elevation ground covers, in May and August, the number of minimum measurements of LST out numbers maximum by approximately 2-3 times. The numbers of maximum and minimum LST measurements is closer to equal for all summer months

in number in the Conifer land cover. The number of minimum LST measurements in June and July is approximately half of May and August.

Table 4-3 shows the comparison of the grid cells for the three monthly average temperature products with that of all sky air temperature measured at nine independent metrological stations. The stations are located on Barren, Sparsely Vegetated or Permanent Snow & Ice land covers. The SNAP and NARR downscaled temperatures are typically within ± 2 °C of the air temperature average irrespective of differences between station elevation and the intersecting grid cell average elevation. In contrast the grid cells with < 10 % snow cover displayed an average LST of 1-3 °C warmer than the other measures of temperature and grid cells with > 90 % snow cover displayed an average LST of 4-6 °C colder than the other measures of temperature.

Discussion

The downscaled temperature, station air temperature and LST all trend colder as the snow fraction increases, but where there is low snow cover (< 40 %) the LST tends to be warmer. The trend in average LST is caused by the strong decline in maximum LST, to ~ 0 °C as snow fractions get larger, coupled with the uniformly cold minimum LST values. We expected the LST averages to be within 2-3 °C of air temperature for snow free vegetated surfaces (Zaksek et al., 2009) or when using daytime temperature measurements exclusively over snow covered terrain (Hall et al., 2008). An analysis by Williamson et al. (2013) showed that near instantaneous daytime MODIS LST versus air temperature relationship from the two Environment Canada meteorological stations

located within the study area were highly correlated throughout the year, indicating that snow cover does not bias the daytime air temperature – LST relationship (night time measurements were not investigated). Thus, in the Conifer land cover, where the two Environment Canada meteorological stations are located, snow cover is inherently accounted for in both MODIS LST and downscaled air temperature, under clear skies.

Westermann et al. (2012) showed that the inclusion of minimum LST into longer term averages caused a cold bias compared to in-situ ground level thermal infrared measurements of between 1.5 and 6 K, with a mean bias of 3 K, in winter on Svalbard. Cloud cover increases the average minimum surface temperature, compared to the clear sky satellite measurement of MODIS LST, and is the reported cause of the discrepancy. This phenomenon is also seen when making aggregated eight-day averages using minimum and maximum LST gathered from the same day or from different days within the same eight-day period (Williamson et al., 2014). The results of the comparison of downscaled temperature products and LST to snow cover indicates that maximum LST and NARR temperature are the most sensitive to changing snow cover, most especially for areas where there is little treed canopy cover.

The number of measurements of maximum and minimum per month seems to exert little influence on the relationship between downscaled temperature and LST. This is confirmed by comparing the number of observations of maximum or minimum LST found in Table 4-2 to the trends in downscaled temperatures compared to maximum and minimum LST in Figures 4-3 and 4-4. If the number of observations was playing a large role in determining the discrepancy between downscaled temperature and LST, then the difference between these measures of temperature should be governed

by the number of observations. This was not observed, and our results suggest that the effect reported by Westermann et al. (2012) also operates in summer as it does in winter, but for snow fractions greater than ~40 %. The opposite relationship occurs in summer when the snow fraction is less than ~10% in a grid cell: average LST is greater than air temperature for land cover classes above treeline. This was likely caused by a clear sky bias to warm temperatures for maximum values of LST.

Two areas require further work to fully exploit the relationships found between downscaled temperature products and LST with regard to snow cover. Improved fractional snow cover algorithms for MODIS will provide an increased level of confidence in the corrections required for the temperature products, especially in densely treed land covers. Second, the relationship between maximum and minimum LST in relation to other temperature products can aid in the investigation of atmospheric and ground heat fluxes, especially in remote areas experiencing changes in snow cover such as high latitude tundra.

Conclusions

We used the four summer months of 2008 to assess the relationship between downscaled temperature and average LST caused by and changes in snow cover. We find that summer ‘clear sky’ observation for satellite measurement of infrared temperature causes a cold bias in average LST because of the interplay between minimum and maximum LST over different land cover types, when related to other average temperature products, but only when there is snow cover greater than ~ 40 %.

Average LST is 5-7 °C colder than the other measures of surface temperature for > 90 % snow covered grid cells. Conversely, a lesser amount of evidence indicates that average LST is 1-3 °C warmer for grid cells with snow cover < 10 %.

Table 4-1: Southwest Yukon validation meteorological stations, descriptions and locations.

Site	Location	Description	Station Elevation (m)	Grid Cell Elevation (m)
South Glacier (GL1)	60.82°N, 139.13°W	Permanent Snow & Ice	2280	2427
North Glacier (GL2)	60.91°N, 139.16°W	Sparse Vegetation	2319	2016
Transect Canada Creek	60.88°N, 138.97°W	Sparse Vegetation	2184	2600
Transect Duke River	60.94°N, 138.90°W	Sparse Vegetation	2214	1960
Pika Camp	61.21°N, 138.28°W	Sparse Vegetation	1635	1681
John Creek	61.20°N, 138.25°W	Sparse Vegetation	1408	1812
Ruby Range North	61.25°N, 138.19°W	Sparse Vegetation	1926	1621
Kaskawulsh	60.74°N, 139.17°W	Permanent Snow & Ice	1845	1807
Divide	60.70°N, 139.81°W	Permanent Snow & Ice	2690	2377

Land Cover	Snow Cover	May			June			July			August						
		Max Obs	Max Sd	Min Obs	Min Sd	Max Obs	Max Sd	Min Obs	Min Sd	Max Obs	Max Sd	Min Obs	Min Sd				
Permanent Snow & Ice	<10%								6.6	1.6	5.4	0.7	5.3	3.0	9.6	2.3	
	10% - 20%								4.6	2.1	6.7	1.9	5.1	3.0	10.4	4.7	
	20% - 30%								3.3	1.3	7.6	3.1	4.6	1.8	10.1	3.0	
	30% - 40%							4.8	5.2	3.7	7.7	2.8	5.0	3.7	11.1	3.5	
	40% - 50%							7.4	6.5	4.1	8.0	2.9	3.9	2.6	10.9	4.0	
	50% - 60%							5.4	2.6	5.9	2.7	6.9	3.5	3.8	2.6	12.5	3.4
	60% - 70%	4.5	3.6	12.8	3.0	3.4	2.3	5.8	2.4	3.9	2.8	8.1	3.0	3.5	2.3	11.5	3.7
	70% - 80%	4.1	2.3	12.3	2.2	3.7	2.8	6.2	2.7	3.0	2.1	8.7	4.0	3.1	1.9	12.2	3.5
	80% - 90%	4.5	2.9	13.2	2.4	3.1	1.9	6.4	2.6	3.2	2.0	7.5	3.7	3.6	2.0	11.3	3.5
>90%	8.4	3.3	11.8	2.6	5.0	2.5	6.4	2.4	3.7	1.9	7.1	3.0	5.6	2.6	9.4	3.2	
Sparse Vegetation & Barren	<10%	7.8	4.8	10.9	1.8	7.7	3.1	4.9	1.8	7.6	2.5	5.7	7.4	2.8	7.5	2.5	
	10% - 20%	6.0	4.5	11.5	2.0	6.4	3.7	5.4	2.1	5.7	3.0	7.0	6.4	3.3	10.5	3.8	
	20% - 30%	5.5	4.4	12.0	2.0	5.4	3.5	5.6	2.0	5.7	2.9	8.0	5.9	3.3	11.7	3.4	
	30% - 40%	4.2	3.4	12.0	2.0	5.0	3.1	5.8	2.2	4.2	2.4	8.9	4.8	3.0	12.3	3.9	
	40% - 50%	4.1	2.9	12.3	2.1	4.0	3.0	6.4	2.0	4.5	3.2	8.2	4.4	2.9	12.9	3.8	
	50% - 60%	4.1	2.9	12.5	2.1	4.4	3.6	6.6	2.5	3.1	1.9	8.4	3.0	3.6	2.2	11.9	3.0
	60% - 70%	4.3	2.9	12.8	2.1	4.2	2.4	6.7	2.6	3.7	3.1	8.3	3.3	5.1	3.3	13.2	3.5
	70% - 80%	4.2	2.4	12.5	2.2	3.4	2.5	7.1	2.3	2.2	1.0	8.1	5.0	4.0	5.3	11.5	3.5
	80% - 90%	4.4	2.4	12.8	2.2	2.8	1.4	7.8	3.3					3.5	1.3	14.0	1.8
>90%	6.0	3.1	12.9	2.4	3.7	1.9	7.7	2.9					4.9	2.2	6.3	1.2	
Closed to Open Grassland	<10%	8.9	3.5	10.4	1.9	7.9	2.4	4.4	1.6	7.5	2.0	5.3	1.7	6.9	1.9	5.5	2.1
	10% - 20%	6.2	3.1	11.2	2.0	6.8	2.8	5.0	1.9	6.2	0.9	4.5	1.0	6.7	2.2	5.4	1.7
	20% - 30%	5.0	2.3	11.3	1.9									5.7	1.5	4.3	1.1
	30% - 40%	5.0	2.7	12.4	1.6												
Mosaic Forest, Shrubland, Grassland	40% - 50%	5.0	2.4	12.7	2.0												
	<10%	10.0	3.4	10.4	1.9	8.4	2.7	4.4	1.7	7.8	2.0	5.1	1.7	7.5	2.2	6.3	2.1
	10% - 20%	6.1	3.2	11.1	2.4	5.0	2.7	3.8	2.0	6.0	3.0	5.4	1.8	7.6	1.4	4.8	1.2
	20% - 30%	4.7	2.9	12.1	1.7									5.4	1.2	4.6	1.3
Mixed Forest	30% - 40%	6.0	2.5	11.8	1.9												
	40% - 50%	5.0	2.6	12.3	1.7												
	50% - 60%	5.2	2.0	12.7	1.5												
	60% - 70%	3.9	2.9	11.7	1.8												
Conifer Forest	70% - 80%	4.9	1.7	13.0	1.3												
	<10%	8.0	3.3	10.0	2.1	8.3	2.9	4.6	1.7	7.6	1.9	4.9	1.6	7.1	2.2	6.3	1.9
	10% - 20%	5.1	2.5	11.4	2.2	4.7	2.1	4.1	1.6					7.4	1.5	5.2	1.1
	20% - 30%	4.8	2.6	12.0	2.2												
Conifer Forest	30% - 40%	4.8	2.1	12.6	1.9												
	40% - 50%	5.1	2.0	12.4	1.7												
	50% - 60%	3.3	1.3	11.9	1.7												
	60% - 70%	3.9	1.5	11.3	2.1												
Conifer Forest	70% - 80%	4.7	1.2	11.6	1.5												
	<10%	11.8	3.3	9.8	2.0	10.1	3.1	4.3	1.7	9.3	2.3	5.4	1.6	8.7	2.4	6.4	2.2
	10% - 20%	10.2	3.6	11.1	2.2	7.3	5.0	3.1	1.2					7.7	2.1	5.2	1.5
	20% - 30%	9.1	4.7	11.6	2.3									6.2	0.9	4.3	1.0
Conifer Forest	30% - 40%	9.5	3.5	12.7	2.2												
	40% - 50%	7.8	2.5	12.4	1.5												
50% - 60%	9.3	3.5	12.9	1.0													

Table 4-2: The average number of daily measurements of maximum and minimum 2008 LST for each month and 10 % snow cover bins, including standard deviation. This Table is presented with the same categorical breaks as Figure 4-2.

Table 4-3: The comparison of air temperature from nine meteorological stations to the intersecting NARR, SNAP and LST (average, maximum and minimum) grid cells in 2008. Included is the number of observations of minimum and maximum LST. NA refers to LST grid cell's where Average LST could not be calculated because minimum or maximum LST were not acquired.

Month	Site	Snow Cover (%)	Station Tair (°C)	NARR (°C)	SNAP (°C)	LST (°C)	LST Max (°C)	LST Max Obs	LST Min (°C)	LST Min Obs
May	South Glacier (GL1)	99.5	-3.8	-5.3	-3.6	-12.1	-8.2	2.7	-16.1	13.5
	North Glacier (GL2)	79.4	-3.5	-2.7	-3.8	NA	NA	NA	NA	NA
	Transect Canada Creek	98	-2.2	-5.3	-4.1	-13.1	-9.4	5.7	-16.9	16.2
	Transect Duke River	89.6	-3.9	-2.3	-2.8	-9.1	-3.9	6.2	-14.3	18.3
	Pika Camp	61.2	0.4	1.7	1.1	7.5	20.8	2.5	-5.8	11.7
	Kaskawulsh	99.11	-1.5	-1.4	1.0	NA	NA	NA	NA	NA
	Divide	99.5	-7.9	-5.6	-5.7	-10.3	-4.2	12.5	-16.4	15.8
June	South Glacier (GL1)	98.0	0.0	-2.4	0.2	NA	NA	NA	NA	NA
	North Glacier (GL2)	71.5	0.2	0.6	1.2	-2.6	3.3	2.5	-8.5	11.0
	Transect Canada Creek	61.8	1.0	-2.3	-0.4	-6.1	-1.2	2.0	-11.1	9.0
	Transect Duke River	66.7	0.0	1.0	1.1	1.2	7.7	3.3	-5.2	9.3
	Pika Camp	3.4	3.9	4.7	5.3	6.7	14.7	8.3	-1.3	5.8
	Kaskawulsh	95.3	2.7	1.8	3.9	-2.2	0.8	5.3	-5.1	8.5
	Divide	100	-3.7	-2.8	-1.5	-6.3	-0.9	3.5	-11.8	4.8
July	South Glacier (GL1)	41.9	1.2	2.8	3.0	NA	NA	NA	NA	NA
	North Glacier (GL2)	72.4	1.8	0.1	3.2	NA	NA	NA	NA	NA
	Transect Canada Creek	88.1	2.7	0.2	3.4	NA	NA	NA	NA	NA
	Transect Duke River	20.8	1.9	3.2	4.1	1.0	11.4	5.0	-9.5	9.8
	Pika Camp	0.0	5.6	6.3	8.2	9.0	17.8	7.8	0.2	3.5
	Kaskawulsh	86.0	4.4	4.0	6.7	-1.0	6.4	3.3	-8.5	4.8
	Divide	99.9	-2.1	-0.1	1.9	-6.0	-1.3	3.3	-10.7	4.8
August	South Glacier (GL1)	70.2	0.9	2.4	-0.3	-5.5	-2.6	2.7	-8.5	12.5
	North Glacier (GL2)	32.1	1.1	3.5	2.2	2.2	13.4	4.2	-8.9	15.0
	Transect Canada Creek	64.2	2.1	2.0	-0.4	-6.6	-2.7	2.2	-10.5	16.7
	Transect Duke River	10.5	1.4	3.5	2.5	3.5	12.1	4.2	-5.1	11.7
	Pika Camp	0.0	4.6	7.3	5.5	7.3	15.2	10.5	-0.6	4.2
	John Creek	0.0	5.5	7.0	4.6	6.8	16.1	8.5	-2.6	6.0
	Ruby Range North	0.0	2.9	7.3	5.1	6.6	15.4	9.5	-2.2	5.5
	Kaskawulsh	82.1	3.7	7.8	3.6	-3.1	-0.3	5.0	-5.8	9.2
	Divide	99.4	-2.3	1.2	-0.3	-6.2	-3.8	8.5	-8.7	10.8

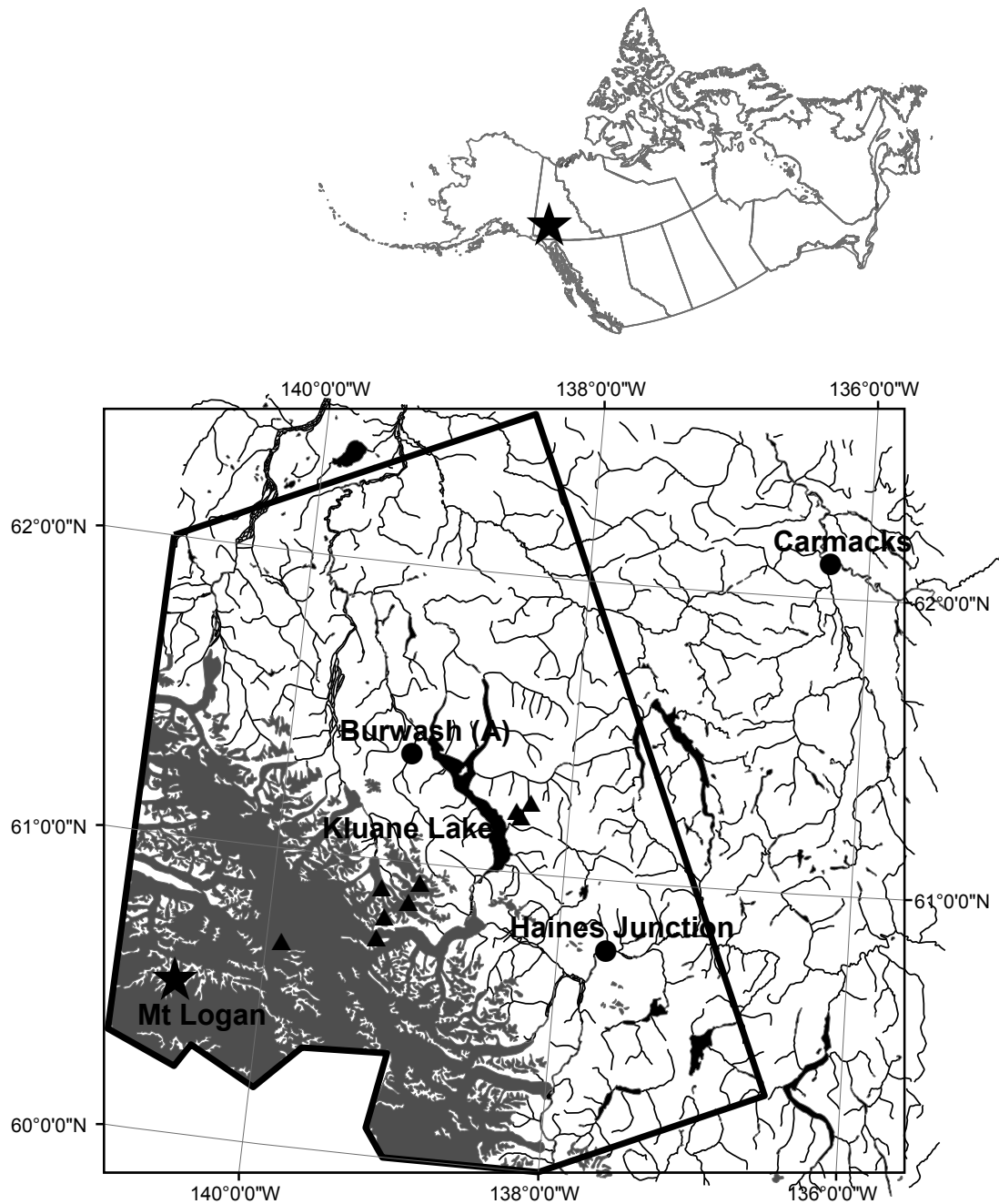


Figure 4-1: The southwest Yukon study area bounded by the thick black line. The grey portion is the glaciated region of Kluane National Park. The elevational gradient extends from the summit of Mt Logan (5,959 m) to Kluane Lake (780 m), and some lower elevation drainages. Two Environment Canada meteorological monitoring stations are located within the study area at Haines Junction (655 m) and Burwash Landing (795 m). Nine additional meteorological monitoring stations are found on Permanent Snow & Ice and Sparse Vegetation & Barren land covers (solid triangles).

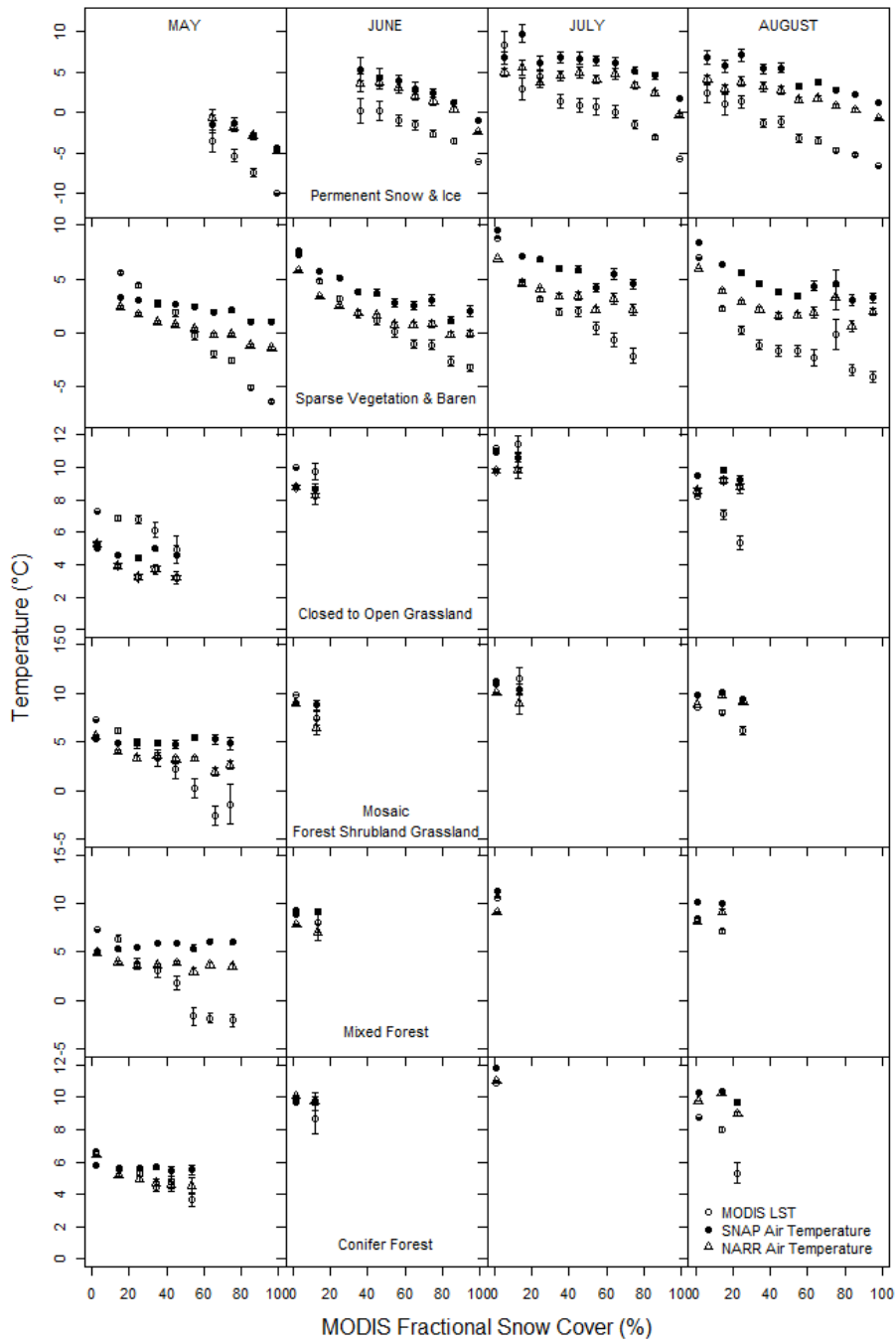


Figure 4-2: Downscaled interpolated air temperature (SNAP) and downscaled NARR surface temperature plotted with MODIS Average Land Surface Temperature (LST) separated by snow fractions in 10% bins, for May through August 2008 monthly means. Six aggregated land cover classes decrease in elevation from a) Permanent Snow and Ice to f) Conifer forest. Error bars indicate standard error.

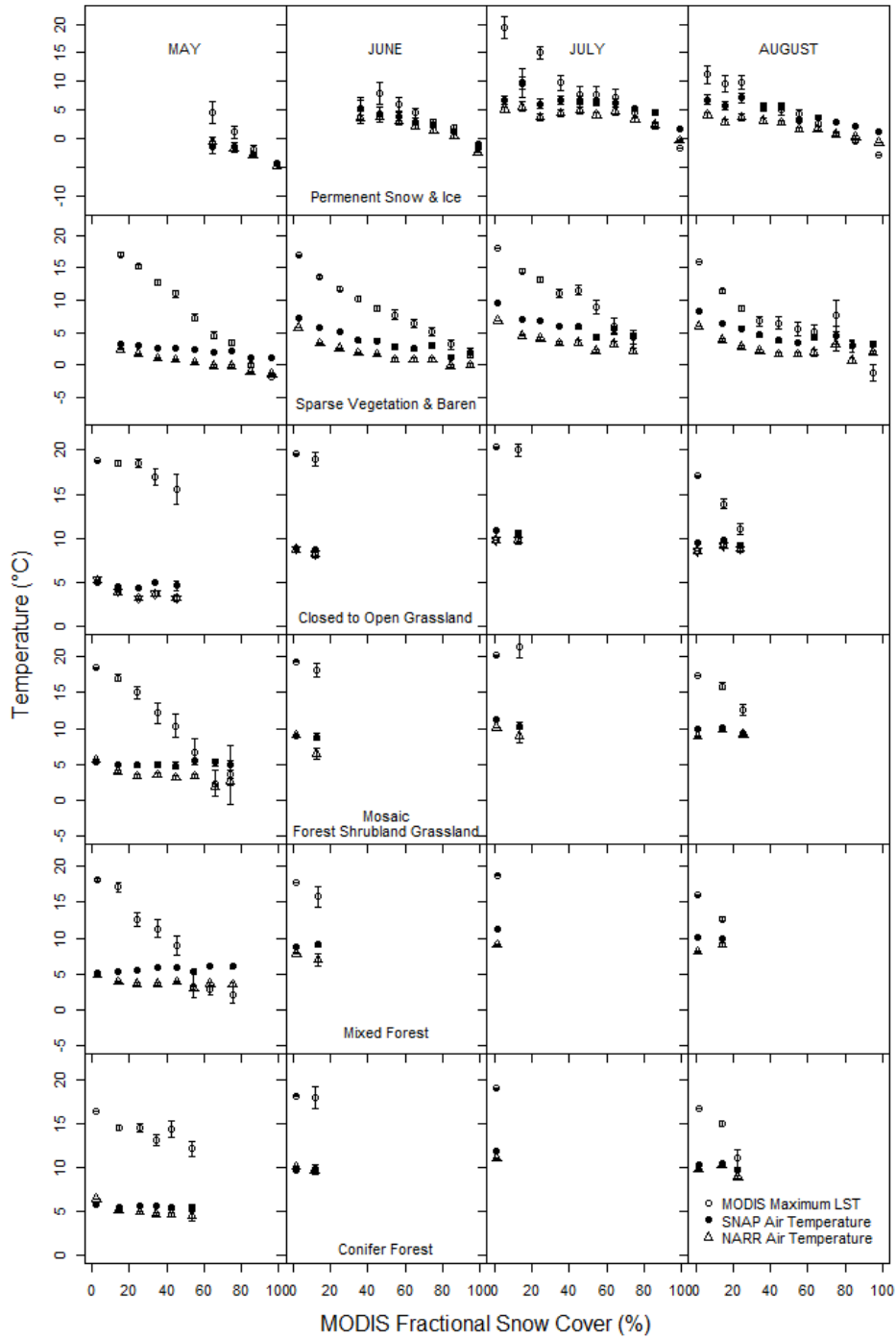


Figure 4-3: Downscaled interpolated air temperature (SNAP) and downscaled NARR surface temperature plotted with MODIS Maximum Land Surface Temperature (LST) separated by snow fractions in 10% bins, for May through August 2008 monthly means. Six aggregated land cover classes decrease in elevation from a) Permanent Snow and Ice to f) Conifer forest. Error bars indicate standard error.

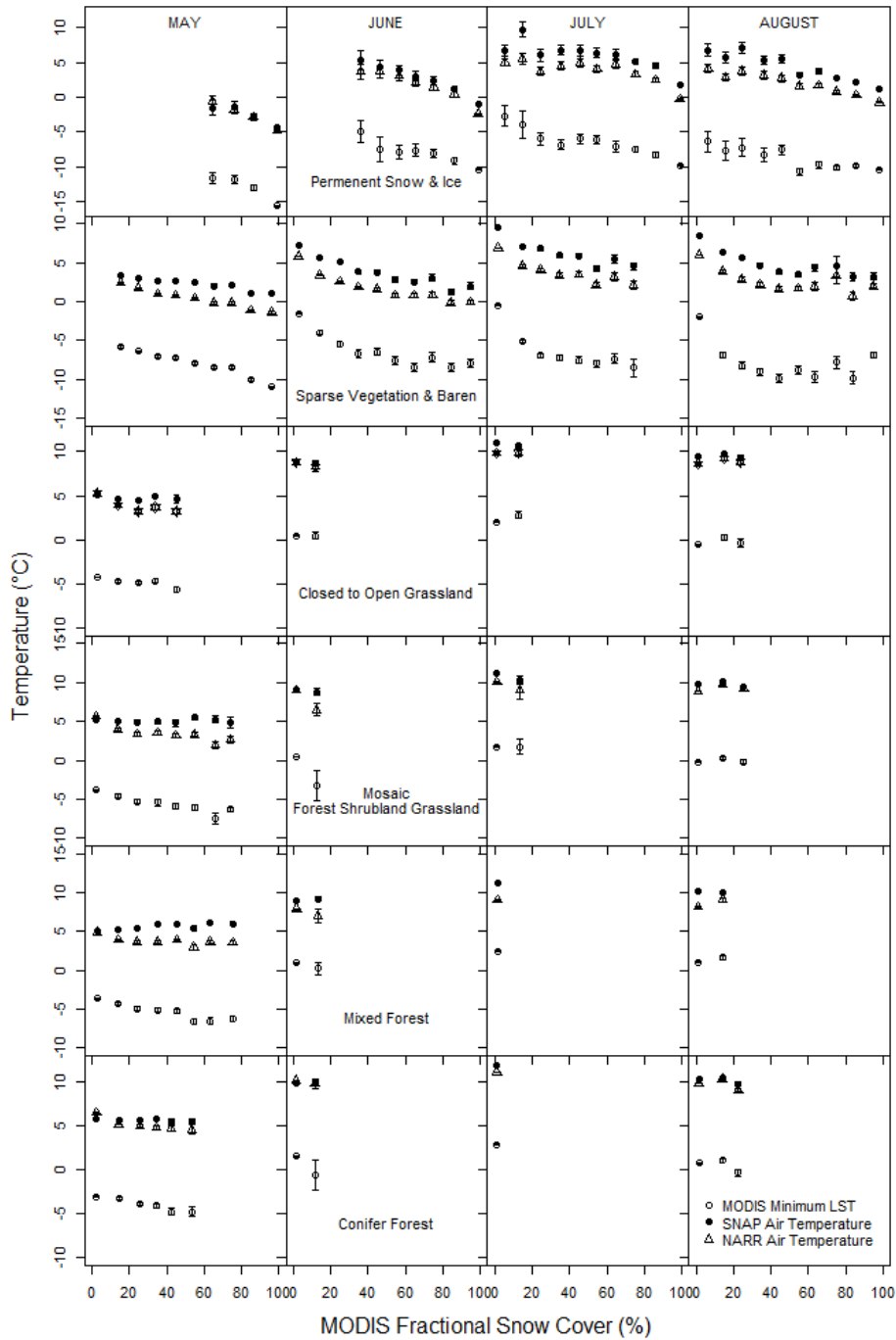


Figure 4-4: Downscaled interpolated air temperature (SNAP) and downscaled NARR surface temperature plotted with MODIS Minimum Land Surface Temperature (LST) separated by snow fractions in 10% bins, for May through August 2008 monthly means. Six aggregated land cover classes decrease in elevation from a) Permanent Snow and Ice to f) Conifer forest. Error bars indicate standard error.

References

- Arctic Climate Impact Assessment (ACIA) Report. (2005). Impacts of a warming Arctic. UK: Cambridge University Press 146 p.
- Ackerman, S.A., Strabala, K.I., Menzel, W.P., Frey, R.A., Moeller, C.C., & Gumley, L.E. (1998). Discriminating clear sky from clouds with MODIS. *Journal of Geophysical Research*, **103**, 32141- 32157.
- Benali, A., Carvalho, A.C., Nunes, J.P., Carvalhais, N., & Santos, A. (2012). Estimating air surface temperature in Portugal using MODIS LST data. *Remote Sensing of Environment*, **124**, 108-121.
- Comiso, J.C. (2003). Warming trends in the Arctic from clear sky satellite observations. *Journal of Climate*, **16**, 3498-3510.
- Daly, C., Neilson, R. P., & Phillips, D. L. (1994). A statistical-topographical model for mapping climatological precipitation over mountainous terrain. *Journal of Applied Meteorology*, **33**, 140-158.
- Fleming, M. D., Chapin, F. S., Cramer, W., Huffords, G. L., & Serreze, M. C. (2000). Geographic patterns and dynamics of Alaskan climate interpolated from a sparse station record. *Global Change Biology*, **6**, 49-58.
- Hall, D. K., Box, J. E., Casey, K. A., Hook, S. J., Shuman, C. A., & Steffen, K. (2008). Comparison of satellite-derived and in-situ observations of ice and snow surface temperatures over Greenland. *Remote Sensing of Environment*, **112**, 3739-3749.
- Hall, D. K., & Riggs, G. A. (2007). Accuracy assessment of the MODIS snow products.

Hydrological Processes, **21**, 1534-1547.

Hall, D. K., Riggs, G. A., Salomonson, V. V., DiGirolamo, N. E., & Bayd, K. J.

(2002). MODIS snow-cover products. *Remote Sensing of Environment*, **83**, 181-194.

Intergovernmental Panel on Climate Change (IPCC) (2007). Summary for policy makers. In Solomon S and 7 others (Eds.) *Climate change 2007: the physical science basis. Contribution of Working Group I to the Fourth Assessment Report of the Intergovernmental Panel on Climate Change*. Cambridge, etc., Cambridge University Press.

Jarosch, A. H., Anslow, F. S., & Clarke, G. K. C. (2012). High-resolution precipitation and temperature downscaling for glacier models. *Climate Dynamics*, **38**, doi: 10.1007/s00382-010-0949-1.

Jin, M., & Dickinson, R. E. (1999). Interpolation of surface radiative temperature measured from polar orbiting satellites to a diurnal cycle: 1. Without clouds. *Journal of Geophysical Research – Atmosphere*, **104**, doi:10.1029/1998JD200005.

Jin, M., & Dickinson, R. E. (2010). Land surface skin temperature climatology: benefitting from the strengths of satellite observations, *Environmental Research Letters*, **5**, doi:10.1088/1748-9326/4/044004.

Mesinger, F., DiMego, G., Kalnay, E., Mitchell, K., Shafran, P.C., Ebisuzaki, W., Jović, D., Woollen, J., Rogers, E., Berery, E.H., Ek, M.B., Fan, Y., Grumine, R., Higgins, W., Li, H., Lin, Y., Manikin, G., Parrish, D., & Shi, W. (2006). North American Regional Reanalysis. *Bulletin of the American Meteorological Society*, **87**, 343-360.

- Painter, T. H., Rittger, K., McKenzie, C., Slaughter, P., Davis, R.E., & Dozier, J. (2009). Retrieval of subpixel snow covered area, grain size, and albedo from MODIS. *Remote Sensing of Environment*, **113**, 868-879.
- Prudhomme, C., Reynard, N., & Crooks, S. (2002). Downscaling of global climate models for flood frequency analysis: Where are we now? *Hydrological Processes*, **16**, 1137–1150.
- Pu, Z., Xu, L., & Salomonson, V. (2007). MODIS/Terra observed seasonal variations of snow cover over the Tibetan Plateau. *Geophysical Research Letters*, **34**, L06706, doi:10.1029/2007GL029262.
- R Development Core Team (2008). R: A language and environment for statistical computing. R foundation for Statistical Computing, Vienna, Austria. ISBN 3-900051-070-0, URL <http://www.R-project.org>.
- Raleigh, M. S., Rittger, K., Moore, C. E., Henn, B., Lutz, J. A., & Lundquist, J. D. (2013). Ground-based testing of MODIS fractional snow cover in subalpine meadows and forest of the Sierra Nevada. *Remote Sensing of Environment*, **128**, 44-57.
- Raynolds, M. K., Comiso, J. C., Walker, D. A., & Verbyla, D. (2008). Relationship between satellite-derived land surface temperatures, Arctic vegetation types, and NDVI. *Remote Sensing of Environment*, **112**, 1884-1894.
- Robeson, S. M. (1995). Resampling of network-induced variability in estimates of terrestrial air temperature change. *Climatic Change*, **29**, 213–229.
- Royer, A., & Poirier, S. (2010). Surface temperature spatial and temporal variations in North America from homogenized satellite SMMR-SSM/I microwave measurements

- and reanalysis for 1979-2008. *Journal of Geophysical Research*, **115**, D08110, doi:10.1029/2009JD012760.
- Salomonson, V. V., & Appel, I. (2004). Estimating fractional snow cover from MODIS using the normalised difference snow index. *Remote Sensing of Environment*, **89**, 351-360.
- Sellers, W. D. (1965). *Physical Climatology*. Univ. of Chicago Press, Chicago, IL. 272p.
- Serreze, M., Barrett, A., Stroeve, J., Kindig, D., & Holland, M. (2009). The emergence of surface-based Arctic amplification. *Cryosphere*, **3**, 11-19.
- Snow, Water, Ice, Permafrost in the Arctic (SWIPA) (2011) Accessed 22 April 2013, <http://amap.no/swipa>
- Snyder, W. C., Wan, Z., Zhang, Y., & Feng, Y. Z. (1998). Classification-based emissivity for land surface temperature measurement from space. *International Journal of Remote Sensing*, **19**, 2753-2774.
- Vincent, L. A., & Mekis, E. (2006). Changes in daily and extreme temperature and precipitation indices for Canada over the twentieth century. *Atmosphere-Ocean*, **44**, 177-193.
- Wan, Z., Zhang, Y., Zhang, Q., & Li, Z. (2002). Validation of the land-surface temperature product retrieved from Terra Moderate Resolution Imaging Spectroradiometer data. *Remote Sensing of Environment*, **83**, 163-180.
- Wan, Z. (2008). New refinements and validation of MODIS land-surface temperature/emissivity products. *Remote Sensing of Environment*, **112**, 59-74.

- Wang, W., Liang, S., & Meyers, T. (2008). Validating MODIS land surface temperature products using long-term nighttime ground measurements. *Remote Sensing of Environment*, **112**, 623-635.
- Westermann, S., Langer, M., & Boike, J. (2012). Systematic bias of average winter-time land surface temperatures inferred from MODIS at a site on Svalbard, Norway. *Remote Sensing of Environment*, **118**, 162-167.
- Williamson, S. N., Hik, D. S., Gamon, J. A., Kavanaugh, J. L., & Koh, S. (2013). Evaluating the quality of clear-sky MODIS Terra daytime Land Surface Temperatures (LST) using ground based meteorology station observations. *Journal of Climate*, **26**, 1551-1560.
- Williamson, S. N., Hik, D. S., Gamon, J. A., Kavanaugh, J. L., & Flowers, G. E. (2014). Estimating temperature fields from MODIS land surface temperature and air temperature observations in a sub-Arctic environment. *Remote Sensing*, **6**, 946-963.
- Zaksek, K., & Schroedter-Homscheidt, M. (2009). Parameterization of air temperature in high temporal and spatial resolution from a combination of SEVIRI and MODIS instruments. *ISPRS Journal of Photogrammetry and Remote Sensing*, **4**, 414-421.

CHAPTER FIVE

Phenology and species determine growing season albedo increase at the altitudinal limit of shrub growth in the sub-Arctic

Introduction

Warming in the Arctic has been linked to spring snow cover reduction which has extended snow-free periods in the southwest Yukon by ~10 days/decade in spring and ~2 days/decade in autumn between 1967 and 2008 (Zeng et al., 2011; Brown et al., 2010) and also with recent shrub expansion (Sturm et al., 2001; Tape et al., 2006; Frost & Epstein, 2014; Tape et al., 2012). Increased shrub growth and growing season length have been predicted to increase sensible heating by reducing albedo (Chapin et al., 2005), triggering a radiative feedback to climate that will promote further atmospheric warming (Pearson et al., 2013). However, differences between shrub species, stature and phenology might also affect this albedo feedback and consequently alter simple predictions about future feedback processes (Oke, 1987), especially in a warmer (SWIPA, 2013) and wetter (Cook et al., 2014) Arctic. Similarly, warming alpine tundra is also leading to increased shrub growth (Hallinger et al., 2010), and it is generally accepted that shrub expansion will reduce albedo in both winter and summer (Sturm et al., 2005). However, field measurements of tundra summer energy budgets and albedo are typically conducted over short periods (1-14 days (see review article by Eugster et al., 2000) that coincide with growing season peak, and lack sampling consistency between studies, especially when spatial averaging is applied. These sampling differences lead to uncertainty in albedo assessment, and the considerable range in the

reported albedo values for most Arctic land cover (e.g., Eugster et al., 2000) preclude accurate predictions of how changing feedback processes will affect tundra energy budgets.

However, several studies which measured albedo for the whole of the growing season show an increase in albedo after snow melt, suggesting growing-season vegetation albedo is more dynamic than fixed values allow. In snow-free, sparsely vegetated tundra, albedo increases with decreasing soil moisture as the growing season progresses (Harding & Lloyd, 1998). A study of mixed willow-birch in the sub-Arctic shows that albedo displays a growing season increase from 0.11 (prior to leaf emergence) to 0.16 after leaves have completely opened indicating that the canopy has progressively become more reflective of incoming shortwave radiation (Blanken & Rouse, 1994). The increase in albedo is strongly and positively related to Leaf Area Index (LAI) for both deciduous trees and sedges (Lafleur et al., 1987).

Shrub species identity, height, and phenological changes in canopy structure affect albedo, so should all be considered in detailed analyses of vegetation feedbacks. Short deciduous shrubs (<0.5m) of the genera *Betula* and *Salix* are largely responsible for shrub encroachment into tundra (Tape et al., 2006; Euskirchen et al., 2009). While both genera are predicted to increase in cover under warming scenarios, *Betula spp.* are likely to be more successful than *Salix spp.* in a warmer Arctic (Euskirchen et al., 2009). Canopy structure also influences albedo with taller vegetation typically having lower albedo than shorter vegetation because taller vegetation is typically more effective at radiation trapping (Oke, 1987). Comparisons of species with contrasting heights confirm that low shrubs have a consistently higher albedo than tall shrubs measured

along a 50 m transect in Alaska when measured early in the growing season after snowmelt (Sturm et al., 2005). This decline in albedo with canopy height has also been observed along a 5 km transect extending from tundra, low shrub, tall shrub, woodland to forest (Thompson et al., 2004). Also, phenological changes along the growing season can influence albedo values. When the albedo values for snow-off pre-leaf low and tall shrub categories from Sturm et al. (2005) are compared to those of Thompson et al. (2005) for the same categories at peak growing season, the albedo has increased by 0.03 – 0.04 between pre-leaf and peak growing season.

To better understand albedo dynamics associated with common Arctic land cover, we measured albedo throughout the growing season at six sites identified *a priori* as being representative of the major alpine tundra land cover types in the southwest Yukon (Figure 5-1). The vegetation along this transect was typical of plant cover at different stages of succession and shrub encroachment (Danby et al., 2011), and our precisely repeated measurements allowed us to account for differences associated with shrub species, canopy structure and height without the confounding effects of spatial averaging across multiple vegetation types. Our specific aim was to determine the growing season albedo trends of tundra landscape cover characteristic of different stages of succession, measured near the upper elevational limit of shrub growth. Making measurements at the upper elevational limit indicates the shrubs being measured are those occupying the successional limit and likely represent the characteristics of the shrubs that will expand into new areas in the future. According to the generally accepted view, we expected that patches dominated by shrubs would have lower albedo values (e.g., Pearson et al., 2013) throughout the growing season than the surrounding

short-statured vegetation or bare ground, but, as discussed below, the actual findings were more nuanced and complex. To put our results into a broader context, we also calculate how the observed albedo changes affect energy budgets of the tundra.

Methods

Field Albedo Measurements

Albedo was measured throughout the 2012 and 2013 growing seasons at six locations along a 200 m north-south transect that paralleled the drainage axis in an alpine valley of the southwest Yukon (61.2° N; 138.3° W). The southern end of the transect was at the highest elevation (1640 m) and descended slightly to the north end of the transect (1623 m). The sites along the transect represent the major vegetation types of the alpine tundra (dry and moist tundra; no wet acidic tundra occurs at this location and no standing water is observed near the plots), and a gradient of shrub cover by *Salix pulchra* (Figure 5-1, sites A-C) and *Betula glandulosa* (Figure 5-1, site E). Plant community composition was assessed using the point intercept method (100 contacts every 0.05 m in a 0.50 m point quadrat), and each site was characterized by a single dominant species (Table 5-1). As *S. pulchra* is the dominant patch-forming shrub in the study area, a more detailed gradient of cover for this species was also included in our study design. Only low statured forms of *B. glandulosa* are found in the study area.

An albedometer (upward and a downward facing CMP11 pyranometers, CMA11, Kipp & Zonen, Delft, The Netherlands) was mounted at fixed positions over the patches of tundra being monitored. This albedometer is sensitive to short wave

radiation between 285 to 2800 nm and is the highest precision class instrument manufactured by Kipp & Zonen. The maximum temperature response of the CMA11 is < 1% for the temperature range found in the study area (-10 °C to 40 °C) and the maximum spectral selectivity is <3% between 350 and 1500 nm. The albedometer was positioned 1 m above each canopy type to minimize possible contamination from surrounding vegetation (Figure 5-1b) and was alternated among the six sites between June 28 and August 15, 2012. Sites were measured 5-6 times over the growing season at approximately weekly intervals, recording at least one diurnal cycle of one-minute averages. The observations used to compare albedo across sites were limited to one hour before and after solar noon, when the sun was at its highest elevation and albedo was at, or close to, its daily minimum (Ohmura, 1981). If compromised by obstruction of the sensor (e.g., by snow, rain or fog), data were removed from the analysis; these conditions were identified using time series of incoming solar radiation from the upper channel of the albedometer, observations from a nearby meteorological station (Campbell Scientific, Edmonton, AB, Canada), and daily field observations of weather conditions. Talus patches are common throughout the valley (~20% of the surface), and albedo of a talus reference site was measured on August 13, 2012; a different talus reference site was measured on July 15, 2013.

Sites were resampled, under clear sky conditions within two hours of solar noon, on July 15 and July 29, 2013, using one-minute intervals for 10 minutes at each site. The 2013 sampling methodology was changed from that of 2012 in order to collect albedo values for all of the sites on the same day under direct sunlight. Analysis of the variance of 2012 albedo values indicated that under direct sunlight 10 min was sufficient

to collect a representative albedo measurement. Finally, four additional albedo measurements of *B. glandulosa* were made on July 14 and 15, 2013: three measurements were conducted 200 m north of the north end of the transect (lowest elevation – 1615 m) and one measurement was made at the south end (highest transect elevation – 1640 m). One moss site and an additional talus site both in the middle of the transect were measured on July 15, 2013.

Field Spectra Measurements

On August 15, 2012 the six transect sites were scanned five times each, over one minute, with a full-range radiometrically calibrated spectroradiometer (PSR-3500, Spectral Evolution, Lawrence, MA, USA) using a 25° field of view foreoptic, 1 m above ground. These scans provided an independent method for calculating albedo and allowed for analysis of fine scale spectral features that provide information on the influence of canopy properties, such as Leaf Area Index (LAI), on albedo. Because the PSR-3500 is a single-channel instrument that requires clear-sky conditions for high quality scans, spectra were only collected on this date. To further normalise for variation in lighting conditions and calculate spectral reflectance, a scan of a 99% reflectance white standard (Spectralon, LabSphere, North Sutton, NH, USA) preceded radiance scans. The spectral range of the PSR-3500 is 350 – 2500 nm, with spectral resolution of 3.5 nm over the 350-1000 nm range; 10 nm at 1500 nm; and 7 nm at 2100 nm. For comparison with albedometer readings, albedo was also calculated from spectral reflectance by using a simple average of the reflectance values for all

bandwidths between 350 nm and 2100 nm, disregarding the atmospheric absorption bands (350-399 nm, 1361-1409 nm, 1801-1959 nm, 2401-2500 nm) that lacked sufficient energy to provide good signal. The correlation of the PSR-3500 albedo measurements and the CMA-11 albedo values collected between August 8 – 13, 2012 was $R^2=0.97$ using 5 of the 6 sites. For this correlation, the dry tundra site was omitted because the spatial heterogeneity of *Dryas* and lichen ground cover resulted in different sampling footprints for the albedometer and the spectroradiometer. The high correlation between these independent measures of albedo indicated that the cosine field of view of CMA-11 provided a good representation of a discrete patch of tundra for the five sites when measured at 1 m above the ground.

Field Observation of Phenological Change

An oblique photo of each plot was taken during each measurement period in 2012 to record vegetation phenology. At the beginning of the summer measurement period, recently emerged shrub leaves, stems and branches were visible; green graminoids were just visible above the previous year's senesced material. By the end of the measurement period, deciduous leaves obscured more of the understory but showed no visible signs of senescence; *Carex spp.* displayed yellowing by August 10, 2012. Dry tundra appeared unchanged in composition and phenology through the duration of the experiment.

MODIS Albedo

Eight-day composites of MODIS MCD43A3 were downloaded from NASA's Earth Observing System Data and Information System at <http://reverb.echo.nasa.gov>, from January 1, 2012 to August 13, 2013. MODIS 8 day white sky and black sky albedo (MCD43A3) were acquired from the EOSDIS (NASA's Earth Observing System Data Information System). White-sky albedo is the bihemispherical reflectance in isotropic illumination conditions, which therefore has the angular dependency eliminated. Black-sky albedo is the directional hemispherical reflectance for local solar noon. Broadband MODIS albedo was used in this study: visible (300–700 nm); near infrared (700–5000 nm); and short wave (300–5000 nm). The MODIS albedo data were resampled using the nearest neighbour algorithm to 500 m grid cells in the NAD83 datum. White sky and black sky albedo values in the visible, near infrared and short wave were extracted for the grid cell in which both the meteorological monitoring station and the summer albedo transect were situated. Due to extensive cloud cover for most of the early growing season, MODIS albedo values were not available at that time, thus the early growing season albedo dynamics could not be viewed directly from MODIS imagery.

Solar Radiation Energy Budget Calculations

To further evaluate the relevance of seasonal albedo changes in a broader context, we calculated overall surface energy balance at our site and estimated the influence of an increase in albedo over a longer snow-free growing season (depicted in

Figure 5-2). These calculations were made using average albedo values of the dominant land cover types at our field site and average albedo values for snow covered periods extracted for the study site from the MODIS satellite sensor, but considered the effect of temporally dynamic albedo due to changing snowmelt and vegetation growth.

For this analysis, we calculated incoming solar radiation (W/m^2) at our site for conditions (i) with no clouds, and (ii) with 70% cloud cover (typical at our site), using the three models (solrad version 1.2) available from Washington State Department of Ecology (<http://www.ecy.wa.gov/programs/eap/models.html>). Values of incoming solar radiation were compared with instrumental measurements (CM6b pyranometer, Kipp and Zonen, Delft, The Netherlands) recorded at the meteorological station located at our study site for the period between June 21 and December 30, 2012 (Figure 5-3). The scatter of the instrumental data was related to daily changes in cloud cover and consistent with our decision to use 70% cloud cover as a mean value for the entire season in these example calculations. Cloud cover was estimated as the ratio of measured solar radiation to 0% cloud covered modelled radiation [using solrad version 1.2]. The daily average energy flux was then calculated as the average of the three global models (Bird and Hulstrom, 1991; Bras, 1990; Ryan and Stolzenbach, 1972) using a 70% cloud cover parameter and default settings, and converted to absorbed energy using the conversion $1\text{MJ}/\text{m}^2 \cdot \text{day} = 11.574 \text{ W}/\text{m}^2$. Total shortwave surface energy absorption (MJ/m^2) was calculated as the albedo change multiplied by the daily average solar flux (W/m^2), summed over the number of days over which the changes took place. The additional energy absorbed due to a reduction in snow cover was calculated as the difference between snow albedo derived from MODIS MCD43A3

product (0.58 – Spring 2012 and 0.50 – Fall 2012) and average albedo of snow-free ground (0.14), multiplied by the daily average solar flux. This spring albedo difference was 0.44 and the fall albedo difference was 0.36, which were used to estimate the albedo change related to snow cover changes. These daily values were summed over the number of days of change in snow cover during the past decade: the reduction in snow cover for spring was estimated to be 11 days (June 2-12 – A in Figure 5-2) and the delay in onset of permanent snow cover in the fall was 2 days (November 7-8 – B in Figure 5-2).

The decrease in heating caused by the growing season albedo increase for the area-averaged albedo for the study site was calculated as the linear increase in albedo from June 13 to the maximum albedo at July 28 and then the subsequent linear albedo reduction to November 6, which produced an average albedo increase of 0.02 for the growing season. The conversion of radiant flux to surface energy was calculated as outlined for snow cover change, and was the cumulative sum of absorbed energy between June 13 and November 6.

Statistical Analyses

To assess overall differences in the seasonal patterns of average albedo we used generalized additive mixed models (Zuur et al., 2009; Wood, 2006), including an interaction term between date (Julian day) and site. Site was included as a random factor to account for the nested structure of the data. The adequacy of models was checked by comparing models with and without the interaction term using a Log-

likelihood Ratio Test (LRT; Zuur et al., 2009). All GAMM analyses were conducted in R 2.14.0 with the *mgcv* (Wood, 2006) package.

Results

Albedo patterns for the six land cover types were species-dependent but most species showed increasing albedo during the 2012 summer growing season (Figure 5-1a), and the timing of maximum and minimum albedo was different for each land cover type. A significant interaction between 2012 Julian day and vegetation type (LRT = 6554.96, $p < 0.001$) indicates different albedo trajectories for the six sites over the season. Sites with a deciduous shrub canopy component became more reflective as the growing season progressed (sparse, mid and dense canopy *Salix* (A-C) and dense canopy *Betula* (E)), whereas graminoid-dominated (D) and dry tundra (F) sites lacking shrub canopies, had relatively flat albedo trajectories. In 2012, shrub albedo values ranged from a high of 0.21 for mid-summer *B. glandulosa* to a low of 0.12 for early season *S. pulchra*. The 2013 albedo values (Table 5-1) followed the 2012 trend, but exhibited higher albedo values, as expected for measurements made under direct sunlight (Ohmura, 1981).

Several additional albedo measurements of *B. glandulosa* shrubs were made on July 14 and 15, 2012, with the aim of placing the albedo values measured for *Betula* on the transect into context. The average albedo for the three northern low elevation plots was 0.161 ± 0.013 . The average canopy height was 0.20 ± 0.10 m. The additional *B. glandulosa* plot at the southern elevational limit had an albedo of 0.20 ± 0.01 and had a canopy height of 0.24 m. The additional sites were uniform in appearance and in the

case of the shrubs were fully closed canopies. The albedo for moss that was collected in the middle of the transect was 0.126 ± 0.006 . An additional talus patch was also measured and had an albedo of 0.087 ± 0.001 , and represented a typical value for a region devoid of vegetation. The additional sites were collected under direct sunlight near solar noon indicating the albedo values should be approaching the minimum diurnal values. The 2013 transect resampling confirm the 2012 increase in growing season albedo for canopy forming landscape units. Further, the 2013 average albedo is larger than 2012 because only midsummer values were used in its calculation.

The average of the three models for incoming solar flux was 141.17 ± 80.39 W/m² (one standard deviation) for the period from June 21 to November 8, 2012 (the period for which field measurements of incoming solar radiation were available and albedo was less than maximum winter values). This model average value is close to the average incoming solar radiation measured at this station, 143.76 ± 89.51 W/m², over the same period, which confirms our choice to use the 70% cloud cover scenario. For comparison, the average of the three models for the 0% cloud cover parameterisation over the same period was 178.96 ± 102.53 W/m².

The effects of albedo dynamics on the overall surface energy balance are depicted in Figure 5-2. Our results indicate that a decrease in spring snow cover of 11 days will contribute an additional 103.9 MJ/m² of surface heating, while the delay in snow cover of 2 days in the fall will contribute 0.95 MJ/m². In contrast, our field measurements indicate that an average increase in summer albedo of 0.02 (0.14 to 0.16) due to vegetation growth counteracts heating associated with the reduction in snow cover by 37.3 MJ/m² (Figure 5-2).

Discussion

Albedo values of *Salix* stands were lower than shrub-free vegetated sites and albedo decreased as shrub cover increased (sparse to dense *Salix* canopy A-C) which fits with theory (Oke, 1987) and previously reported results (e.g., Thompson et al., 2004). However, mean albedo was highest for the closed-canopy *B. glandulosa* and dry tundra (sites E & F); and these plots had summer-averaged albedo values similar to vegetated sites lacking shrubs (*Carex*- and *Dryas*/lichen-covered sites, Table 5-1). The albedo values reported here for short-statured *B. glandulosa* are bracketed by both higher (Blok et al., 2011) and lower (Beringer et al., 2005) values reported for elsewhere in the Arctic, but it is difficult to determine the cause of the disparity because the physical determination of albedo and the spatial sampling regimes employed by all of these studies are different. However, the additional scans of *Betula* in the present study suggest that its albedo is not entirely related to stature and that the growth form adopted at the elevational limit has canopy properties that increase albedo compared to *Betula* found at lower elevation.

For all shrub sites observed here, minimum albedo occurred early in the growing season, immediately following snowmelt (Figure 5-1a), and then continued to increase over much of the summer. ‘Minimum’ albedo values are usually measured at or around point C in figure 5-2, which indicates that the snow off period for albedo is over-estimated if this is the only measure of albedo used. Our early season measurements of *B. glandulosa* and *S. pulchra* are similar to the end of snowmelt albedo for two similar vegetation classes measured in Alaska (Sturm et al., 2005): tundra dominated by 20 cm

high *B. nana*, and tall shrub dominated by 110 cm high *S. pulchra* and *B. glandulosa*. Growing season albedo for our shrub sites, particularly the full canopy site (Figure 5-1a and 5-2), shows clear increases during the growing season. In particular, shrubs with full canopy cover became more reflective than those with partial canopies as the growing season progressed, as indicated by the steep albedo increases early in the season for dense canopy *S. pulchra* and *B. glandulosa* (sites C and E respectively - Figure 5-1a). Lastly, the *S. pulchra* plot with the smallest canopy cover (48%) and the largest moss cover (77%; site A) had the highest albedo value for the three *Salix* plots. Although sites that had a higher dominance of moss tend to have a lower albedo values of all vegetated sites studied (indicated by the measurement of the moss site), a high coverage of graminoids at this site (Table 5-1) creates a highly reflective canopy, mitigating the effect that moss has on the plot's albedo. The vegetation albedo values are much larger than the reference albedo of bare talus, which ranged between 0.087 and 0.102 (our study), and 0.11 for Barren Tundra as measured by Blok et al. (2011), indicating that, relative to bare mineral surface, shrub expansion can actually *increase* albedo.

Daily cloud cover for the growing season of 2012 did not show a significant change (increase or decrease) over the study period, which indicates that cloud cover increase, and the resulting increase in diffuse solar radiation, was not responsible for the increasing growing season trend in albedo. The mechanism of this seasonal increase in albedo can be revealed by examining 2012 reflectance spectra; as leaves expand and the shrub canopy surface becomes increasingly impenetrable by solar radiation towards mid-summer, the increase in optical scattering increases the overall albedo (Figure 5-1),

particularly in the near-infrared (NIR) portion of the electromagnetic spectrum. This increase in NIR reflectance (Figure 5-1c), particularly in the shrub plots, illustrates the effect of canopy structure on albedo caused by increased leaf area index (Asner, 1998; Lafleur et al., 1987). Troughs at ~1000 nm and ~1200 nm are indicative of water absorption, with deeper troughs indicating higher LAI (Zheng & Moskal, 2009), as a result of larger amount of water stored within the canopy leaves for larger canopies (Sims and Gamon, 2003). In general, we observed an increase in LAI and NIR reflectance as shrub canopy cover increased. LAI estimated from reflectance spectra of *B. glandulosa* appears higher than for *S. pulchra*. Short-statured deciduous shrubs with dense canopy cover exhibited increasing albedo through the growing season, which is the general conclusion of Blanken & Rouse (1994) for a willow and birch stand near Churchill, Manitoba. Moreover, the tundra vegetation plots that had dense shrub canopies displayed the maximum increase in albedo of all plots monitored throughout the growing season in our study. Further, Weller and Holmgren (1974) found a similar increase in albedo as short statured (<12 cm in height) dry tundra on flat terrain at Barrow transitioned from spring melt to growing season, but this response was modulated by the amount of standing water. To put these seasonal increases in albedo into context, in our study, some land cover types increased their albedo by approximately 40% during the summer, which is as large as the range of albedo values from forest to tundra (Thompson et al., 2004).

Forecasting future albedo and surface energy balance for tundra communities must consider the rate of vegetation change, shrub encroachment, grazing, snow accumulation, and other processes (Cohen et al., 2013). Short statured shrubs (<0.5m)

are expected to increase in abundance (Bret-Harte et al., 2001; Epstein et al., 2004), cover (Pearson et al., 2013) and height (Walker et al., 2006), and recent studies indicate that *Betula spp.* in particular are likely to thrive in a warmer Arctic (Euskirchen et al., 2009; Heskell et al., 2013). One consequence of these changes to shrub tundra is that albedo in the Arctic will be dependent on the relative expansion of different shrub species with contrasting growth forms, especially at decadal scales where shrubs are expected to respond to climate forcing more quickly than trees (Sturm et al., 2001). Furthermore the peak period of greenness in Arctic deciduous shrubs appears to be increasing (Sweet et al., 2015), so it follows that the peak period of growing season albedo for shrubs will also lengthen and on average increase the growing season albedo. The spatial patterns associated with shrub cover change such as species-specific infilling versus expansion (Tape et al., 2006) and expansion into new, previously unvegetated territory (Frost & Epstein, 2014; Tape et al., 2012), must be considered when making projections of future shrub-dominated tundra albedo and energy balance. If the projection of low statured shrub cover increase is accurate and it outpaces the increases in tall statured growth (i.e., *Betula* gains more than *Salix*) then, future landscape level tundra albedo taken as a whole might not necessarily decrease (Blok et al., 2011), as currently hypothesised (Chapin et al., 2005; Pearson et al., 2013). However, it must be recognised that Blok et al. (2011) collected their minimum albedo values between July 12 and August 13, and thus missed the actual minimum albedo values associated with pre-leaf shrub cover.

Any increase in shrub cover and the associated growing season increase in albedo will be countered by the decrease in winter albedo caused by branches in or

above the snow (Sturm et al., 2005) or changes related to surface moisture. An increase in soil moisture will generally decrease albedo, but can also promote the growth of woody vegetation, which could increase growing season albedo. Similarly, changing surface hydrology has a strong influence on albedo, and this is particularly relevant for coastal arctic regions that appear to be drying (Smith et al. 2005, Andresen and Lougheed 2015). Although the rate of succession from tundra to shrub and the associated changes in albedo will occur over decades, any replacement of bare ground (Elmendorf et al., 2012) or talus with vegetation will increase growing season albedo. The establishment of vegetation within talus patches, which exhibit the lowest albedo of any cover type reported here, is a slow successional process (Danby et al. 2011), and will likely occur over a longer period than shrub encroachment or infilling. Lastly, growing-season albedo can increase for sparsely vegetated tundra as it dries out through the growing season (Harding & Lloyd, 1998) and more generally as tundra dries due to snow cover decreases and temperature increases in the Arctic. These changes will partially mitigate any effect of earlier snowmelt on annual energy balance and act as a negative sensible heating feedback to climate on a decadal scale.

Regardless of the rate of succession it should be pointed out that the albedo differences between tundra vegetation classes are relatively small (peak growing season albedo difference between tundra classes (Barren, Graminoid and Shrub) is approximately 3-4%) and entire summer differences in energy balance have been measured to be 3-5% greater for forest than tundra (Lafleur et al., 1992), which suggests that changes between tundra vegetation classes will produce modest changes in energy balance over the next century.

Recent projections of a wetter Arctic (e.g., Cook et al., 2014) suggests that shrubs growth will increase due to their affinity for drainage networks (Tape et al., 2012), but the effect on albedo will respond regionally, where the variations in temperature, moisture and vegetation will dictate albedo dynamics. On the other hand, large regions of arctic tundra are actually showing surface drying trends as permafrost deepens (Smith et al. 2005, Andresen and Lougheed 2015), and such drying has been associated with reduced vegetation growth (Gamon et al. 2013). Consequently, hydrological changes are likely to be a major source of uncertainty in albedo projections associated with climate change.

Conclusions

Albedo was measured along a 200 m transect of four different tundra vegetation types, which included different canopy coverage amounts of *Salix*, at the altitudinal limit of shrub succession in the southwest Yukon. The albedo of tundra vegetation increases from snow off conditions to the peak of the growing season differently for different vegetation types. Shrub species showed a large difference, where *Betula* had the highest albedo and *Salix* the lowest. Increases in albedo throughout the growing season were largest for shrubs with closed canopies. The summer albedo increase, which varied according to the different vegetation cover groups, acts to partially negate the effect of earlier spring snowmelt on surface energy balance. More detailed landscape albedo characterisations, especially those derived from remote sensing and ecosystem modelling are required to resolve growing season albedo dynamics over tundra. These

characterisations must include the relative abundance of different ground cover types, including barren and shrub species adjusted for growth forms and phenology, and should also consider patterns of changing surface hydrology. The feedback relationships between energy budgets and land cover in the Arctic will require these more detailed observations and measurements, at least at the beginning of the snow-free period and peak growing season. Future albedo-mediated sensible heating feedbacks related to changes in tundra vegetation could be positive or negative, but will likely remain small in magnitude over at least the next several decades.

Table 5-1: Site characteristics for representative tundra plant communities. Dominant plant cover is presented as a percentage of plot area, and was assessed using the point intercept method. Vascular plants were identified to species, but are grouped here to the main functional types of interest. Cover by different plant groups overlaps, so percentages do not sum to 100%. Mean growing season albedo (\pm SD) is the average of measurements acquired one hour around solar noon July and August for 2012. The 2013 albedo values (\pm SD) are the averages of July 15 and 29 measurements recorded over 10 minutes at each site under direct sunlight within two hours of solar noon.

Site	A	B	C	D	E	F
General description	Sparse canopy <i>Salix</i>	Mid canopy <i>Salix</i>	Dense canopy <i>Salix</i>	<i>Carex</i>	<i>Betula</i>	<i>Dryas</i> /lichen
<i>Betula glandulosa</i>	0	0	0	0	100	0
<i>Salix pulchra</i>	48	88	99	0	0	0
Graminoid*	62	45	6	95	3	19
Moss	77	19	71	42	0	2
<i>Dryas octopetala</i>	0	0	0	0	0	52
Lichen	0	0	0	0	0	34
Dwarf <i>Salix</i> spp. **	0	33	0	36	0	16
Forbs	28	45	23	1	3	24
Canopy height (m)	0.20	0.51	0.55	0.15	0.17	0.01
2012 Mean Albedo	0.165 \pm 0.003	0.144 \pm 0.002	0.136 \pm 0.002	0.183 \pm 0.003	0.191 \pm 0.002	0.190 \pm 0.003
July 15, 2013 Albedo	0.169 \pm 0.001	0.144 \pm 0.001	0.156 \pm 0.002	0.193 \pm 0.001	0.194 \pm 0.001	0.191 \pm 0.001
July 29, 2013 Albedo	0.164 \pm 0.001	0.155 \pm 0.001	0.164 \pm 0.002	0.199 \pm 0.001	0.197 \pm 0.002	0.208 \pm 0.001
2013 Mean Albedo	0.167 \pm 0.001	0.150 \pm 0.001	0.160 \pm 0.003	0.196 \pm 0.001	0.196 \pm 0.002	0.199 \pm 0.001

* *Carex* sp. predominantly *C. consimilis*; ** Dwarf *Salix* – *S. reticulata* & *S. polaris*

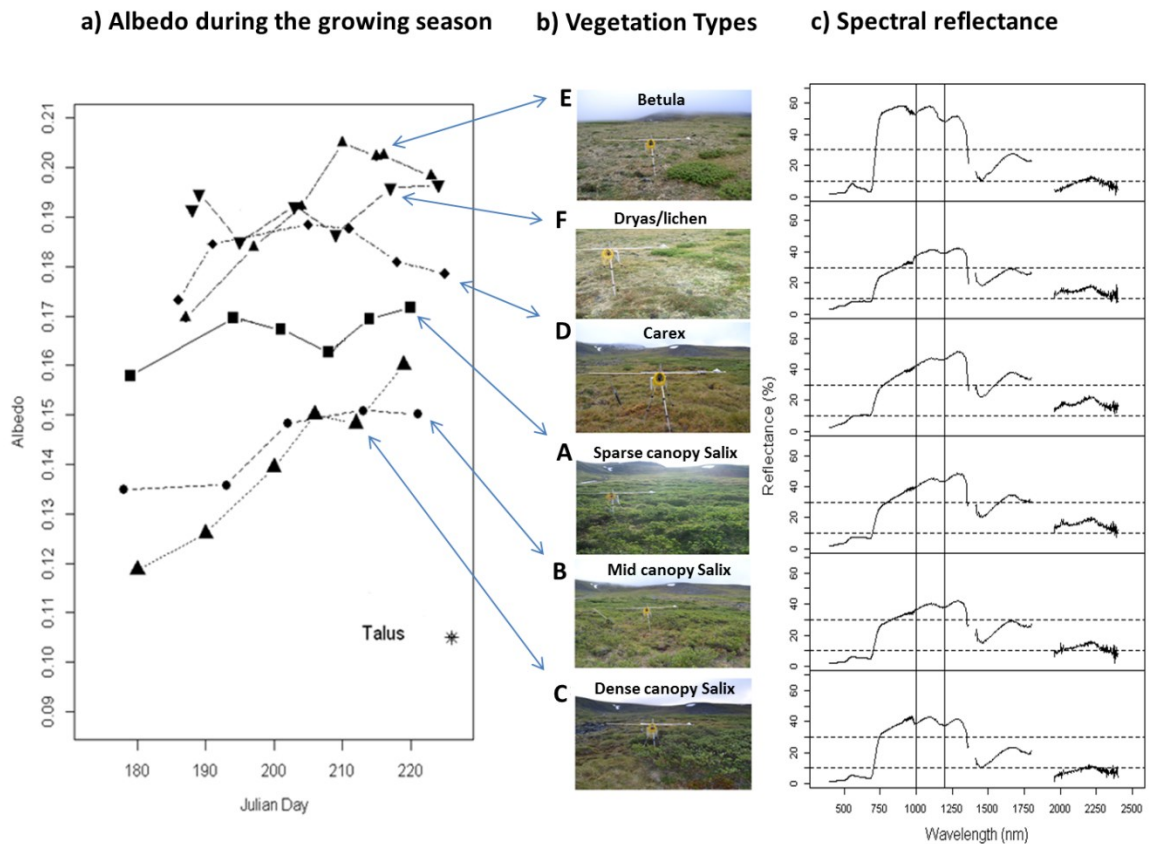


Figure 5-1: Characteristics of the six dominant vegetation types. a) Average broadband albedo during June, July and August 2012 (closed points) calculated for one hour before and after solar noon, compiled from 1-min averages for the six vegetation cover types; standard deviations for albedo measurements ranged from 0.001 to 0.006 indicating the standard errors are on the same order of size as the point symbols, thus no error bars are included. b) Photographs of the six sites. c) Spectral reflectance of the 6 sites on 15 August 2012. Areas in the scans affected by atmospheric water content have been removed. The depths of troughs at ~1000 nm and ~1200 nm (vertical lines) are indicative of Leaf Area Index (LAI), where deeper troughs indicate higher LAI. The two dotted horizontal lines at reflectance values of 10% and 30% are for reference. The 2013 albedo values have been omitted for clarity.

Albedo changes with seasonal phenology

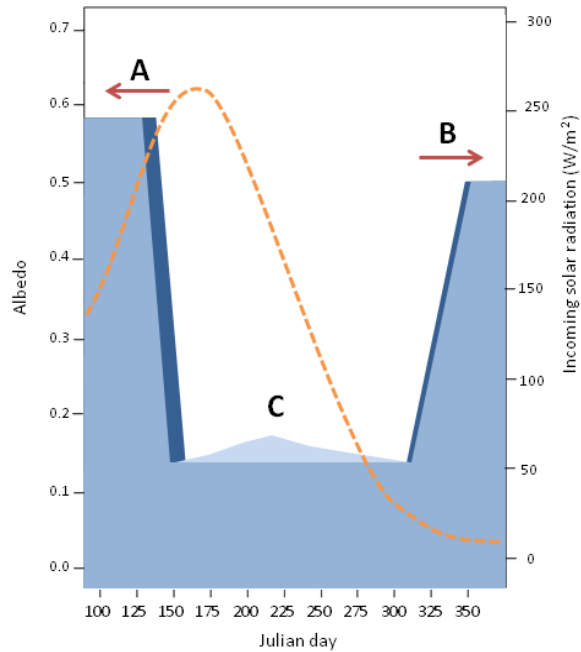


Figure 5-2: Conceptual models of albedo change related to seasonal phenology and tundra vegetation. The potential for increasing growing season albedo in tundra landscapes has been attributed to advanced spring snowmelt (A) and delayed onset of snow at the end of summer (B). The darker areas represent the amount of increased heating attributed to a change in snow cover albedo and this influence will generally be much greater in spring compared to late summer because there is more solar incoming radiation earlier in the season (dashed line; W/m², data calculated at 61.2° N; 138.3° W for 70% cloud cover which was the decadal average cloud cover from 2000-2010 at this site). Based on our measurements in Figure 5-1, summer (2012) average albedo will be greatest near the end of the growing season (C; light blue), however the average increase in albedo over the snow-free season has the potential to partially negate increased heating caused by advanced snowmelt or delayed onset when calculated for the entire snow free season.

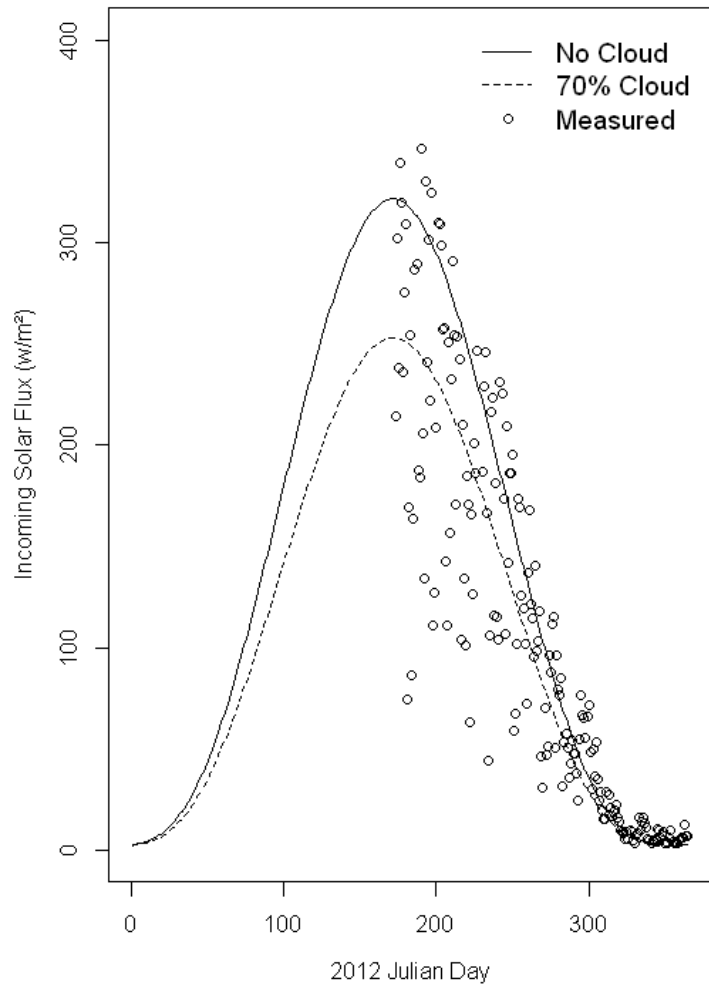


Figure 5-3: Modeled daily average incoming solar radiation with no clouds (solid line) and with 70% cloud cover (dashed line) for 2012. Instrumental values (open circles) are shown for CM6b field measurements of daily average incoming solar radiation between June 21 and December 30, 2012.

References

- Andresen, C.G., & Lougheed, V.L. (2015). Disappearing Arctic tundra ponds: Fine-scale analysis of surface hydrology in drained thaw lake basins over a 65 year period (1948-2013). *Journal of Geophysical Research Biogeosciences*, **120**, 466-479.
- Asner, P. (1998). Biophysical and biochemical sources of variability in canopy reflectance. *Remote Sensing of Environment*, **64**, 234-253.
- Beringer, J., Chapin, F.S., Thompson, C.C., & McGuire, A.D. (2005). Surface energy exchanges along a tundra-forest transition and feedbacks to climate. *Agricultural and Forest Meteorology*, **131**, 143-161.
- Bird, R.E., & Hulstrom, R.L. (1991). *A Simplified Clear Sky model for Direct and Diffuse Insolation on Horizontal Surfaces* by R.E. Bird and R.L. Hulstrom, SERI Technical Report SERI/TR-642-761. Solar Energy Research Institute, Golden, CO.
- Blanken, P.D., & Rouse, W.R. (1994). The role of Willow-Birch Forest in the Surface Energy Balance at Arctic Treeline. *Arctic and Alpine Research*, **26**, 403-411.
- Blok, D., Schaepman-Strub, G., Bartholomeus, H., Heijmans, M. M., Maximov, T. C., & Berendse, F. (2011). The response of Arctic vegetation to the summer climate: relation between shrub cover, NDVI, surface albedo and temperature. *Environmental Research Letters*, **6**, 035502, doi:10.1088/1748-9326/6/3/035502.
- Bras, R.L. *Hydrology*. (1990). Addison-Wesley, Reading, MA.
- Bret-Harte, M. S., Shaver, G. R., Zoerner, J. P., Johnstone, J. F., Wagner, J. L., Chavez, A. S., ... & Laundre, J. A. (2001). Developmental plasticity allows *Betula nana* to dominate tundra subjected to an altered environment. *Ecology*, **82**, 18-32.

- Brown, R., Derksen, C., & Wang, L. (2010). A multi-dataset analysis of variability and change in Arctic spring snow cover extent. *Journal of Geophysical Research*, **115**, D16111, doi:10.1029/2010JD013975.
- Chapin, F. S., Sturm, M., Serreze, M. C., McFadden, J. P., Key, J. R., Lloyd, A. H., McGuire, A. D., Rupp, T. S., Lynch, A. H., Schimel, J. P., Beringer, J., Chapman, W. L., Epstein, H. E., Euskirchen, E. S., Hinzman, L. D., Jia, G., Ping, C.-L., Tape, K. D., Thompson, C. D. C., Walker, D. A., & Welker, J. M. (2005). Role of land-surface changes in Arctic summer warming. *Science*, **310**, 657-660.
- Cohen, J., Pulliainen, J., Ménard, C.B., *et al.* (2013). Effects of reindeer grazing on snowmelt, albedo and energy balance based on satellite data analyses. *Remote Sensing of Environment*, **135**, 107-117.
- Cook, B.I., Smerdon, J.E., Seager, R., & Coats, S. (2014). Global warming and 21st century drying. *Climate Dynamics*, **43**, 2607-2627.
- Danby, R.K., Koh, S., Hik, D.S., & Price, L.W. (2011). Four decades of plant community change in the alpine tundra of southwest Yukon, Canada. *AMBIO*, **40**, 660-671.
- Elmendorf, S. C., Henry, G. H., Hollister, R. D., Björk, R. G., Boulanger-Lapointe, N., Cooper, E. J., ... & Wipf, S. (2012). Plot-scale evidence of tundra vegetation change and links to recent summer warming. *Nature Climate Change*, **2**, 453-457.

- Epstein, H.E., Calef, M.P., Walker, M.D., Chapin, F.S., & Starfield, A.M. (2004). Detecting changes in Arctic tundra plant communities in response to warming over decadal time scales. *Global Change Biology*, **10**, 1325-1334.
- Eugster, W., Rouse, W. R., Pielke, R. A., McFadden, J. P., Baldocchi, D. D., Kittel, T. G. F., Chapin, F. S., Liston, G. E., Vidale, P. L., Vaganov, E., & Chambers, S. (2000). Land-atmosphere energy exchange in Arctic tundra and boreal forest: available data and feedbacks to climate. *Global Change Biology*, **6**, 84-115.
- Euskirchen, E.S., McGuire, A.D., Chapin, F.S., & Thompson, C.C. (2009). Changes in vegetation in northern Alaska under scenarios of climate change, 2003-2100: implications for climate feedbacks. *Ecological Applications*, **19**, 1022-1043.
- Frost, G.V., & Epstein, H.E. (2014). Tall shrub expansion in Siberian tundra ecotones since the 1960s. *Global Change Biology*, **20**, 1264-1277.
- Gamon, J.A., Huemmrich, K.F., Stone, R.S., & Tweedie, C. (2013). Spatial and Temporal Variation in Primary Productivity (NDVI) of Coastal Alaskan Tundra: Decreased Vegetation Growth following Earlier Snowmelt. *Remote Sensing of Environment*, **129**, 144-153.
- Hallinger, M., Manthey, M., & Wilmking, M. (2010). Establishing a missing link: warm summers and winter snow cover promote shrub expansion into alpine tundra in Scandinavia. *New Phytologist*, **186**, 890-899.
- Harding, R.J., & Lloyd, C.R. (1998). Fluxes of Water and Energy from Three High Latitude Tundra Sites in Svalbard. *Nordic Hydrology*, **29**, 267-284.

- Heskel, M., Greaves, H., Kornfeld, A., *et al.* (2013). Differential physiological responses to environmental change promote woody shrub expansion. *Ecology and Evolution*, **3**, 1149-1162.
- Lafleur, P.M., Rouse, W.R., & Hardill, S.G. (1987). Components of the surface radiation balance of subArctic wetlands terrain units during the snow-free season. *Arctic and Alpine Research*, **19**, 53-63.
- Lafleur, P.M., Rouse, W.R., & Carlson, D.W. (1992). Energy balance difference and the hydrologic impacts across the northern treeline. *International Journal of Climatology* **12**, 193-203.
- Ohmura, A. (1981). *Climate and Energy Balance of Arctic Tundra*. Zürcher Geographische Schriften/ETH Zürich, Switzerland.
- Oke, T.R. (1987). *Boundary Layer Climates*. 2nd edn. Methuen, London.
- Pearson, R. G., Phillips, S. J., Loranty, M. M., Beck, P. S., Damoulas, T., Knight, S. J., & Goetz, S. J. (2013). Shifts in Arctic vegetation and associated feedbacks under climate change. *Nature Climate Change*, **3**, 673-677.
- R Development Core Team. (2011). *R: A language and environment for statistical computing*. R Foundation for Statistical Computing, Vienna, Austria. ISBN 3-900051-07-0; URL <http://www.R-project.org/>
- Ryan, P.J., & Stolzenbach, K.D. (1972). *Engineering Aspects of Heat Disposal From Power Generation* (D.R.F. Harleman, ed.). R.M. Parson Laboratory for Water

Resources and Hydrodynamics, Department of Civil Engineering, Massachusetts Institute of Technology, Cambridge, MA.

Sims, D.A., & Gamon, J.A. (2003). Estimation of vegetation water content and photosynthetic tissue area from spectral reflectance: a comparison of indices based on liquid water and chlorophyll absorption. *Remote Sensing of Environment*, **84**, 526-537.

Smith, L.C., Sheng, Y., MacDonald, G.M., & Hinzman, L.D. (2005). Disappearing arctic lakes. *Science*, **308**, 1429.

Snow, Water, Ice, Permafrost in the Arctic (SWIPA) (2011). Accessed 22 April 2013, <http://amap.no/swipa>.

Sturm, M., Racine, C., & Tape, K. (2001). Increasing shrub abundance in the Arctic. *Nature*, **411**, 546-547.

Sturm, M., Douglas, T., Racine, C., & Liston, G.E. (2005). Changing snow and shrub conditions affect albedo with global implications. *Journal of Geophysical Research*, **110**, G01004, doi: 10.1029/2005JG000013.

Sweet S.K., Griffin, K.L., Steltzer, H., Gough, L., & Boelman, N.T. (2015). Greater deciduous shrub abundance extends tundra peak season and increases modeled net CO₂ uptake. *Global Change Biology*, **21**, 2394-2409.

Tape, K., Sturm, M., & Racine, C. (2006). The evidence for shrub expansion in Northern Alaska and the Pan-Arctic. *Global Change Biology*, **12**, 686-702.

- Tape, K.D., Hallinger, M., Welker, J.M., & Ruess, R.W. (2012). Landscape heterogeneity of shrub expansion in Arctic Alaska. *Ecosystems*, **15**, 711-724.
- Thompson, C., Beringer, J., Chapin, F.S., & McGuire, A.D. (2004). Structural complexity and land-surface energy exchange along a gradient from Arctic tundra to boreal forest. *Journal of Vegetation Science*, **15**, 397-406.
- Walker, M. D., Wahren, C. H., Hollister, R. D., Henry, G. H., Ahlquist, L. E., Alatalo, J. M., ... & Wookey, P. A. (2006). Plant community responses to experimental warming across the tundra biome. *Proceedings of the National Academy of Sciences of the United States of America*, **103**, 1342-1346.
- Weller, G., & Holmgren, G. (1974). The Microclimate of the Arctic Tundra. *Journal of Applied Meteorology*, **13**, 854-862.
- Wood, S.N. (2006). *Generalized Additive Models: An Introduction with R*. Chapman and Hall/CRC.
- Zeng, H., Jia, G., & Epstein, H. (2011). Recent changes in phenology over the northern high latitudes detected from multi-satellite data. *Environmental Research Letters*, **6**, 045508, doi:10.1088/1748-9326/6/4/045508.
- Zheng, G., & Moskal, L.M. (2009). Retrieving Leaf Area Index (LAI) using remote sensing: theories, methods and sensors. *Sensors*, **9**, 2719-2745.
- Zuur, A.F., Ieno, E.N., Walker, N.J., Saveliev, A.A., & Smith, G.M. (2009). *Mixed Effects Models and Extensions in Ecology with R*, Springer.

CHAPTER SIX

Spring snow cover decline in altitudinal tundra provides a minimal contribution to Arctic temperature amplification

Introduction

The annual average surface air temperature at latitudes greater than 60 °N have become consistently warmer than the global average since 2000 (Overland et al., 2014). Arctic temperature is rising at a rate greater than two times faster than the globe as a whole (AMAP, 2012) where the air temperature has increased by 0.72 °C since 1950 (IPCC, 2013). Differential warming by increasing latitude is known as Arctic amplification, a phenomenon in the northern hemisphere which has occurred simultaneously with snow cover reduction (e.g., Serreze et al., 2009; Serreze & Barry, 2011). The pan-Arctic snow cover extent has decreased by 14% in May and 46% in June between 1967 and 2008 (Brown et al., 2010). Increasing air temperature results in decreased snow cover extent and duration (Euskirchen et al., 2006; Dye & Tucker, 2003); however, the influence of the resulting decrease in albedo on surface temperature is unclear. The amplification related to local versus external influences is still a matter of debate. Evidence for spring terrestrial warming in the Northern Hemisphere being partially related to a snow cover reduction has been reported by Déry & Brown (2007) and Groisman et al. (1994). Northern Hemisphere albedo feedback, which include changes from sea-ice cover and terrestrial snow cover, have been calculated as 0.3-1.1 W m⁻² K⁻¹, between 1979 and 2008 (Flanner et al., 2011). This range is larger than AR4

multi-model albedo feedback of $0.26 \pm 0.08 \text{ W m}^{-2} \text{ K}^{-1}$ by Soden & Held (2006) and those calculated from 18 CMIP3 models by Flanner et al. (2011). The amount of summer warming in Alaska related to the decrease in snow cover has been calculated by Chapin et al. (2005) for a study period between 1982 and 1999 was calculated to be 3.3 W m^{-2} per decade; they attributed the increase predominantly to snow cover decline because over the same period cloud cover has increased.

An alternative to snow albedo feedback (SAF) driving Arctic amplification is the possibility that external forcing has been driving warming. Through the investigation of re-analysis data, Arctic amplification is shown to be heavily dependent upon the transport of heat from low latitudes (Graversen et al., 2008; Screen & Simmonds, 2010), which these authors deduce from year-round warming of the Arctic mid-troposphere. However, in the terrestrial Arctic the influence by local factors (such as snow cover decrease) on surface warming is still a matter of debate largely because it is difficult to isolate local from external factors in observation data or reanalysis (Screen et al., 2012), especially in spring when multiple processes occur simultaneously. In the absence of a coherent observational assessment of the strength of the snow albedo feedback, model simulations provide some insight into the SAF. Winton (2006) showed through the neutralization of SAF in 12 AR4 models that have regionally fitted zero-dimensional energy balance, SAF was not a dominating factor in Arctic amplification. However, Crook et al. (2011) found that the multiple types of forcing between models for high-latitude regions were broad enough that it was difficult to define the particular causes of Arctic temperature increase. Lastly, Screen (2014) found that Arctic amplification

produces the largest signal in the autumn, which suggests that the SAF in spring related to snow cover decline is not producing a large contribution to temperature change.

We use a natural experiment to determine the effect that terrestrial snow cover reduction has in modulating surface temperature in spring and summer in the southwest Yukon between 2000 and 2008. Previous analysis (Chapter Four) indicates that maximum LST and downscaled NARR temperatures are sensitive to snow cover change. The steep elevation gradient dictates differential rates of snow cover loss at different elevations and on different land cover types. Thus an increase in temperature should be the response to decreasing snow cover. However, this temperature increase cannot be attributed exclusively to local snow cover change as feedbacks and forcings can, and usually do, occur ensemble. To separate feedback from forcing, spring snow cover at high elevation sites, where no snow cover change was observed, was compared to mid-elevation areas where large amounts of snow cover change has occurred, between 2000 and 2008. Further, these two areas are compared to low elevation areas where the spring snow cover melt precedes the mid-elevation areas. The simultaneous comparison of temperature trends originating from snow covered areas, changing snow covered areas and areas with no snow cover also provides the ability to define the influence of local vs. external factors on snow melt.

Study Area

The study area (Figure 6-1) is bounded by the Yukon – Alaska border on the west (141 °W) and southwest, Yukon – British Columbia border on the south (60°N), 138 °W

on the east and 62 °N on the north. The study area has a large negative west to east elevation gradient of ~5,000 m decreasing from Mt Logan (5,959 m to Kluane Lake 780 m) over approximately 120 km. Snow cover duration in the southwest Yukon has declined in both spring and fall by 6 – 8 days per decade in both spring and fall between 1967 and 2007 (Brown et al., 2010). Further, Alaska and the Yukon have warmed between 1 – 3 °C over the last 50 years (Arctic Climate Impact Assessment – ACIA, 2005; Snow, Water Ice, Permafrost in the Arctic - SWIPA, 2011). 11 land cover types (GLOBCOVER - (<http://due.esrin.esa.int/globcover/>)) occur in the study area. Three land covers were retained for analysis: Conifer forest (Conifer), Sparse vegetation plus Bare areas (Tundra) and Permanent Snow and Ice (Icefield). The Conifer group has the lowest average elevation (937 m ± 177 m – one standard deviation) and the Icefield group is the highest (2,325 m ± 702 m). Between these two groups is the Tundra group which has an average elevation of 1,656 m (± 459 m). The study region has a total area of 34,878 km², of which the Icefield measures 11,923 km², Tundra 10,703 km² and Conifer 4,163 km². Approximately 2/3 of the study area is without a treed canopy or significant amounts of vegetation that might bias the remote detection of snow cover or modify the three-dimensional temperature structure in relation to snow cover at ground level. Another advantage of using this study area is the ability to conduct analysis of temperature changes related to snow cover loss on Tundra simultaneously with Permanent Snow and Ice cover that is not changing appreciably and with Conifer Forest class which is largely devoid of snow cover by the beginning of May.

The southwest Yukon lies in the rain shadow of the St. Elias mountain range, which is modulated by the position of the Aleutian Low (Trenberth & Hurrell, 1994).

Furthermore the Pacific Decadal Oscillation index (PDO), or the standardised principle component time series of monthly Pacific sea surface temperatures, can help to quantify the effect Pacific Ocean surface temperatures has on modulation of summer temperature and snow cover in the Pacific North-west to Alaska. During the PDO in positive phase, the wintertime Aleutian Low moves southward resulting in positive temperature anomalies in north-west North America (Mantua & Hare, 2002). Although PDO is often well correlated with precipitation proxies such as those found in ice core records using decadal anomalies, its relationship to climate using annual anomalies is complex (Moore, et al., 2002).

Methods

In this study we use infrared Land Surface Temperature (LST) from the MODIS sensors on the Terra and Aqua platforms; fractional snow cover and cloud cover from the MODIS sensor on Terra. In addition, we use dynamically downscaled North American Regional Reanalysis and meteorological station measurements of air temperature. Monthly averages for MODIS data are composed of four eight-day periods that start on non-leap year Julian day 121. The monthly averages correspond to the months of May, June and July between 2000 and 2008.

MODIS LST

The MODIS LST data are clear-sky reprocessed version 5 Terra and Aqua

(MOD11L2 and MYD11L2) LST swath data, gridded at 1 km, produced using the split window technique (Wan et al. 2002; Wan 2008) using MODIS bands 31 and 32 (10.78 – 11.28 μm and 11.77 – 12.27 μm). The split window uses a global land surface emissivity derived look-up table (Snyder et al. 1998) to correct for emissivity and atmospheric variations. MODIS data were downloaded from the Land Processes Distributed Active Archive Center – LPDAAC (<https://lpdaac.usgs.gov/>). The MOD11L2 data are composed of geolocation, sensor radiance data, atmospheric temperature and water profile, cloud mask, quarterly land cover, and snow cover MODIS products. The MYD11L2 and MOD11L2 swath data were reprojected from sinusoidal projection to 1 km Albers Equal Area Projection (WGS84) using nearest neighbour resampling. The daytime MODIS LST product cloud mask has a larger confidence in identifying contamination than the night-time mask (Ackerman et al. 1998), and previous work in the southwest Yukon has shown that cloud contamination is <13-17% of all grid cells, with a maximum temperature depression of 2 K caused by contamination (Williamson et al, 2013; see also Chapter Two). The LST was filtered for grid cells that showed anomalous values, caused by cloud or cloud shadow contamination or large view angles (Benali et al., 2012). We adopted an approach similar to that used by Reynolds et al. (2008) on AVHRR LST data for additional filtering of MODIS LST data. If a MODIS LST grid cell was <5 K than the average of the surrounding values within 2 km radius, or >3 K different than the standard deviation, it was eliminated from the analysis.

Maximum LST

Maximum LST was determined (i) by identifying MODIS Aqua and Terra swaths that corresponded to within 1 h before and after solar noon at 61° N and 139.5° W; and (ii) selecting the maximum value from multiple images for a given day (2 to 4 depending on how the 90 minute repeat orbital corresponds to the 2 hour interval around solar noon) for each 1 km grid cell. This method utilises the maximum overpass density to produce a narrowly distributed temperature product. The actual diurnal maximum surface temperature occurs when net radiation is equal to zero, and can happen up to several hours after solar noon and the last closest MODIS overpass. Maximum LST is of central importance because albedo decreases related to snow melt should correlate most strongly with daytime maximum temperatures, rather than minimum temperatures (e.g., Kothawale et al., 2010). Minimum LST values were not calculated because minimum LST (collected at night) skews average LST to low values compared to average air temperature (Westermann et al., 2012; Williamson et al., 2014; see also Chapter Three) and the bias becomes progressively larger when calculated over increasing snow fraction (Chapter 5).

MODIS Snow & Cloud cover

MODIS provides a measure of snow cover using an algorithm based on the normalised difference snow index (NDSI), normalised difference vegetation index for forested areas, a thermal mask and a cloud mask (Hall et al., 2002). The snow cover product used in this study is the MODIS Terra daily fractional snow cover product

produced at 500 metre resolution (MOD10A1) determined through regression equations of NDSI and fractional snow cover (e.g., Salomonson & Appel, 2004). The daily fractional snow cover was resampled to 1 km grid cells using an arithmetic average of the 4 possible values, ignoring values other than 0-100%. The daily maps of 1 km snow cover were aggregated to eight-day averages showing a value of 0-100% for each aggregated grid cell.

Grid cells in the 500 m MOD10A1 snow cover layers that were identified by the MODIS cloud mask as cloud covered were marked as such. Monthly fractional cloud cover maps were produced by averaging the original binary classification of cloud cover over the month, after which these 500 m grid cells were arithmetically averaged to 1 km. Cloud cover is daytime cloud cover because it is extracted from the snow cover product which incorporates visible portion of the electromagnetic spectrum.

NCEP North American Regional Re-analysis (NARR) downscaling

A mix of statistical and dynamical downscaling methods were applied to North American Regional Reanalysis (NARR) 500 mbar air temperature to produce the downscaled temperature product used in this study. NARR is National Center for Environmental Prediction (NCEP) product that uses surface, radiosonde, and satellite data combined in the Eta forecasting system (Mesinger et al., 2006). The downscaling method uses a two-part, piece-wise fitting to NARR vertical air profiles and subsequent interpolation of those fitting parameters to a 200 m grid for prediction of temperature at arbitrary elevation, while using an interpolation scheme that reconstructs vertical

temperature profiles from a regional reanalysis and does not require meteorological station measurements for tuning (Jarosch et al., 2012). This method was developed for western Canada with the aim of producing temperature fields that are more accurate than other downscaled products for high elevation, high vertical relief glaciated areas. Jarosch et al. (2012) report a mean bias of 0.5 °C for areas with high vertical relief, for the data set encompassing 1990 to 2008. Furthermore, a mean absolute error of no more than 2 °C for monthly averages was found when compared against station temperatures. The daily averaged downscaled NARR were resampled to 1 km grids using cubic convolution and averaged to monthly time periods. Further, daily averages were produced using observed snow cover as a mask.

Air Temperature

Air temperature was measured at the Burwash Landing Environment Canada weather station over the course of the study. This station is located within the conifer forest class at an elevation of 807 m and records no snow on the ground for May, June or July over the 2000 to 2008 study period. The data were obtained from Environment Canada's National Climate Archive (http://www.climate.weatheroffice.gc.ca/Welcome_e.html).

Pacific Decadal Oscillation (PDO)

Standardised monthly (May, June and July) values for the PDO index were

obtained from the University of Washington (<http://research.jisao.washington.edu/pdo/>) for 2000 to 2008.

Statistical analyses

All GIS analysis and data manipulation was conducted with ESRI's ArcGIS 10. Statistical analysis and visualisation was conducted using the R statistical programming language (R Development Core Team, 2008).

Results

Downscaled NARR surface temperature, Maximum LST, Snow Fraction and Cloud fraction are displayed as monthly averages for May (Figure 6-2), June (Figure 6-3) and July (Figure 6-4). In May, both measures of surface temperature increased between 2000 and 2005, after which they fell by 2008, but are still higher than at the beginning of the study for conifer and tundra. The Icefield showed an increase in NARR temperature, but the maximum LST remained below 0 °C and displayed less variability which is expected for a surface that is largely snow covered. In Tundra, the May snow cover trend is well correlated with the daytime cloud cover fraction ($R^2=0.90$), both of which show a steep decline between 2000 and 2005. The maximum LST over Tundra closely mirrored the snow cover fraction. The NARR trend in the Conifer class was very well correlated with the air temperatures recorded at the Burwash Landing Environment Canada monitoring station, and these values are indicated as the

black dots on Figures 6-2, 6-3 and 6-4: this was expected because Environment Canada air temperature data are assimilated within the NARR product.

The most striking feature in the May trends is the similarity between NARR temperature trends for different land cover and snow cover, despite the observation that the Icefield is almost completely snow covered, Tundra is decreasing in snow cover and conifer has little snow cover. Regression analysis of NARR values of Icefield versus Tundra ($R^2=0.93$) and Conifer versus Tundra ($R^2=0.96$) show very high degrees of correlation. This similarity in temperature trends occurs while Tundra experiences a decrease in snow cover by 35% between 2000 and 2008. Moreover, the linear slopes for the May NARR trends are very similar, with the tundra rate of temperature change by year being bracketed by Conifer and Icefield (Conifer = +0.38 °C/Year, Tundra = +0.33 °C/Year and Icefield = +0.25 °C/Year). The differential between May tundra maximum LST and NARR increased from 2.8 °C in 2000 to 9.5 °C in 2005, where snow cover changed from its highest to lowest levels, a decline of 50%. The remainder of the correlation co-efficient between Tundra and Icefield and Conifer is approximately 6%, which when applied to the NARR temperature increase in Tundra between 2000 and 2008 equates to a radiative feedback which includes snow cover loss of $<0.091 \text{ W m}^{-2}$ per decade. This feedback equates to $<0.82 \text{ W m}^{-2}$ over the nine-year study period.

Figure 6-3 (June averages) shows a large increase in the NARR temperature in 2004, which has a corresponding increase in maximum LST and decrease in cloud cover. However in 2006 there was an increase in conifer and tundra maximum LST, but not the icefield maximum LST, while there is no corresponding increase in the NARR temperature. These changes occur while a decrease in cloud cover occurred for Tundra

and Conifer, and increased for the Icefield. In July, there was also a large increase in cloud cover between 2006 and 2008, which corresponds to an increase then decrease in maximum LST and NARR temperatures for all three land cover classes (Figure 6-4: July averages).

The relationship between May NARR temperatures, maximum LST and cloud fraction as a function of snow fraction for tundra class was plotted to evaluate the degree of sensitivity of these variables to snow cover fraction. In order to mitigate any effect caused by the lapse rates over the elevation range of Tundra, we constrained this analysis to between 1,600 and 1,700 m over Tundra for the month of May. This range brackets the average elevation of the Tundra class (1,656 m). The results are presented individually for each year and include Elevation, NARR, LST and cloud fraction all of which are plotted versus snow fraction (Figures 6-5 to 6-14). With the exception of May 2000, the other plots of from May show negative trends between snow fraction and NARR surface temperature, as expected.

The large elevation gradient found in the Icefield was used to evaluate the May average NARR temperature trends in 1,000 m elevation bins, from 2,000 m to slightly below 6,000 m over the study period (Figure 6-15). The temperature change in 2000 – 2001 and 2006 – 2008 is uncoupled from elevation, such that in the first instance there is warming at high elevation and cooling at low elevation, in the second instance there is cooling at high elevation but a flat trend at low elevation. Between 2002 and 2005 the trends correlate in sign, but not magnitude; warming and cooling between years is greater at higher elevation, and is progressively diminished as elevation decreased.

Lastly, we plotted the monthly average PDO index values for the months of May, June and July (Figure 6-16). These trends are poorly correlated with the four variables analysed in this study, likely because of the short time series being evaluated.

Discussion

Elevation or a heterogeneous vertical distribution of snow cover appears not to be dictating the majority of the variability in the NARR temperature trends, with the potential exception of May 2000 (Figures 6-5 to 6-14). The temperature difference between 1700 m and 1600 m in the tundra should be less than 1 °C as expected by the adiabatic lapse rate. Thus NARR temperatures seem to be largely associated with (are negatively correlated with) snow cover extent. Maximum LST should converge with average air temperature over high snow cover fractions (see Chapter Five), but will rapidly grow larger than air temperature over areas with no snow cover. This is observed in Figure 6-2 comparing maximum LST to NARR for high snow cover fractions. Maximum LST however is an average of only clear sky days. Thus the large snow cover decrease in Tundra does not influence the average air temperature compared to Conifer or Icefield, both of which are expressing only very moderate snow cover changes. Furthermore, the similarity of May cloud cover trends over the three surface types indicates that differences in solar forcing are not the cause. Figure 6-2 shows that maximum LST has a greater rate of warming than average air temperature in May on Tundra, when snow cover is declining rapidly. This behaviour is indicative of a snow cover feedback. However the increased radiative energy is not being translated into an

increase in the May average air temperature even though the temperature differential increases as snow fraction diminishes between 2000 and 2005. To understand this behaviour, consideration of the snow albedo feedback (SAF) is required.

Here we used fractional snow cover, instead of albedo, in order to relate snow cover change to temperature change. Previous work has shown that the snow cover extent change contribute 70-80% of the SAF, where the majority of the difference is contributed by snow metamorphosis or aging (Fletcher et al., 2012). Albedo does not describe the amount of short wave radiation that is absorbed by the surface, but the ratio of incoming to outgoing and is unitless. The maximum value LST used here is the surface temperature during daytime coinciding within hours of solar noon when the incoming solar power/area is close to maximum. Further, this relationship is modified by daytime cloud cover, which serves to reduce the amount of incoming short wave radiation available to increase ground temperature, and then be radiated back to the atmosphere completing the feedback.

This effect can be seen using the June and July plots (Figures 6-3 and 6-4), which isolate the effect without the confounding effect of snow cover change in Tundra that occurs in May. At night air temperature is greater under cloud cover than under clear sky due to radiative losses. Thus, when comparing the increased energy emitted by a surface due to reduced snow cover to average air temperature, the daytime radiative forcing by the surface of the atmosphere is dampened by the fact that solar zenith angle are only large near solar noon and cloud cover (i.e., modulating total incoming solar radiation) and albedo change (i.e., the change in the length of the melt period). The SAF will be a small contributor to average air temperature increase, especially over a month

or longer time period. The high correlations of May NARR temperatures between Tundra and Icefield and Tundra and Conifer ($R^2=0.93$ and 0.96) indicates that the contribution of SAF is less than approximately 6% for May average temperature. Although this value likely includes the effects of other feedbacks, the dramatic decrease in snow cover suggests SAF is the dominant feedback component. The <6% value of the tundra NARR temperature trend equates to $<0.091 \text{ W m}^{-2}$ per decade over the 2000 to 2008 study period. This value is more than an order of magnitude less than that calculated by Chapin et al. (2005) (3.3 W m^{-2} per decade between 1982 and 1999 for the SAF in Alaska, likely because the effects of external influences on snow cover loss were not adequately considered.

Over the nine-year study period the feedback for May at surface increased by $<0.82 \text{ W m}^{-2}$. The values for the radiative feedback related to snow cover loss at TOA must then be less than $0.28 \text{ W M}^{-2} \text{ K}^{-1}$. This value is in better agreement with modeling results ($0.26 \pm 0.08 \text{ W m}^{-2} \text{ K}^{-1}$ (Soden & Held, 2006)) than recent observation studies (e.g., Flanner et al., 2011).

With the influence of the SAF being small when averaged into monthly or three monthly air temperatures, we can conclude that the temperature changes seen within the study site are related to external forcing such as meridional heat transport. The lockstep changes by the three surface types, even though they exhibit large differences in snow cover change, indicate these temperature profiles are reacting to a forcing that is being exerted on all three simultaneously. Although we examined a relatively small portion of the Northern Hemisphere, our results provide insight that can be used to interpret possible mechanisms driving apparent Arctic amplification. Graversen et al. (2008)

indicate that there is little evidence for a surface albedo feedback because amplified warming occurred well above the surface, which is consistent with our findings, but their use of three-month averages must reduce their ability to detect a feedback.

The Pacific North American pattern and Pacific Decadal Oscillation in positive phase can be used to explain some of the variability observed in the climate record and can also explain enhanced advection of warm air and winds into Alaska and Western Canada (McGuire et al., 2006). The amplification of warming and cooling found in the icefields with no snow cover change suggests that Elevational Dependent Warming (e.g. Pepin et al., 2015) must be related to large scale circulation patterns, and provides additional evidence that terrestrial snow cover loss is largely a response to external forcing, and not the primary cause. Further, the EDW trends supports the findings by Graversen et al. (2008) that high altitude warming by in the Arctic is more related to external heat transport than the snow-cover feedback. There is a strong correlation between snow cover and cloud cover, where cloud cover decrease is likely a manifestation of larger synoptic easterly air flow which brings water vapour from the Pacific to northwest Canada (Smirnov et al., 1999). For example, the extremely warm early part of 2004 has been attributed to the disruption of the Polar Vortex and warming in the atmospheric column up to 50 hPa (Manney et al., 2005). However the relationship to PDO and the position of the Aleutian Low is not clearly defined. The PDO analysed here correlates poorly with snow cover, cloud cover and temperature because our time series is not long enough to fully constrain the complexities of the PDO index, a behaviour that has been discussed for the study area previously (Moore et

al., 2002). However, a sufficiently long time series for the analysis of Elevation Dependent Warming is not currently available for the southwest Yukon.

Conclusions

We show that May snow cover decrease between 2000 and 2008 had only a small influence on the increase of surface air temperature in altitudinal tundra in the southwest Yukon. Variation in cloud cover mediated surface temperature to a small degree, but there was only a weak relationship to PDO. Although we observed evidence for a small snow cover temperature feedback (< 6 % contribution to the monthly average), the strength appears to be insufficient to measurably influence the measured surface temperature changes, which are most likely dictated by external factors, such as latitudinal heat transport. These findings contradict the results of Chapin et al. (2005) who indicated a much larger role for the snow-albedo feedback in increasing Alaskan temperature. It is likely that these differences can be explained by external forcing consistent with latitudinal heat transport.

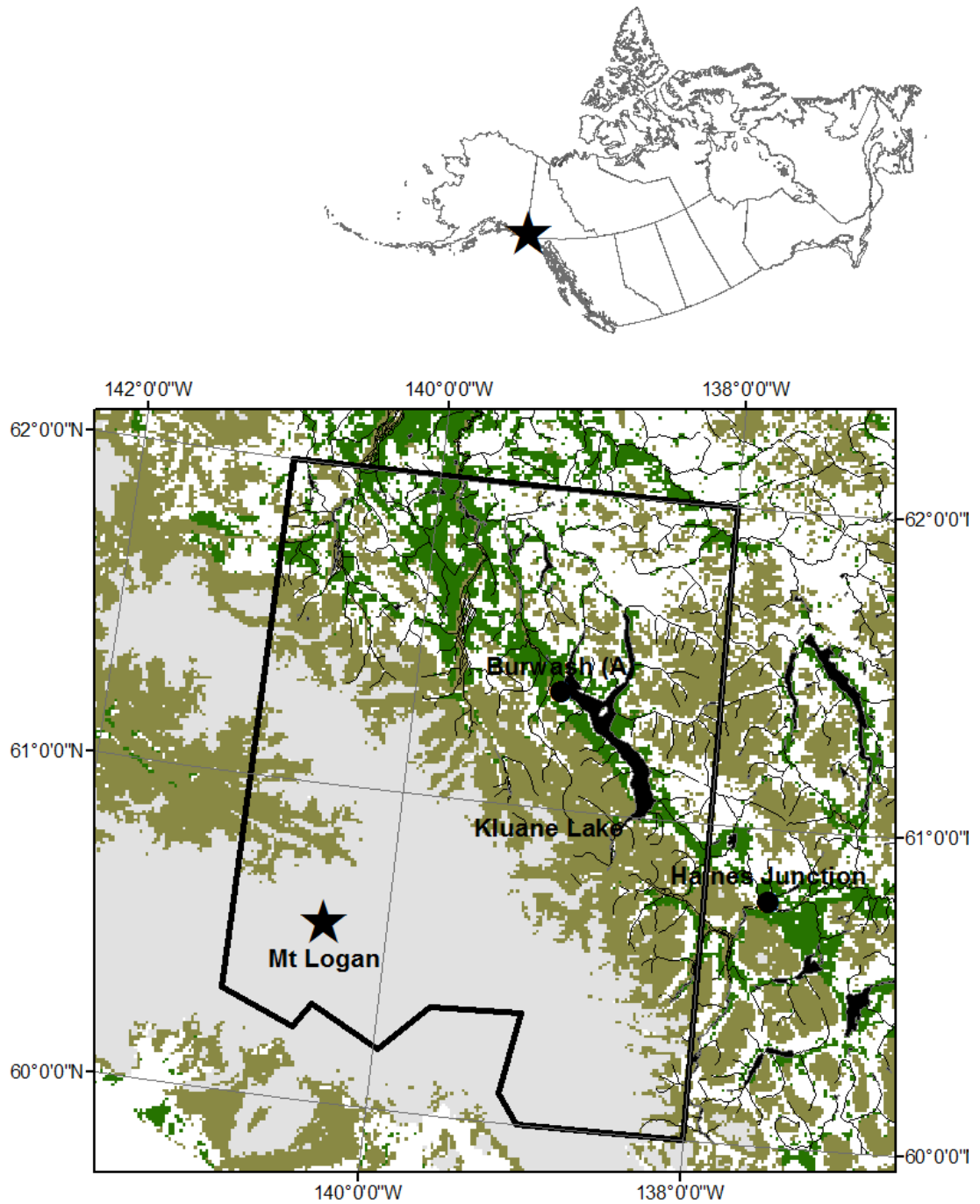


Figure 6-1: Figure 6-1: The southwest Yukon study area bounded by the thick black line. The grey portion is the glaciated region of Kluane National Park, olive colour indicates sparse vegetation (tundra) and the green indicates conifer forest. The elevational gradient extends from the summit of Mt Logan (5959 m) to Kluane Lake (780 m), and some lower elevation drainages. An Environment Canada meteorological monitoring station is located at Burwash Landing and is referred to as Burwash (A).

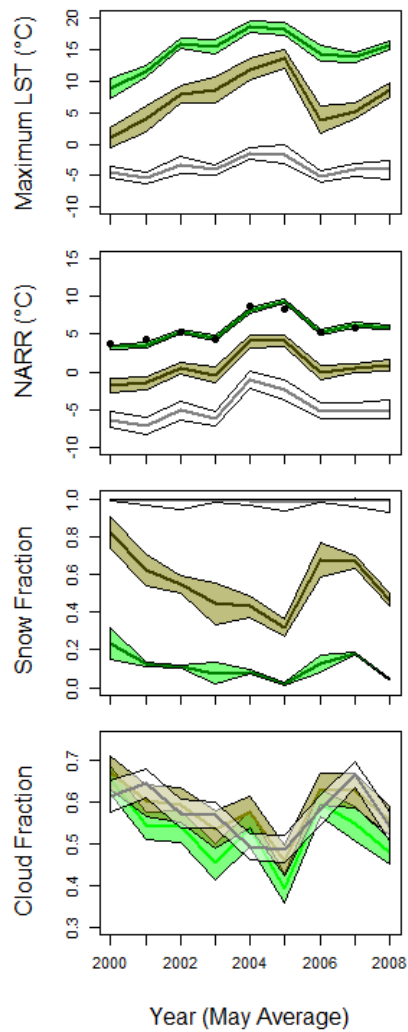


Figure 6-2: Plots of May monthly average Maximum Land Surface Temperature (top panel), Downscaled North American Regional Re-analysis surface temperatures (second panel from top), MODIS snow fraction (third panel from top) and MODIS cloud fraction (bottom panel) for the years 2000 through 2008. The dark green indicates trends indicate Conifer land cover, olive colour indicates Tundra, and White indicates Icefield. The bottom panel uses the same colour scheme, except the black line indicates Permanent Snow & Ice. The polygons surrounding the trend lines indicate standard error. The black dots on the NARR panel (second from top) are air temperature averages measured at the Burwash Landing monitoring station. May 2008 was omitted because of missing data. Standard error for the air temperatures are encapsulated within the black dot.

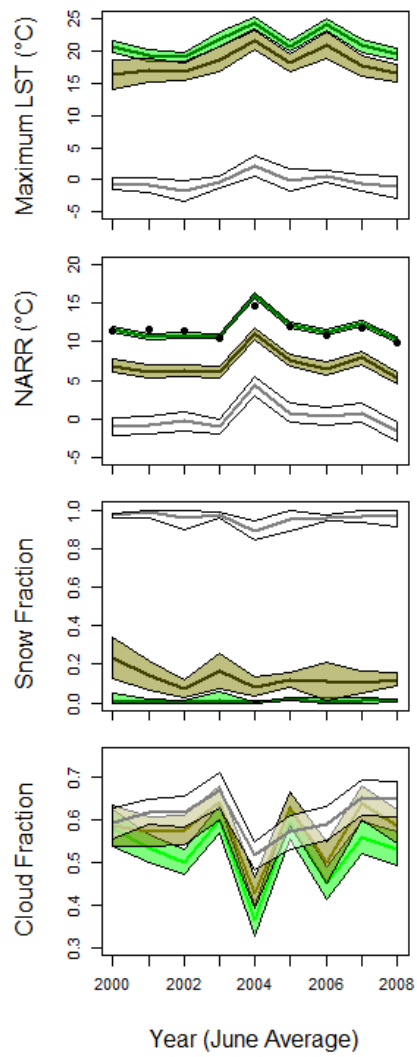


Figure 6-3: June averages of maximum LST, average NARR, snow fraction and cloud fraction. The material is displayed in the same format as Figure 2.

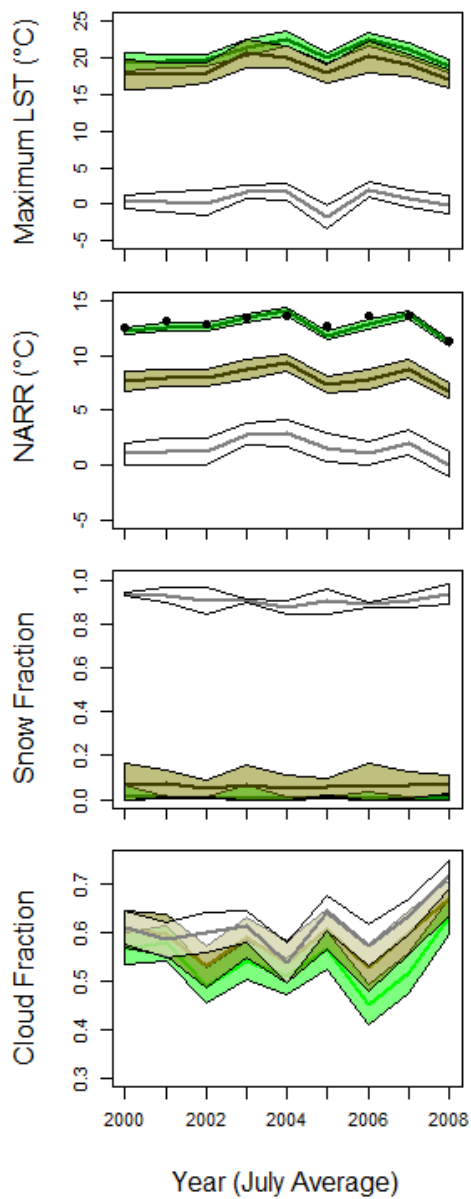
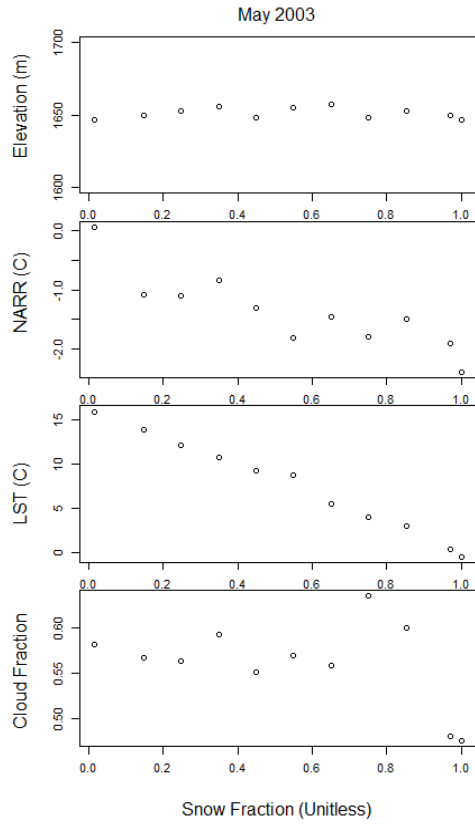
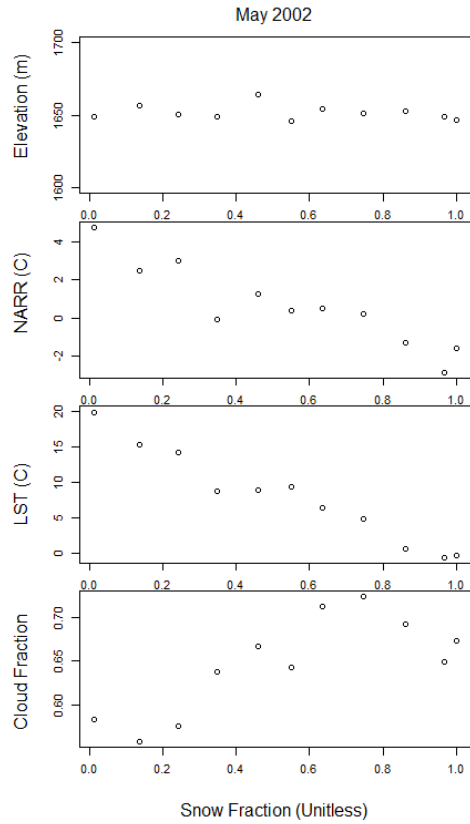
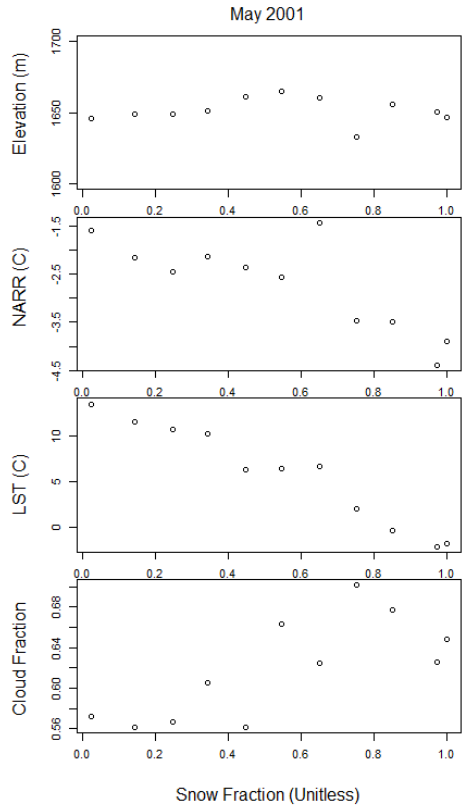
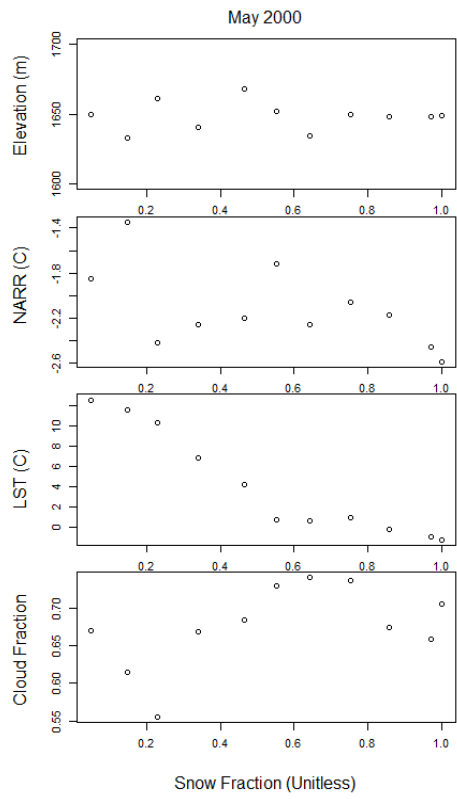
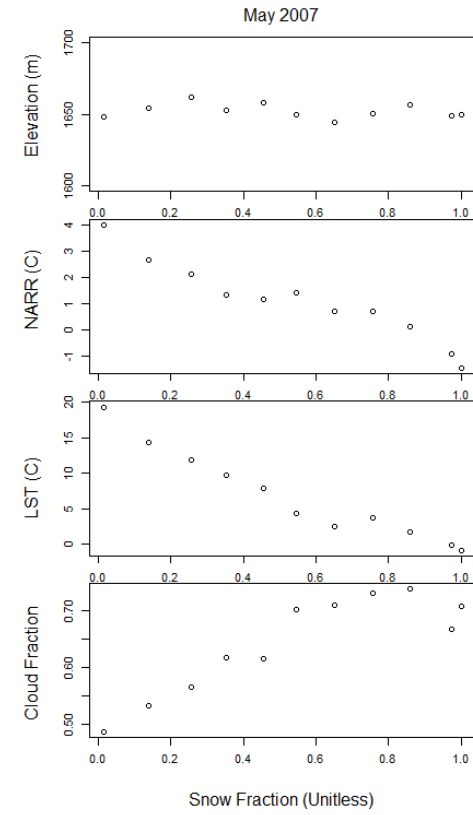
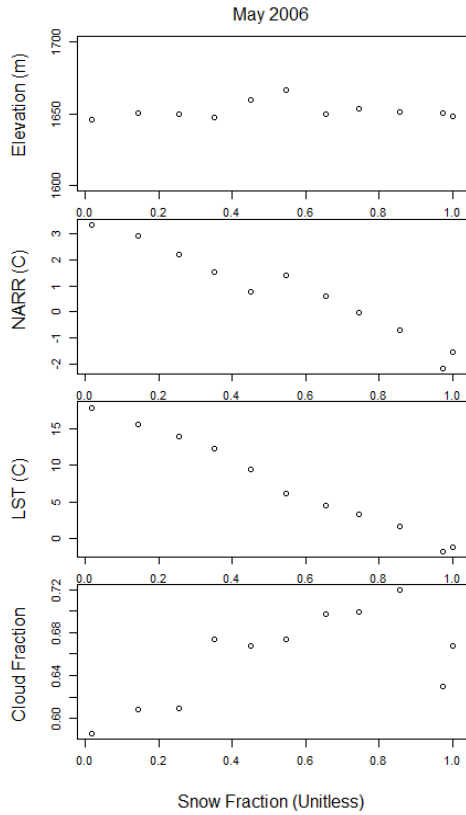
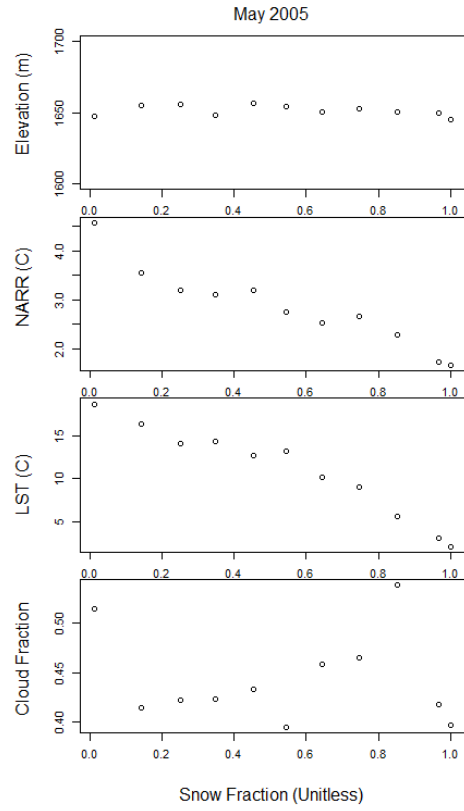
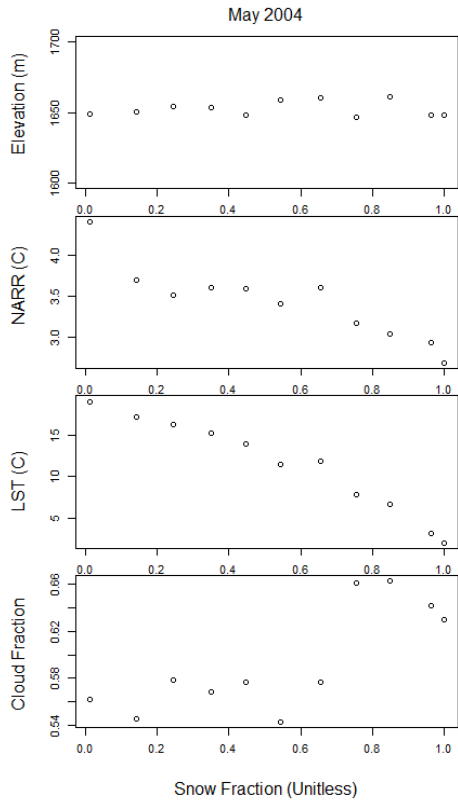
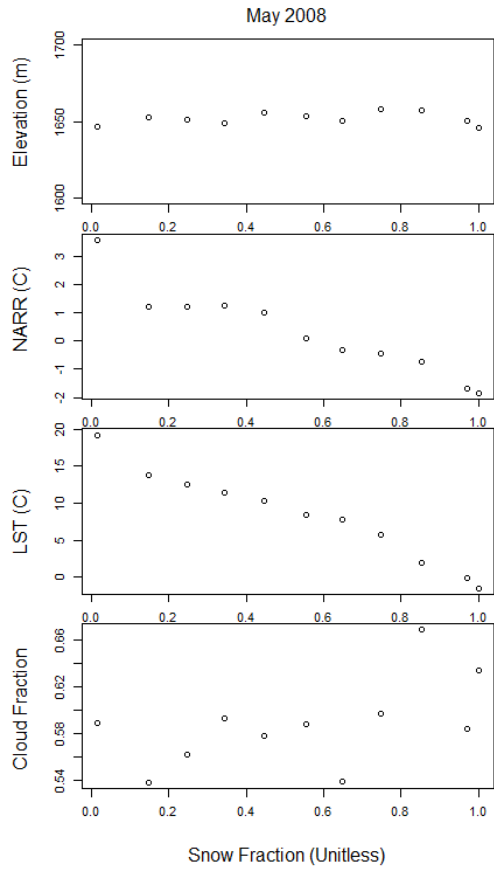


Figure 6-4: July averages of maximum LST, average NARR, snow fraction and cloud fraction. The material is displayed in the same format as Figure 2.







Figures 6-5 to 6-13: (May 2000 to May 2008 respectively). Each Figure is the four panel plot of the distribution of Elevation, NARR temperature, Maximum LST, and Cloud fraction in 0.1 snow fraction bins, for the Tundra class within the elevation range of 1600 to 1700 m.

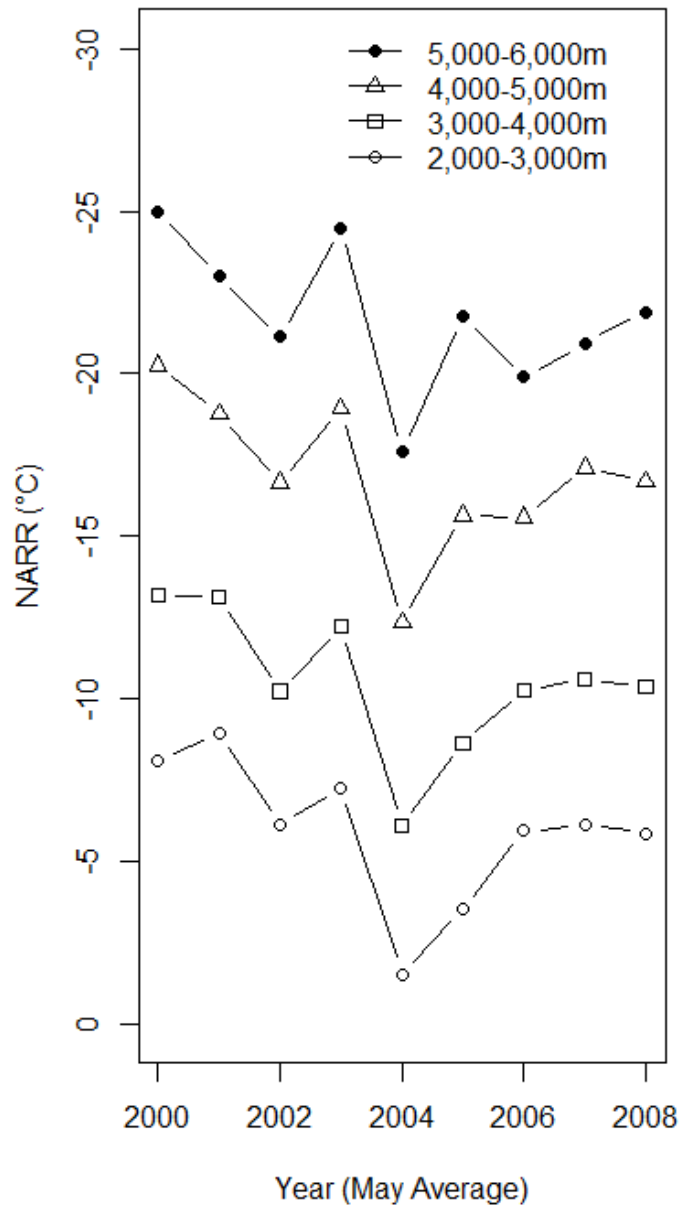


Figure 6-14: May average NARR temperature by 1,000 m elevation zone starting at 2,000 m for the Icefield where average snow cover fraction was greater than 99% for all points. The NARR temperature for the 2,000 – 3,000 m elevation band was calculated across an average 4,513 grid cells for each year. The 3,000 – 4,000 m band used on average 816 grid cells, 4,000 – 5,000 m 110 grid cells and >5,000 m used 19 grid cells.

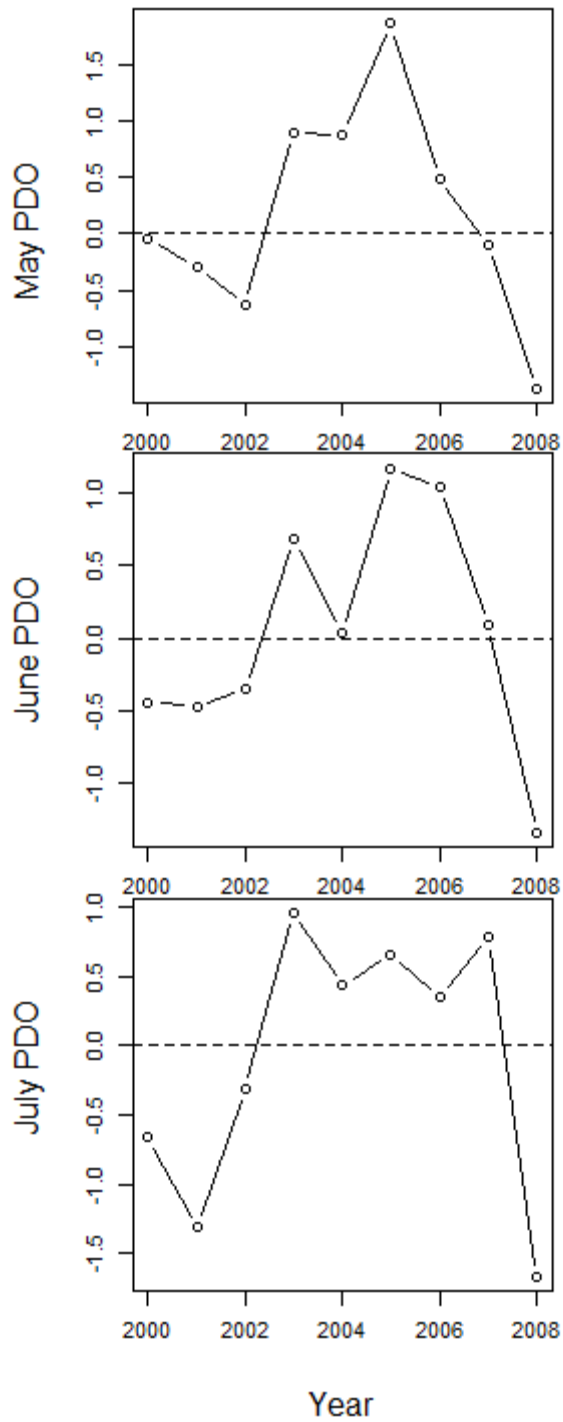


Figure 6-15: Pacific Decadal Oscillation (PDO) for May (top) June (middle) and July (bottom) between 2000 and 2008.

References

- AMAP (Arctic Monitoring and Assessment Programme) (2012). SWIPA overview report. In: Arctic Climate Issues 2011: Changes in Arctic Snow, Water, Ice and Permafrost (eds. Shearer, R., Wrona, F., Klint, M., Larsen, H., Skovgaard, O., Mahonen, O., Jensson, H., Dovle, P., Tsaturov, Y., Lundeberg, T., Armstrong, T., Solbakken, J.-I., pp. 30-40. Oslo, Norway.
- Arctic Climate Impact Assessment (ACIA) Report. (2005). Impacts of a warming Arctic. UK: Cambridge University Press 146 p.
- Ackerman, S.A., Strabala, K.I., Menzel, W.P., Frey, R.A., Moeller, C.C., & Gumley, L.E. (1998). Discriminating clear sky from clouds with MODIS. *Journal of Geophysical Research*, **103**, 32141- 32157.
- Benali, A., Carvalho, A.C., Nunes, J.P., Carvalhais, N., & Santos, A. (2012). Estimating air surface temperature in Portugal using MODIS LST data. *Remote Sensing of Environment*, **124**, 108-121.
- Brown, R., Derksen, C., & Wang, L. (2010). A multi-dataset analysis of variability and change in Arctic spring snow cover extent. *Journal of Geophysical Research*, **115**, D16111, doi:10.1029/2010JD013975.
- Chapin, F. S., Sturm, M., Serreze, M. C., McFadden, J. P., Key, J. R., Lloyd, A. H., McGuire, A. D., Rupp, T. S., Lynch, A. H., Schimel, J. P., Beringer, J., Chapman, W. L., Epstein, H. E., Euskirchen, E. S., Hinzman, L. D., Jia, G., Ping, C.-L., Tape, K. D., Thompson, C. D. C., Walker, D. A., & Welker, J. M. (2005). Role of land-surface

- changes in Arctic summer warming. *Science*, **310**, 657-660.
- Crook, J.A., Forster, P.M., & Stuber N. (2011). Spatial Patterns of Modeled Climate Feedback and Contributions to Temperature Response and Polar Amplification. *Journal of Climate*, **24**, 3575-3592.
- Déry, S.J., & Brown, R.D. (2007). Recent Northern Hemisphere snow cover extent trends and implications for the snow-cover feedback. *Geophysical Research Letters*, **34**, L22504, doi:10.1029/2007GL031474.
- Dye, D.G., & Tucker, C.J. (2003). Seasonality and trends in snow-cover, vegetation index, and temperature in northern Eurasia. *Geophysical Research Letters*, **30**, 1405, doi:10.1029/2002GL016384.
- Euskirchen, E. S., A. D. McGuire, D. W. Kicklighter, Q. Zhuang, J. S. Clein et al. (2006). Importance of recent shifts in soil thermal dynamics on growing season length, productivity, and carbon sequestration in terrestrial high-latitude ecosystems. *Global Change Biology*, **12**, 731-750.
- Flanner, M. G., Shell, K. M., Barlage, M., Pervich, D. K., & Tschudi, M. A. (2011). Radiative forcing and albedo feedback from the Northern Hemisphere cryosphere between 1979 and 2008. *Nature Geoscience*, **4**, 151-155.
- Fletcher, C.G., Zhao, H., Kushner, P.J., & Fernandes, R. (2012). Using models and satellite observations to evaluate the strength of snow albedo feedback. *Journal of Geophysical Research*, **17**, D11117, doi:10.1029/2012JD017724.
- Graversen, R., Mauritsen, T., Tjernström, M., Källén, E., & Svensson, G. (2008). Vertical structure of recent Arctic warming. *Nature*, **451**, 53-56.

- Groisman, P. Y., Karl, T. R., & Knight, R. W. (1994). Observed impact of snow cover on the heat balance and the rise of continental spring temperatures. *Science*, **263**, 198-200.
- Hall, D.K., Riggs, G.A., Salomonson, V.V., DiGirolamo, N.E., & Bayd, K.J. (2002). MODIS snow-cover products. *Remote Sensing of Environment*, **83**, 181-194.
- Intergovernmental Panel on Climate Change (IPCC) (2013). Fifth Assessment Report. In: Climate Change 2013 – Working Group 1: The Physical Science Basis (eds Stocker TF, Qin D, Plattner G-K, Tignor M, Allen SK, Boschung J, Nauels A, Xia Y, Bex V, Midgley PM), pp.130-194; 1257-1258. Cambridge University Press, Cambridge, UK.
- Jarosch, A.H., Anslow, F.S., & Clarke, G.K.C. (2012). High-resolution precipitation and temperature downscaling for glacier models. *Climate Dynamics*, **38**, doi: 10.1007/s00382-010-0949-1.
- Kothawale, D., Munot, A. & Kumar, K. K. (2010). Surface air temperature variability over India during 1901-2007, and its association with ENSO. *Climate Research*, **42**, 89-104.
- Manney, G.L., Kruger, K., Sabutis, J.L., Sena, S.A., & Pawson, S. (2005). The remarkable 2003-2004 winter and other recent warm winters in the Arctic stratosphere since the late 1990s. *Journal of Geophysical Research – Atmospheres*, **110**, doi:10.1029/2004JD005367.
- Mantua, N.J., & Hare, S.R. (2002). The Pacific Decadal Oscillation. *Journal of Oceanography*, **58**, 35-44.

- McGuire, A. D., Chapin, F. S., Walsh, J. E., & Wirth, C. (2006). Integrated Regional Changes in Arctic Climate Feedbacks: Implications for the Global Climate System. *Annual Review of Environment and Resources*, **31**, 61-91.
- Mesinger, F., DiMego, G., Kalnay, E., Mitchell, K., Shafran, P.C., Ebisuzaki, W., Jović, D., Woollen, J., Rogers, E., Berery, E.H., Ek, M.B., Fan, Y., Grumine, R., Higgins, W., Li, H., Lin, Y., Manikin, G., Parrish, D., & Shi, W. (2006). North American Regional Reanalysis. *Bulletin of the American Meteorological Society*, **87**, 343-360.
- Moore, G. W. K., Holdsworth, G., & Alverson, K. (2002). Climate change in the North Pacific region over the past three centuries. *Nature*, **420**, 401-403.
- Overland, J., Hanna, E., Hanssen-Bauer, I., Kim, S.-J., Walsh, J., Wang, M., & Bhatt, U.S. (2014). Arctic Report Card 2014 – Air Temperature.
www.Arctic.noaa.gov/reportcard/
- Pepin, N., Bradely R. S., Diaz, H. F., Baraer, M., Caceres, E. B., Forsythe, N., Fowler, H., Greenwood, G., Hasmi, M. Z., Liu, X. D., Miller, J., Ning, L., Ohmura, A., Palazzi, E., Rangwala, I., Schoener, W., Severskiy, I., Shahgedanova, M., Williamson, S. N., & Yang, D. Q. (2015). Elevation-Dependent Warming in Mountain Regions of the World. *Nature Climate Change*, **5**, 424-430.
- R Development Core Team (2008). R: A language and environment for statistical computing. R foundation for Statistical Computing, Vienna, Austria. ISBN 3-900051-070-0, URL <http://www.R-project.org>.
- Raynolds, M. K., Comiso, J. C., Walker, D. A., & Verbyla, D. (2008). Relationship

- between satellite-derived land surface temperature, Arctic vegetation types, and NDVI. *Remote Sensing of Environment*, **112**, 1884-1894.
- Salomonson, V. V., & Appel, I. (2004). Estimating fractional snow cover from MODIS using the normalised difference snow index. *Remote Sensing of Environment*, **89**, 351-360.
- Screen, J., & Simmonds, I. (2010). The central role of diminishing sea ice in recent Arctic temperature amplification. *Nature*, **464**, 1334-1337.
- Screen, J.A., Deser, C., & Simmonds, I. (2012). Local and remote controls on observed Arctic warming. *Geophysical Research Letters*, **39**, L10709, doi:10.1029/2012GL051598.
- Screen, J.A. (2014). Arctic amplification decreases temperature variance in northern mid- to hi-latitudes. *Nature Climate Change*, **4**, 577-582.
- Serreze, M., Barrett, A., Stroeve, J., Kindig, D., & Holland, M. (2009). The emergence of surface-based Arctic amplification. *Cryosphere*, **3**, 11-19.
- Serreze, M., & R. Barry. (2011). Processes and impacts of Arctic amplification: A research synthesis. *Global and Planetary Change*, **77**, 85-96.
- Snow, Water, Ice, Permafrost in the Arctic (SWIPA) (2011) Accessed 22 April 2013, <http://amap.no/swipa>
- Smirnov, V. V., & Moore, G. W. K. (1999). Spatial and temporal structure of atmospheric water vapor transport in the Mackenzie River basin. *Journal of Climate*, **12**, 681-696.

- Snyder, W.C., Wan, Z., Zhang, Y., & Feng, Y.Z. (1998). Classification-based emissivity for land surface temperature measurement from space. *International Journal of Remote Sensing*, **19**, 2753-2774.
- Trenberth, K.E., & Hurrell, J.W. (1994). Decadal atmosphere-ocean variability in the Pacific. *Climate Dynamics*, **9**, 303–309.
- Wan, Z., Zhang, Y., Zhang, Q., & Li, Z. (2002). Validation of the land-surface temperature product retrieved from Terra Moderate Resolution Imaging Spectroradiometer data. *Remote Sensing of Environment*, **83**, 163-180.
- Wan, Z. (2008). New refinements and validation of MODIS land-surface temperature/emissivity products. *Remote Sensing of Environment*, **112**, 59-74.
- Westermann, S., Langer, M., & Boike, J. (2012). Systematic bias of average winter-time land surface temperatures inferred from MODIS at a site on Svalbard, Norway. *Remote Sensing of Environment*, **118**, 162-167.
- Williamson, S. N., Hik, D. S., Gamon, J. A., Kavanaugh, J. L., & Koh, S. (2013). Evaluating the quality of clear-sky MODIS Terra daytime Land Surface Temperatures (LST) using ground based meteorology station observations. *Journal of Climate*, **26**, 1551-1560.
- Williamson, S. N., Hik, D. S., Gamon, J. A., Kavanaugh, J. L., & Flowers, G.E. (2014). Estimating Temperature Fields from MODIS Land Surface Temperature and Air Temperature Observations in a Sub-Arctic Alpine Environment. *Remote Sensing*, **6**, 946-963.

Winton, M. (2006). Amplified Arctic climate change: What does surface albedo feedback have to do with it? *Geophysical Research Letters*, **33**, doi:10.1029/2005GL025244.

CHAPTER SEVEN

Summary and Conclusions: Warming Arctic Mountains

Introduction

The Arctic is warming at a rate between 2 and 3 times faster than lower latitudes (IPCC, 2013). The annual average Arctic surface temperature has become consistently greater than the global average since 2000 (Overland et al., 2014). These phenomena describe a process known as Arctic amplification and its source has been hypothesised to be related to both latitudinal heat transport and local heating, mostly related to surface albedo changes (e.g., Serreze & Barry, 2011). However the relative contribution of local versus external influences to Arctic amplification is still a matter of debate, largely because the Arctic is difficult access, making the in-situ measurements and observations limited in number, length and geographical placement. Furthermore, the Arctic albedo feedback processes occur over different surface types at different spatial and temporal scales (e.g., albedo feedback from Arctic sea ice reduction versus the albedo feedback related to terrestrial snow cover reduction), and separating their influence to Arctic amplification is difficult.

Satellite remote sensing and modelled climate products are commonly used to fill the shortcomings of in-situ observations by providing a massive amount of spatially continuous data. However the validation by, and integration with field measurements and observations is also impacted by the small amount of measurements, which limits the ability to convert at sensor radiance or interpolation scheme into climate or

landscape surface function. For these reasons uncertainties remain about the mechanisms of Arctic surface and atmospheric processes in Arctic amplification and their relation to external forcing (Screen et al., 2012).

Summary of Results

This thesis considered various aspects of surface and climate measurement and function, focusing on the southwest Yukon. The first chapter provided a general overview of the study area and an introduction to Arctic amplification and surface energy balance related to snow cover and tundra land cover. Chapters two, three and four are concerned with the validation and aggregation of measurement and observation data; these chapters are primarily methodological. In chapter two we show that cloud contamination of MODIS infrared Land Surface Temperatures is similar to published values (Ackerman et al., 1998) and in the process we devised and validated a new cloud mask for the MODIS sensor. The influence of cloud and snow on LST remote sensing measurements is the topic of chapters three and four, and represents an extension of the work by Westermann et al. (2012), for spring conditions and variable snow covers. Chapter five involves the measurement and analysis of growing season albedo at a long-term study site in alpine tundra in the southwest Yukon. This is useful because it puts summer landscape albedo (annual minimum albedo occurs in the absence of snow) into context and shows that the growing season albedo increase is small compared to the albedo decrease caused by snow cover loss. Chapter six is an analysis of snow cover feedbacks to climate, and supports the findings of the importance of latitudinal heat

transport by Graversen et al. (2008) for the terrestrial Arctic temperature change.

Immediately following are chapter summaries, after which a general conclusion and ideas for further work are presented.

Chapter Two: Evaluating cloud contamination in clear-sky MODIS Terra daytime Land Surface Temperatures using ground-based meteorology station observations

We used Environment Canada meteorological station hourly sampled air temperatures (T_{air}) at two of four stations in the southwest Yukon to identify cloud contamination in MODIS (MOD11A1 – Collection 5) Terra clear-sky daytime Land Surface Temperatures (LST) that is not flagged by the MODIS quality algorithm as contaminated. We did so by using qualitative ground-based sky condition observations and coincident MODIS quality flag information. Our results indicate that air temperature observed at a variety of discrete spatial locations having different land cover, is highly correlated with MODIS LST collected at 1 km grid spacing. Quadratic relationships between LST and air temperature, constrained by ground observations of “clear” sky conditions show less variability than relationships found under “mainly clear” and “mostly cloudy” sky conditions and the more cloud observed in the sky coincides with an decreasing y-intercept. Analysis of MODIS LST and its associated quality flags show a cold bias (<0 °C) in the assignment of the ≤ 3 K average LST error, indicating MODIS LST has a maximum average error of ≤ 2 K over a warm surface (>0 °C). Our analysis of two sites showed that unidentified clouds in MODIS LST are between 13 % and 17 %, a result that agrees well with previous studies. Analysis of

daytime values is important because many processes are dependent on daylight and maximum temperature. We showed that the daytime “clear” sky LST to T_{air} relationship observed for the good quality confirmed cloud free sky MODIS LST quality flag can be used to discriminate cloud contaminated grid cells beyond the standard MODIS cloud mask.

Chapter Three: Estimating Temperature Fields from MODIS Land Surface Temperature and Air Temperature Observations in a Sub-Arctic Alpine Environment

Spatially continuous satellite infrared temperature measurements are essential for understanding the consequences and drivers of change, at local and regional scales, especially in northern and alpine environments dominated by a complex cryosphere where *in situ* observations are scarce. We described two methods for producing daily temperature fields using MODIS “clear-sky” day-time Land Surface Temperatures (LST). The Interpolated Curve Mean Daily Surface Temperature (ICM) method, interpolates single daytime Terra LST values to daily means using the coincident diurnal air temperature curves. The second method calculated daily mean LST from daily maximum and minimum LST (MMM) values from MODIS Aqua and Terra. The ICM and MMM models were compared to daily mean air temperatures recorded between April and October at seven locations in southwest Yukon, Canada, covering characteristic alpine land cover types (tundra, barren, glacier) at elevations between 1408 m and 2319 m. Both methods for producing mean daily surface temperatures have advantages and disadvantages. ICM signals are strongly correlated with air temperature

($R^2 = 0.72$ to 0.86), but have relatively large variability (RMSE = 4.09 to 4.90 K), while MMM values had a stronger correlation to air temperature ($R^2 = 0.90$) and smaller variability (RMSE = 2.67 K). Lastly, when the 8-day LST averages were compared to air temperature, the aggregate from the MMM method had a high correlation ($R^2 = 0.84$) with less variability (RMSE = 1.54 K). The trend was less steep and the y-intercept increased by 1.6 °C compared to the daily correlations. This effect is likely a consequence of LST temperature averages being differentially affected by cloud cover over warm and cold surfaces. We conclude that satellite infrared skin temperature (e.g., MODIS LST), which is often aggregated into multi-day composites to mitigate data reductions caused by cloud cover, changes in its relationship to air temperature depending on the period of aggregation.

Chapter Four: Night-Time Cloud Cover over Snow Covered Mountainous Terrain Produces an Inherent Cold Bias in MODIS LST when compared to Average Air Temperature

We compared monthly average temperatures from two independent downscaled temperature products to MODIS Land Surface Temperature (LST) and air temperature at nine meteorological stations, situated above tree-line, for a full range of snow cover fractions, for the southwest Yukon between May and August 2008. We found that both downscaled products generally agreed with LST for the low elevation, snow-free, vegetation classes. However a systematic cold bias in average LST was found for snow fractions greater than approximately 40%, and this bias increased in magnitude as snow

cover increased (downscaled temperatures are 5-7 °C warmer than average LST for snow fractions of >90%), and was largely independent of the number of measurements of LST within a month. Maximum LST was similar to average air temperatures for high snow fractions and was warmer for small snow fractions, but minimum LST was colder by 10 °C or more for all snow fractions. The average of maximum and minimum LST produced a cold bias, compared to air temperature, for high snow cover fractions. In contrast, a weak warm bias in average LST occurred for small snow fractions over non-forested land covers classes. Air temperature measured at nine meteorological monitoring stations located between elevations of 1408 – 2690 m, on Barren, Sparsely Vegetated or Permanent Snow and Ice land covers, confirmed the cold bias results from incorporating minimum LST in monthly averages. Furthermore the average LST is warmer than air temperature by 1-3 °C for the snow fractions < 10 %, but this finding is not broadly supported by the comparison to downscaled temperature products. Downscaled temperature fields show physically real differences to average LST in summer indicating these data streams could be used collaboratively to answer questions related to snow cover change and climate.

Chapter Five: Phenology and species determine growing season albedo increase at the altitudinal limit of shrub growth in the sub-Arctic

Arctic warming has resulted in both reduced snow cover and increased shrub growth, both of which have been associated with strengthening of feedback processes related to sensible heat flux, ground heat flux and biogeochemical cycling. Using field

measurements, we show that two common Arctic shrub species (*Betula glandulosa* and *Salix pulchra*), responsible for shrub encroachment in tundra, differed markedly in albedo and that albedo of both species increased as growing season progressed when measured at their altitudinal limit. Contrary to the generally accepted view of shrub covered areas having low albedo, full-canopy prostrate *B. glandulosa* had almost the highest albedo of all tundra surfaces measured during growing season peak.

Furthermore, most vegetation cover types showed increased albedo during the growing season with shrub canopy growth, and these dynamics are often not considered in energy balance analyses. Using field measurements, the ensemble summer increase in tundra albedo counteracted the effect of earlier spring snowmelt on surface energy balance by approximately 40%. Future efforts to calculate energy budgets and a sensible heating feedback in the Arctic will require more detailed information about the relative abundance of different ground cover types, particularly shrub species and their respective growth forms and phenology.

Chapter Six: Spring snow cover decline in altitudinal tundra provides a minimal contribution to Arctic temperature amplification

Both General Circulation Models and re-analysis studies indicate that Arctic amplification is caused mostly by latitudinal heat transport, and that local snow cover albedo feedback plays a limited role, but both approaches suffer limitations which add uncertainty into these results to the point that a firm understanding has still not been achieved. We used differential snow melt rates found over an ~5,000 m elevational

gradient found in the southwest Yukon between 2000 and 2008, to measure the relative effect of local heating caused by spring snow cover decline. To do this we utilised MODIS satellite measurements (Land Surface Temperature, snow cover and cloud cover), downscaled climatology, and meteorological measurements. We show for an $\sim 35,000 \text{ km}^2$ portion of the southwest Yukon the magnitude and rate of temperature change is nearly identical for Icefield, Conifer forest and Tundra, between 2000 and 2008, while Tundra snow cover decreased by 35 – 50%. Cloud cover, however does play an important role in modulating surface temperature and snow extent. Although we found evidence for a snow cover feedback ($< 6\%$ contribution in a monthly average which is the equivalent of $< 0.091 \text{ W m}^{-2}$ per decade over the 2000 to 2008 study period), we showed that the strength is insufficient to influence the monthly average temperature variation, leading us to conclude that snow cover and temperature change in southwest Yukon tundra is largely the result of external forcing consistent with latitudinal heat transport.

Conclusions and Future Work

The SAF to local climate in altitudinal tundra is small in comparison to the temperature fluctuations that are superimposed upon the Kluane region. This suggests that the snow cover loss between 2000 and 2008 has been primarily related to external factors, such as latitudinal heat transport, rather than a self-sustaining feedback. By extension, the feedback that has been hypothesised to be related to the increase in woody deciduous shrub cover will also be small because the albedo change related to

this phenomenon is much less than that related to snow cover decrease. Further, we also conclude that the assumption of albedo decrease caused by increasing woody deciduous shrub cover that fails to consider growing interspecific differences or growing season albedo dynamics is too simplistic for accurate feedback estimates.

The influence of temporal and spatial scale on the detection and attribution of ecological and atmospheric processes is of fundamental importance. Temporally matching observation to measurement provided a means to identify cloud contamination in LST data that would have been difficult to detect in aggregated data. The aggregation of LST measurements introduced bias depending on the amount of daytime (maximum) and night time (minimum) measurements, which were both modified by the amount of snow cover. Fractional snow cover, for example, can be used in such a way as to circumvent the limitations of spatial scale. The aggregation of temporal scale does not have the same ability. Sensitivity analysis of the magnitude of the effect of processes in relation to their duration must be conducted before analysis, otherwise a risk that real events can be smoothed to the point of where they are indistinguishable from background. In this respect the findings from chapters five and six are similar in that close enough attention has not been paid to temporal scale by previous studies.

The trend analysed in Chapter six was only nine years, which is not long enough to determine larger scale mechanisms working in the climate system. Climate normals are typically calculated as the 30-year average; however, if the new climate monitoring systems are becoming satellite-based, how will the ever-changing technology affect our ability to monitor change by constantly changing the measures that are being composited for time series analysis? For example the MODIS sensor on board the Terra

satellite was launched in 1999, with an expected mission lifespan of six years. As of this writing in June 2015 the satellite is still in orbit and is producing a live data stream. Continuity of this data stream will be necessary if we are to conduct objective, long-term analyses of the changing Arctic climate.

During the completion of this thesis an analogue to Arctic amplification was identified as Elevational Dependent Warming (EDW) in mountain regions (Pepin et al., 2015). This amplification of warming with elevation is poorly understood, especially in the attribution of the causal mechanisms such as the snow albedo feedback. The southwest Yukon will provide an ideal location to continue the analysis of EDW due to its relatively large area above 5,000 m. These northern mountains, which are located in the Arctic, display a large amount of alpine area. This should serve as a useful laboratory for global change studies, especially in terms of landscape resilience. Clarke et al. (2015) showed that most of the glaciers in western Canada will disappear this century, with a refugium in southwest British Columbia. The refugium will likely extend to the St Elias Mountains due to its high elevation and large precipitation input, producing healthy glacier mass balances.

During the course of this thesis an array of meteorological stations was established in an 8 km² alpine valley east of the southern portion of Kluane Lake. Field measurements in high enough spatial and temporal resolution are currently being made that will provide, in collaboration with satellite measurements, a field-based quantification of snow cover feedbacks. Other feedbacks are very important in tundra, especially tundra that overlays permafrost. This field site will provide a venue for the

investigation of questions related to ground heat fluxes, atmospheric heat fluxes, and landscape ecology.

Some aspects of the feedback processes are still poorly understood and likely require modelling to provide testable hypotheses. Modelling is fundamentally a hypotheses generation machine, and will provide future research goals that are presently unknown, or poorly conceptualised. For example, the effect of snow metamorphosis on albedo, and thus its contribution to climate feedback, remains unclear. Although there are studies looking at this topic (e.g., Fletcher et al., 2012) the merging of field measurements and satellite imagery will provide value added products that will be used to solve questions identified from modelling studies.

The integrated analysis presented here is leading to new insights into the primary forces driving climate change in this region. This was possible because of the interdisciplinary nature and unified techniques of investigation on what are usually separate fields of research related to glaciology, tundra ecology and forestry. The conclusion is that interdisciplinary research yields results that single disciplines are unable to provide.

References

- Ackerman, S.A., Strabala, K.I., Menzel, W.P., Frey, R.A., Moeller, C.C., & Gumley, L.E. (1998). Discriminating clear sky from clouds with MODIS. *Journal of Geophysical Research*, **103**, 32141- 32157.
- Clarke, G.K.C., Jarosch, A.H., Anslow, F.S., Radić, V., & Menounos, B. (2015). Projected deglaciation of western Canada in the twenty-first century. *Nature Geoscience*, **8**, 372-377.
- Fletcher, C.G., Zhao, H., Kushner, P.J., & Fernandes, R. (2012). Using models and satellite observations to evaluate the strength of snow albedo feedback. *Journal of Geophysical Research*, **17**, D11117, doi:10.1029/2012JD017724.
- Graversen, R., Mauritsen, T., Tjernström, M., Källén, E., & Svensson, G. (2008). Vertical structure of recent Arctic warming. *Nature*, 451, 53-56.
- Intergovernmental Panel on Climate Change (IPCC) (2013). Fifth Assessment Report. In: Climate Change 2013 – Working Group 1: The Physical Science Basis (eds Stocker TF, Qin D, Plattner G-K, Tignor M, Allen SK, Boschung J, Nauels A, Xia Y, Bex V, Midgley PM), pp.130-194; 1257-1258. Cambridge University Press, Cambridge, UK.
- Overland, J., Hanna, E., Hanssen-Bauer, I., Kim, S.-J., Walsh, J., Wang, M., & Bhatt, U.S. (2014). Arctic Report Card 2014 – Air Temperature.
www.Arctic.noaa.gov/reportcard/
- Pepin, N., Bradely R.S., Diaz, H.F., Baraer, M., Caceres, E.B., Forsythe, N., Fowler, H.,

- Greenwood, G., Hasmi, M.Z., Liu, X.D., Miller, J., Ning, L., Ohmura, A., Palazzi, E., Rangwala, I., Schoener, W., Severskiy, I., Shahgedanova, M., Williamson, S.N., & Yang, D.Q. (2015). Elevation-Dependent Warming in Mountain Regions of the World. *Nature Climate Change*, **5**, 424-430.
- Screen, J.A., Deser, C., & Simmonds, I. (2012). Local and remote controls on observed Arctic warming. *Geophysical Research Letters*, **39**, L10709, doi:10.1029/2012GL051598.
- Serreze, M., & R. Barry. (2011). Processes and impacts of Arctic amplification: A research synthesis. *Global and Planetary Change*, **77**, 85-96.
- Westermann, S., Langer, M., & Boike, J. (2012). Systematic bias of average winter-time land surface temperatures inferred from MODIS at a site on Svalbard, Norway. *Remote Sensing of Environment*, **118**, 162-167.

Inclusive Bibliography

ACIA (Arctic Climate Impact Assessment) Report. (2005). Impacts of a warming Arctic.

UK: Cambridge University Press 146 pp.

AMAP (Arctic Monitoring and Assessment Programme). (2012). SWIPA overview

report. In: Arctic Climate Issues 2011: Changes in Arctic Snow, Water, Ice and

Permafrost (eds. Shearer, R., Wrona, F., Klint, M., Larsen, H., Skovgaard, O.,

Mahonen, O., Jensson, H., Dovle, P., Tsaturov, Y., Lundeberg, T., Armstrong, T.,

Solbakken, J.-I., pp. 30-40. Oslo, Norway.

Ackerman, S. A., Strabala, K. I., Menzel, W. P., Frey, R. A., Moeller, C. C., & Gumley,

L. E. (1998). Discriminating clear sky from clouds with MODIS. *Journal of*

Geophysical Research, **103**, 32141-32157.

Ackerman, S. A., Holz, R. E., Frey, R., Eloranta, E. W., Maddux, B. C., & McGill, M.

(2008). Cloud detection with MODIS. Part II: Validation. *Journal of Atmosphere*

and Oceanic Technology, **25**, 1073-1086.

Andresen, C.G., & Lougheed, V.L. (2015). Disappearing Arctic tundra ponds: Fine-

scale analysis of surface hydrology in drained thaw lake basins over a 65 year period

(1948-2013). *Journal of Geophysical Research Biogeosciences*, **120**, 466-479.

Armstrong, R. L. & Brun, E. (editors). (2008). Snow and Climate. Cambridge

University Press, Cambridge, U.K.

Asner, P. (1998). Biophysical and biochemical sources of variability in canopy

reflectance. *Remote Sensing of Environment*, **64**, 234-253.

Bartlett, M. G., Chapman, D. S., & Harris, R. N. (2006). A decade of ground-air

- temperature tracking at Emigrant Pass observatory, Utah. *Journal of Climate*, **19**, 3722-3731.
- Benali, A., Carvalho, A.C., Nunes, J.P., Carvalhais, N., & Santos, A. (2012). Estimating air surface temperature in Portugal using MODIS LST data. *Remote Sensing of Environment*, **124**, 108–121.
- Beringer, J., Chapin F. S., Thompson C. C., & McGuire, A. D. (2005). Surface energy along a tundra-forest transition and feedbacks to climate. *Agricultural and Forest Meteorology*, **131**, 143-161.
- Berthier, E., Schiefer, E., Clarke, G. K. C., Menounos, B., & Remy, F. (2010). Contribution of Alaskan glaciers to sea-level rise derived from satellite imagery. *Nature Geoscience*, **3**, doi:10.1038/NGEO737.
- Bhatt, U.S., Walker, D.A., Raynolds, M.K., Bieniek, P.A., Epstein, H.E., Comiso, J.C., Pinzon, J.E., Tucker, C.J., & Polyakov, I.V. (2013). Recent declines in warming and vegetation greening trends over pan-Arctic tundra. *Remote Sensing*, **5**, 4229–4254.
- Bird, R.E., & Hulstrom, R.L. (1991). *A Simplified Clear Sky model for Direct and Diffuse Insolation on Horizontal Surfaces* by R.E. Bird and R.L Hulstrom, SERI Technical Report SERI/TR-642-761. Solar Energy Research Institute, Golden, CO.
- Blackmon, M. L. (1976). Climatological spectral study of 500 Mb geopotential height of northern hemisphere. *Journal of Atmospheric Science*, **33**, 1607-1623.
- Blanken, P.D., & Rouse, W.R. (1994). The role of Willow-Birch Forest in the Surface Energy Balance at Arctic Treeline. *Arctic and Alpine Research*, **26**, 403-411.

- Blok, D., Schaepman-Strub, G., Bartholomeus, H., Heijmans, M. M., Maximov, T. C., & Berendse, F. (2011). The response of Arctic vegetation to the summer climate: relation between shrub cover, NDVI, surface albedo and temperature. *Environmental Research Letters*, **6**, 035502, doi:10.1088/1748-9326/6/3/035502.
- Bonan, G. B. (2008). Forests and Climate Change: Forcings, Feedbacks, and the Climate Benefits of Forests. *Science*, **320**, 1444-1449.
- Bony, S., Colman, R., Kattsov, V. M., Allan, R. P., Bretherton, C. S., Dufresne, J. L., Hall, A., Hallegatte, S., Holland, M. M., Ingram, W., Randall, D. A., Soden, B. J., Tselioudis, G., & Webb, M. J. (2006). How well do we understand and evaluate climate change feedback processes? *Journal of Climate*, **19**, 3445-3482.
- Bras, R.L. *Hydrology*. (1990). Addison-Wesley, Reading, MA.
- Bret-Harte, M. S., Shaver, G. R., Zoerner, J. P., Johnstone, J. F., Wagner, J. L., Chavez, A. S., ... & Laundre, J. A. (2001). Developmental plasticity allows *Betula nana* to dominate tundra subjected to an altered environment. *Ecology*, **82**, 18-32.
- Brown, R., Derksen, C., & Wang, L. (2010). A multi-dataset analysis of variability and change in Arctic spring snow cover extent. *Journal of Geophysical Research*, **115**, D16111, doi:10.1029/2010JD013975.
- Brown, R., Derksen, C., & Wang, L. (2010). A multi-dataset analysis of variability and change in Arctic spring snow cover extent. *Journal of Geophysical Research*, **115**, D16111, doi:10.1029/2010JD013975.
- Chapin, F. S., Sturm, M., Serreze, M. C., McFadden, J. P., Key, J. R., Lloyd, A. H., McGuire, A. D., Rupp, T. S., Lynch, A. H., Schimel, J. P., Beringer, J., Chapman, W.

- L., Epstein, H. E., Euskirchen, E. S., Hinzman, L. D., Jia, G., Ping, C.-L., Tape, K. D., Thompson, C. D. C., Walker, D. A., & Welker, J. M. (2005). Role of land-surface changes in Arctic summer warming. *Science*, **310**, 657-660.
- Clarke, G.K.C., Jarosch, A.H., Anslow, F.S., Radić, V., & Menounos, B. (2015). Projected deglaciation of western Canada in the twenty-first century. *Nature Geoscience*, **8**, 372-377.
- Cohen, J., Pulliainen, J., Ménard, C.B., *et al.* (2013). Effects of reindeer grazing on snowmelt, albedo and energy balance based on satellite data analyses. *Remote Sensing of Environment*, **135**, 107-117.
- Comiso J. C. (2003). Warming trends in the Arctic from clear sky satellite observations. *Journal of Climate*, **16**, 3498-3510.
- Cook, B.I., Smerdon, J.E., Seager, R., & Coats, S. (2014). Global warming and 21st century drying. *Climate Dynamics*, **43**, 2607-2627.
- Crosson, W.L., Al-Hamdan, M.Z., Hemmings, S.N.J., & Wade, G.M. (2012). A daily merged MODIS Aqua-Terra land surface temperature data set for the conterminous United States. *Remote Sensing of Environment*, **119**, 315–324.
- Curry, J. A., Rossow, W. B., Randall, D., & Schramm, J. L. (1996). Overview of Arctic cloud and radiation characteristics. *Journal of Climate*, **9**, 1731-1764.
- Dai, A., Fyfe, J.C., Xie, S.-P., & Dai, X. (2015). Decadal modulation of global surface temperature by internal climate variability. *Nature Climate Change*, doi: 10.1038/NCLIMATE2605.

- Daly, C., Neilson, R. P., & Phillips, D. L. (1994). A statistical-topographical model for mapping climatological precipitation over mountainous terrain. *Journal of Applied Meteorology*, **33**, 140-158.
- Danby, R. K., & Hik, D. S. (2007). Variability, contingency and rapid change in recent subArctic alpine tree line dynamics. *Journal of Ecology*, **95**, 352-363.
- Danby, R.K., Koh, S., Hik, D.S., & Price, L.W. (2011). Four decades of plant community change in the alpine tundra of southwest Yukon, Canada. *AMBIO* **40**, 660-671.
- Déry, S.J., & Brown, R.D. (2007). Recent Northern Hemisphere snow cover extent trends and implications for the snow-cover feedback. *Geophysical Research Letters*, **34**, L22504, doi:10.1029/2007GL031474.
- Dessler, A. E., Zhang, Z., & Yang, P. (2008). Water-vapor climate feedback inferred from climate fluctuations, 2003-2008. *Geophysical Research Letters*, **35**, doi: 10.1029/2008GL035333.
- Dwyer, J., & Schmidt, G. (2006). The MODIS reprojection tool. In J. J. Qu, W. Gao, M. Kaftos, R. E. Murphy, & V. V. Salmonson, Eds., *Earth science satellite remote sensing*, Berlin Heidelberg: Springer Berlin Heidelberg, 162-177.
- Dye, D.G., & Tucker, C.J. (2003). Seasonality and trends in snow-cover, vegetation index, and temperature in northern Eurasia. *Geophysical Research Letters*, **30**, 1405, doi:10.1029/2002GL016384.

- Elmendorf, S. C., Henry, G. H., Hollister, R. D., Björk, R. G., Boulanger-Lapointe, N., Cooper, E. J., ... & Wipf, S. (2012). Plot-scale evidence of tundra vegetation change and links to recent summer warming. *Nature Climate Change*, **2**, 453-457.
- Epstein, H.E., Calef, M.P., Walker, M.D., Chapin, F.S., & Starfield, A.M. (2004). Detecting changes in Arctic tundra plant communities in response to warming over decadal time scales. *Global Change Biology*, **10**, 1325-1334.
- Eugster, W., Rouse, W. R., Pielke, R. A., McFadden, J. P., Baldocchi, D. D., Kittel, T. G. F., Chapin, F. S., Liston, G. E., Vidale, P. L., Vaganov, E., & Chambers, S. (2000). Land-atmosphere energy exchange in Arctic tundra and boreal forest: available data and feedbacks to climate. *Global Change Biology*, **6**, 84-115.
- Euskirchen, E. S., McGuire, A. D., Kicklighter, D. W., Zhuang, Q., Clein, J. S., Dargaville, R. J., Dye, D. G., Kimball, J. S., McDonald, K. C., Melillo, J. M., Romanovsky, V. E., & Smith, N. V. (2006). Importance of recent shifts in soil thermal dynamics on growing season length, productivity, and carbon sequestration in terrestrial high-latitude ecosystems. *Global Change Biology*, **12**, 731-750.
- Euskirchen, E. S., McGuire, A. D., Chapin, F. S., Yi, S., & Thompson, C. C. (2009). Changes in vegetation in northern Alaska under scenarios of climate change, 2003-2100: implications for climate feedbacks. *Ecological Applications*, **19**, 1022-1043.
- Flanner, M. G., Shell, K. M., Barlage, M., Pervich, D. K., & Tschudi, M. A. (2011). Radiative forcing and albedo feedback from the Northern Hemisphere cryosphere between 1979 and 2008. *Nature Geoscience*, **4**, 151-155.
- Fleming, M. D., Chapin, F. S., Cramer, W., Huffords, G. L., & Serreze, M. C. (2000). Geographic patterns and dynamics of Alaskan climate interpolated from a sparse

- station record. *Global Change Biology*, **6**, 49-58.
- Fletcher, C.G., Zhao, H., Kushner, P.J., & Fernandes, R. (2012). Using models and satellite observations to evaluate the strength of snow albedo feedback. *Journal of Geophysical Research*, **17**, D11117, doi:10.1029/2012JD017724.
- Frost, G.V., & Epstein, H.E. (2014). Tall shrub expansion in Siberian tundra ecotones since the 1960s. *Global Change Biology*, **20**, 1264-1277.
- Gamon, J.A., Huemmrich, K.F., Stone, R.S., & Tweedie, C. (2013). Spatial and Temporal Variation in Primary Productivity (NDVI) of Coastal Alaskan Tundra: Decreased Vegetation Growth following Earlier Snowmelt. *Remote Sensing of Environment*, **129**, 144-153.
- Garbutt, R. (2008). Yukon Forest Health Report 2007. Government of Yukon, Energy, Mines and Resources, Forest Management Branch. ISSN: 1708-9360.
- Goodison, B. E. (1981). Compatibility of Canadian snowfall and snow cover data. *Water Resources Research*, **17**, 893-900.
- Grace, J., Berninger, F., & Nagy, L. (2002). Impacts of climate change on the tree line. *Annals of Botany*, **90**, 537-544.
- Graversen, R., Mauritsen, T., Tjernström, M., Källén, E., & Svensson, G. (2008). Vertical structure of recent Arctic warming. *Nature*, **451**, 53-56.
- Grenfell, T. C., & Perovich, D. K. (2004). Seasonal and spatial evolution of albedo in a snow-ice-land-ocean environment. *Journal of Geophysical Research*, **109**, C01001, doi:10.1029/2003JC001866.

- Groisman, P. Y., Karl, T. R., & Knight, R. W. (1994). Observed impact of snow cover on the heat balance and the rise of continental spring temperatures. *Science*, **263**, 198-200.
- Hall, D. K., Box, J. E., Casey, K. A., Hook, S. J., Shuman, C. A., & Steffen, K. (2008). Comparison of satellite-derived and in-situ observations of ice and snow surface temperatures over Greenland. *Remote Sensing of Environment*, **112**, 3739-3749.
- Hall, D. K., & Riggs, G. A. (2007). Accuracy assessment of the MODIS snow products. *Hydrological Processes*, **21**, 1534-1547.
- Hall, D. K., Riggs, G. A., Salomsonson, V. V., DiGirolamo, N. E., & Bayd, K. J. (2002). MODIS snow-cover products. *Remote Sensing of Environment*, **83**, 181-194.
- Hallinger, M., Manthey, M., & Wilmking, M. (2010). Establishing a missing link: warm summers and winter snow cover promote shrub expansion into alpine tundra in Scandinavia. *New Phytologist*, **186**, 890-899.
- Harding, R.J., & Lloyd, C.R. (1998). Fluxes of Water and Energy from Three High Latitude Tundra Sites in Svalbard. *Nordic Hydrology*, **29**, 267-284.
- Harrison, E. F., Minnis, P., Barkstrom, B. R., Ramanathan, V., Cess, R. D. & Gibson, G. G. (1990). Seasonal variation of cloud radiative forcing derived from the Earth Radiation Budget Experiment. *Journal of Geophysical Research*, **95**, 18687-18703.
- Heskel, M., Greaves, H., Kornfeld, A., *et al.* (2013). Differential physiological responses to environmental change promote woody shrub expansion. *Ecology and Evolution*, **3**, 1149-1162.

- Holdridge, L.R. (1967). *Life Zone Ecology*, Tropical Science Center: San Jose, Costa Rica.
- Holland, M. M., & Bitz, C. M. (2003). Polar amplification of climate change in coupled models. *Climate Dynamics*, **21**, 221-232.
- Houghton, J. T., Ding, Y., Griggs, D. J., Noguer, M., van der Linden, P. J., Dai, X., Maskell, K., & Johnson, C. A., Eds., 2001: *Climate Change 2001: The Scientific Basis*. Cambridge University Press, 944 pp.
- Intergovernmental Panel on Climate Change (IPCC) (2013). Fifth Assessment Report. In: *Climate Change 2013 – Working Group 1: The Physical Science Basis* (eds Stocker TF, Qin D, Plattner G-K, Tignor M, Allen SK, Boschung J, Nauels A, Xia Y, Bex V, Midgley PM), pp.130-194; 1257-1258. Cambridge University Press, Cambridge, UK.
- Jarosch, A. H., Anslow, F. S., & Clarke, G. K. C. (2012). High-resolution precipitation and temperature downscaling for glacier models. *Climate Dynamics*, **38**, doi: 10.1007/s00382-010-0949-1.
- Jin, M. (2000). Interpolation of surface radiation temperature measured from polar orbiting satellites to a diurnal cycle. 2. Cloudy pixel treatment. *Journal of Geophysical Research*, **105**, 4061–4076.
- Jin, M., & Dickinson, R.E. (1999). Interpolation of surface radiative temperature measured from polar orbiting satellite to a diurnal cycle. Part 1: Without clouds. *Journal of Geophysical Research*, **104**, 2105–2116.
- Jin, M., & Dickinson, R. E. (2000). A generalized algorithm for retrieving cloudy sky skin temperature from satellite thermal infrared radiances. *Journal of Geophysical*

Research - Atmosphere, **105**, 27037-27047.

- Jin, M., & Dickinson, R. E. (2010). Land surface skin temperature climatology: benefitting from the strengths of satellite observations, *Environmental Research Letters*, **5**, doi:10.1088/1748-9326/4/044004.
- Jin, M., & Treadon, R.E. (2003). Correcting orbit drift effects of AVHRR on Skin Temperature Measurements. *International Journal of Remote Sensing*, **24**, 4543–4558.
- Jones, P. D., & Moberg, A. (2003). Hemispherical and large scale surface air temperature variations: an extensive revision and an update to 2001. *Journal of Climate*, **16**, 206-223.
- Karl, T.R., Arguez, A., Huang, B., Lawrimore, J.H., McMahon, J.R., Menne, M.J., Peterson, T.C., Vose, R.S., & Zhand, H.-M. (2015). Possible artifacts of data biases in the recent global surface warming hiatus. *Science*, **348**, 1469-1472.
- Karlsen, S. R., & Elvebakk, A. (2003). A method using indicator plants to map local climatic variation in the Kagerlussuaq/Scoresby Sund area, East Greenland. *Journal of Biogeography*, **30**, 1469-1491.
- Körner, C. (2003). *Alpine plant life: functional plant ecology of high mountain ecosystems; with 47 tables*. Springer Science & Business Media.
- Kothawale, D., Munot, A. & Kumar, K. K. (2010). Surface air temperature variability over India during 1901-2007, and its association with ENSO. *Climate Research*, **42**, 89-104.

- Lafleur, P.M., Rouse, W.R., & Hardill, S.G. (1987). Components of the surface radiation balance of subArctic wetlands terrain units during the snow-free season. *Arctic and Alpine Research*, **19**, 53-63.
- Lafleur, P.M., Rouse, W.R., & Carlson, D.W. (1992). Energy balance difference and the hydrologic impacts across the northern treeline. *International Journal of Climatology* **12**, 193-203.
- Langen, P. L., & Alexeev, V. A. (2004). Multiple equilibria and asymmetric climates in the CCM3 coupled to an oceanic mixed layer with thermodynamic sea ice. *Geophysical Research Letters*, **31**, doi: 10.1029/2003GL019039.
- Langer, M., Westermann, S., & Boike, J. (2010). Spatial and temporal variations of summer surface temperatures of wet polygonal tundra in Siberia – implications for MODIS LST base permafrost monitoring. *Remote Sensing of Environment*, **114**, 2059-2069.
- Lewis, M. C., & Callaghan, T. V. (1976). Tundra. *Vegetation and the Atmosphere*. Vol. 2. J. L. Monteith, Ed. Academic Press, 399-433.
- Liston, G. E. (1995). Local advection of momentum, heat, and moisture during the melt of patchy snow covers. *Journal of Applied Meteorology*, **34**, 1705-1715.
- Liston, G. E., & Sturm, M. (1998). A snow-transport model for complex terrain. *Journal of Glaciology*, **44**, 1705-1715.
- Liu, Y., Key, J. R., & Wang, X. (2008). The influence of changes in cloud cover on recent surface temperature trends in the Arctic. *Journal of Climate*, **21**, 705-715.

- Lugo, A.E., Brown, S.L., Dodson, R., Smith, T.S., & Shugart, H.H. (1999). The Holdridge life zone of the conterminous United States in relation to ecosystem mapping. *Journal of Biogeography*, **26**, 1025–1038.
- Manabe, S., & Bryan, K. (1969). Climate calculations with a combined ocean-atmosphere model. *Journal of Atmospheric Science*, **26**, 786-789.
- Manney, G.L., Kruger, K., Sabutis, J.L., Sena, S.A., & Pawson, S. (2005). The remarkable 2003-2004 winter and other recent warm winters in the Arctic stratosphere since the late 1990s. *Journal of Geophysical Research – Atmospheres*, **110**, doi:10.1029/2004JD005367.
- Mantua, N.J., & Hare, S.R. (2002). The Pacific Decadal Oscillation. *Journal of Oceanography*, **58**, 35-44.
- Marsh, P. 1991. Water flux in melting snow covers. In: *Advances in Porous Media* (ed. Corapcioglu MY), Vol. 1, pp. 61-124. Elsevier, Amsterdam.
- McGuire, A. D., Chapin F. S., Walsh, J. E., & Wirth, C. (2006). Integrated Regional Changes in Arctic Climate Feedbacks: Implications for the Global Climate System. *Annual Review of Environment and Resources*, **31**, 61-91.
- Mesinger, F., DiMego, G., Kalnay, E., Mitchell, K., Shafran, P.C., Ebisuzaki, W., Jović, D., Woollen, J., Rogers, E., Berery, E.H., Ek, M.B., Fan, Y., Grumine, R., Higgins, W., Li, H., Lin, Y., Manikin, G., Parrish, D., & Shi, W. (2006). North American Regional Reanalysis. *Bulletin of the American Meteorological Society*, **87**, 343-360.
- Moore, G. W. K, Holdsworth, G., & Alverson, K. (2002). Climate change in the North Pacific region over the past three centuries. *Nature*, **420**, 401-403.

- Murphy, J., Sexton, D., Barnett, D., Jones, G., Webb, M., Collins, M., & Stainforth, D. (2004). Quantification of modelling uncertainties in a large ensemble of climate change simulations. *Nature*, **430**, 768-772.
- National Research Council – of the National Academics (NRC). (2003). Understanding Climate Change Feedbacks. National Academic Press, 152pp.
- Nishida, K., Nemani, R. R., Glassy, J. M., & Running, S. W. (2003). Development of an Evapotranspiration Index From Aqua/MODIS for Monitoring Surface Moisture Status. *IEEE Transactions Geoscience and Remote Sensing*, **41**, 493-501.
- Ohmura, A. 1981. Climate and Energy Balance of Arctic Tundra. Zürcher Geographische Schriften/ETH Zürich, Switzerland.
- Oke, T.R. (1987). *Boundary Layer Climates*. 2nd edn. Methuen, London.
- Overland, J. E., Turet, P., & Oort, A. H. (1996). Regional variation of moist static energy flux into the Arctic. *Journal of Climate*, **9**, 54-65.
- Overland, J., Hanna, E., Hanssen-Bauer, I., Kim, S.-J., Walsh, J., Wang, M., & Bhatt, U. S. (2014). Arctic Report Card 2014 – Air Temperature.
www.Arctic.noaa.gov/reportcard/
- Painter, T. H., Rittger, K., McKenzie, C., Slaughter, P., Davis, R.E., & Dozier, J. (2009). Retrieval of subpixel snow covered area, grain size, and albedo from MODIS. *Remote Sensing of Environment*, **113**, 868-879.
- Pearson, R. G., Phillips, S. J., Loranty, M. M., Beck, P. S., Damoulas, T., Knight, S. J., & Goetz, S. J. (2013). Shifts in Arctic vegetation and associated feedbacks under climate change. *Nature Climate Change*, **3**, 673-677.

- Pepin, N., Bradely R. S., Diaz, H. F., Baraer, M., Caceres, E. B., Forsythe, N., Fowler, H., Greenwood, G., Hasmi, M. Z., Liu, X. D., Miller, J., Ning, L., Ohmura, A., Palazzi, E., Rangwala, I., Schoener, W., Severskiy, I., Shahgedanova, M., Williamson, S. N., & Yang, D. Q. (2015). Elevation-Dependent Warming in Mountain Regions of the World. *Nature Climate Change*, **5**, 424-430.
- Pinheiro, A.C.T., Privette, J.L., Mahoney, R., & Tucker, C.J. (2004). Directional effects in a daily AVHRR land surface temperature dataset over Africa. *IEEE Transactions on Geoscience and Remote Sensing*, **42**, 1941–1954.
- Platnick, S., King, M. D., Ackerman, S. A., Menzel, W. P., Baum, B. A., Riedi, J. C., & Frey, R. A. (2003). The MODIS Cloud Products: Algorithms and Examples From Terra. *IEEE Transactions Geoscience and Remote Sensing*, **41**, 459-473.
- Polyakov, I. D., Alekseev, G. V., Bekryaev, R. V., Bhatt, U., Colony, R., Johnson, M. A., Karklin, V. P., Makshatas, A. P., Walsh, D., & Yulin, A. V. (2002). Observationally based assessment of polar amplification of global warming. *Geophysical Research Letters*, **29**, doi:10.1029/2001GL011111.
- Post, E., Forchhammer, M.C., Bret-Harte, M.S., Callaghan, T.V., Christensen, T.R., Elberling, B., Fox, A.D., Glig, O., Hik, D.S., Hoye, T.T., *et al.* (2009). Ecological dynamics across the Arctic associated with recent climate change. *Science*, **325**, 1355–1358. doi:10.1126/science.1173113.
- Prudhomme, C., Reynard, N., & Crooks, S. (2002). Downscaling of global climate models for flood frequency analysis: Where are we now? *Hydrological Processes*, **16**, 1137–1150.

- Pu, Z., Xu, L., & Salomonson, V. (2007). MODIS/Terra observed seasonal variations of snow cover over the Tibetan Plateau. *Geophysical Research Letters*, **34**, L06706, doi:10.1029/2007GL029262.
- R Development Core Team. (2008). R: A language and environment for statistical computing. R foundation for Statistical Computing: Vienna, Austria. ISBN 3-900051-070-0. Available online: <http://www.R-project.org> (accessed on 30 October 2013).
- Raleigh, M. S., Rittger, K., Moore, C. E., Henn, B., Lutz, J. A., & Lundquist, J. D. (2013). Ground-based testing of MODIS fractional snow cover in subalpine meadows and forest of the Sierra Nevada. *Remote Sensing of Environment*, **128**, 44-57.
- Raynolds, M.K., Comiso, J.C., Walker, D.A., & Verbyla, D. (2008). Relationship between satellite-derived land surface temperatures, Arctic vegetation types, and NDVI. *Remote Sensing of Environment*, **112**, 1884–1894.
- Robeson, S. M. (1995). Resampling of network-induced variability in estimates of terrestrial air temperature change. *Climatic Change*, **29**, 213–229.
- Rouse, W. R. (2000). The energy and water balance of high latitude wetlands: controls and extrapolations. *Global Change Biology*, **6**, 59-68.
- Rouse, W. R., Carlson, D. W., & Weick, E. J. (1992). Impacts of summer warming on the energy balance of wet tundra. *Climate Change*, **22**, 305-326.
- Royer, A, & Poirier, S. (2010). Surface temperature spatial and temporal variations in North America from homogenized satellite SMMR-SSM/I microwave measurements and reanalysis for 1979-2008. *Journal of Geophysical Research*, **115**, D08110,

doi:10.1029/2009JD012760.

- Ryan, P.J., & Stolzenbach, K.D. (1972). *Engineering Aspects of Heat Disposal From Power Generation* (D.R.F. Harleman, ed.). R.M. Parson Laboratory for Water Resources and Hydrodynamics, Department of Civil Engineering, Massachusetts Institute of Technology, Cambridge, MA.
- Salomonson, V. V., & Appel, I. (2004). Estimating fractional snow cover from MODIS using the normalised difference snow index. *Remote Sensing of Environment*, **89**, 351-360.
- Screen, J., & Simmonds, I. (2010). The central role of diminishing sea ice in recent Arctic temperature amplification. *Nature*, **464**, 1334-1337.
- Screen, J.A., Deser, C., & Simmonds, I. (2012). Local and remote controls on observed Arctic warming. *Geophysical Research Letters*, **39**, L10709, doi:10.1029/2012GL051598.
- Screen, J.A. (2014). Arctic amplification decreases temperature variance in northern mid- to hi-latitudes. *Nature Climate Change*, **4**, 577-582.
- Sellers, W.D. (1965). *Physical Climatology*, University of Chicago Press: Chicago, IL, USA, p. 272.
- Serreze, M. C., & Francis, J. A. (2006). The Arctic amplification Debate. *Climate Change*, **76**, 241-264.
- Serreze, M. C., Barrett, A., Stroeve, D., Kindig, D., & Holland, M. (2009). The emergence of surface-based Arctic amplification, *Cryosphere*, **3**, 11-19.
- Serreze, M., & R. Barry. (2011). Processes and impacts of Arctic amplification: A

- research synthesis. *Global and Planetary Change*, **77**, 85-96.
- Shi, T., Clothiaux, E. E., Yu, B., Braverman, A. J., & Groff, D. N. (2007). Detection of daytime Arctic clouds using MISR and MODIS data. *Remote Sensing of Environment*, **107**, 172-184.
- Sims, D.A., & Gamon, J.A. (2003). Estimation of vegetation water content and photosynthetic tissue area from spectral reflectance: a comparison of indices based on liquid water and chlorophyll absorption. *Remote Sensing of Environment*, **84**, 526-537.
- Smirnov, V. V., & Moore, G. W. K. (1999). Spatial and temporal structure of atmospheric water vapor transport in the Mackenzie River basin. *Journal of Climate*, **12**, 681-696.
- Smith, L.C., Sheng, Y., MacDonald, G.M., & Hinzman, L.D. (2005). Disappearing arctic lakes. *Science*, **308**, 1429.
- Snow, Water, Ice, Permafrost in the Arctic (SWIPA) (2011) Accessed 22 April 2013, <http://amap.no/swipa>.
- Snyder, W.C., Wan, Z., Zhang, Y., & Feng, Y. Z. (1998). Classification-based emissivity for land surface temperature measurement from space. *International Journal of Remote Sensing*, **19**, 2753-2774.
- Snow, Water, Ice, Permafrost in the Arctic (SWIPA). (2011). Available online: <http://amap.no/swipa/> (accessed on 20 April 2013).
- Soden, B. J. & Held, I. M. (2006). An assessment of climate feedbacks in coupled

- ocean-atmosphere models. *Journal of Climate*, **19**, 3354-3360.
- Soliman, A., Duguay, C., Saunders, W., & Hachem, S. (2012). Pan-Arctic land surface temperature from MODIS and AASTR: Product development and intercomparison. *Remote Sensing*, **4**, 3833–3856.
- Stainforth, D. A., Aina, T., Christensen, C., Collins, M., Faull, N., Frame, D. J., Kettleborough, J. A., Knight, S., Martin, A., Murphy, J. M., Piani, D., Sexton, D., Smith, L. A., Spicer, R. A., Thorpe, A. J., & Allen, M. R. (2005). Uncertainty in predictions of the climate response to rising levels of greenhouse gases. *Nature*, **433**, 403-406.
- Sturm, M., Racine, C., & Tape, K. (2001). Climate change: increasing shrub abundance in the Arctic. *Nature*, **411**, 546-547.
- Sturm, M., McFadden, J. P., Liston, G. E., Chapin F. S., Racine, C. H., & Holmgren, J. (2001). Snow – Shrub Interactions in Arctic Tundra: A Hypothesis with Climactic Implications. *Journal of Climate*, **14**, 336-344.
- Sturm, M., Douglas, T., Racine, C., & Liston, G. E. (2005). Changing snow and shrub conditions affect albedo with global implications. *Journal of Geophysical Research*, **110**, doi: 10.1029/2005JG000013.
- Sun, J., Salvucci, G.D., & Entekhabi, D. (2012). Estimates of evapotranspiration from MODIS and AMSR-E land surface temperature and moisture over the Southern Great Plains. *Remote Sensing of Environment*, **127**, 44–59.

- Sweet S.K., Griffin, K.L., Steltzer, H., Gough, L., & Boelman, N.T. (2015). Greater deciduous shrub abundance extends tundra peak season and increases modeled net CO₂ uptake. *Global Change Biology*, **21**, 2394-2409.
- Tape, K., Sturm, M., & Racine, C. (2006). The evidence for shrub expansion in Northern Alaska and the Pan-Arctic. *Global Change Biology*, **12**, 686-702.
- Tape, K.D., Hallinger, M., Welker, J.M., & Ruess, R.W. (2012). Landscape heterogeneity of shrub expansion in Arctic Alaska. *Ecosystems*, **15**, 711-724.
- Thompson, C., Beringer, J., Chapin, F. S., & McGuire, A. D. (2004). Structural complexity and land-surface energy exchange along a gradient from Arctic tundra to boreal forest. *Journal of Vegetation Science*, **15**, 397-406.
- Trenberth, K.E. (1984). Some effects of finite sample size and persistence on meteorological statistics, II, Potential predictability. *Monthly Weather Review*, **112**, 2369–2379.
- Trenberth, K.E., & Hurrell, J.W. (1994). Decadal atmosphere-ocean variability in the Pacific. *Climate Dynamics*, **9**, 303–309.
- Van Loon, H., & Rogers, J. C. (1978). The seesaw in winter temperatures between Greenland and northern Europe. Part I: General description. *Monthly Weather Review*, **106**, 296-310.
- Vancutsem, C., Ceccato, P., Dinku, T., & Connor, S.J. (2010). Evaluation of MODIS land surface temperature data to estimate air temperature in different ecosystems over Africa. *Remote Sensing of Environment*, **114**, 449–465.
- Varvus, S. (2004). The impact of cloud feedbacks on Arctic climate under greenhouse

- gas forcing. *Journal of Climate*, **17**, 603-615.
- Vincent, L.A., & Mekis, E. (2006). Changes in daily and extreme temperature and precipitation indices for Canada over the twentieth century. *Atmosphere-Ocean*, **44**, 177-193.
- Walker, M. D., Wahren, C. H., Hollister, R. D., Henry, G. H., Ahlquist, L. E., Alatalo, J. M., ... & Wookey, P. A. (2006). Plant community responses to experimental warming across the tundra biome. *Proceedings of the National Academy of Sciences of the United States of America*, **103**, 1342-1346.
- Wan, Z., Zhang, Y. Zhang, Q. Li, Z. (2002). Validation of the land-surface temperature product retrieved from Terra Moderate Resolution Imaging Spectroradiometer data. *Remote Sensing of Environment*, **83**, 163-180.
- Wan, Z. (2008). New refinements and validation of MODIS land-surface temperature/emissivity products. *Remote Sensing of Environment*, **112**, 59-74.
- Wang, W., Liang, S., & Meyers, T. (2008). Validating MODIS land surface temperature products using long-term nighttime ground measurements. *Remote Sensing of Environment*, **112**, 623-635.
- Wang, X. & Key, J. R. (2003). Recent trends in Arctic surface, cloud, and radiation properties from space. *Science*, **299**, 1725-1728.
- Weller, G., & Holmgren, G. (1974). The Microclimate of the Arctic Tundra. *Journal of Applied Meteorology*, **13**, 854-862.

- Wenbin, Z., Aifeng, L., & Shaofeng, J. (2013). Estimation of daily maximum and minimum air temperature using MODIS land surface temperature products. *Remote Sensing of Environment*, **130**, 62–73.
- Westermann, S., Langer, M., & Boike, J. (2012). Systematic bias of average winter-time land surface temperatures inferred from MODIS at a site on Svalbard, Norway. *Remote Sensing of Environment*, **118**, 162-167.
- Winton, M. (2006). Amplified Arctic climate change: What does surface albedo feedback have to do with it? *Geophysical Research Letters*, **33**, L03701, doi:10.1029/2005GL025244.
- Williamson, S.N., Hik, D.S., Gamon, J.A., Kavanaugh, J.L., & Koh, S. (2013). Evaluating cloud contamination of clear-sky MODIS Terra daytime Land Surface Temperatures using ground-based meteorology station observations. *Journal of Climate*, **26**, 1551–1560.
- Williamson, S. N., Hik, D. S., Gamon, J. A., Kavanaugh, J. L., & Flowers, G. E. (2014). Estimating temperature fields from MODIS land surface temperature and air temperature observations in a sub-Arctic environment. *Remote Sensing*, **6**, 946-963.
- Wolfe, R. E., Nishihama, M., Fleig, A. J., Kuyper, J. A., Roy, D. P., Storey, J. C., & Patt, F. S. (2002). Achieving sub-pixel geolocation accuracy in support of MODIS land science. *Remote Sensing of Environment*, **83**, 31-49.
- Woo, M. K., Heron, R., Marsh, P., & Steer, P. (1983). Comparison of weather station snowfall with winter snow accumulation in high Arctic basins. *Atmosphere-Oceans*, **21**, 312-325.

- Woo, M. K., Lewkowicz, A. G., & Rouse, W. R. (1992). Response of the Canadian permafrost environment to climatic change. *Physical Geography*, **134**, 287-317.
- Wood, S.N. (2006). *Generalized Additive Models: An Introduction with R*. Chapman and Hall/CRC.
- Zaksek, K., & Schroedter-Homscheidt, M. (2009). Parameterization of air temperature in high temporal and spatial resolution from a combination of SEVIRI and MODIS instruments. *ISPRS Journal of Photogrammetry and Remote Sensing*, **4**, 414–421.
- Zar, J. H. (2009). *Biostatistical Analysis*, 5th Edition. Prentice Hall, Upper Saddle River, New Jersey, 944pp.
- Zeng, H., Jia, G., & Epstein, H. (2011). Recent changes in phenology over the northern high latitudes detected from multi-satellite data. *Environmental Research Letters*, **6**, 045508, doi:10.1088/1748-9326/6/4/045508.
- Zheng, G., & Moskal, L.M. (2009). Retrieving Leaf Area Index (LAI) using remote sensing: theories, methods and sensors. *Sensors*, **9**, 2719-2745.
- Zuur, A.F., Leno, E.N., Walker, N.J., Saveliev, A.A., & Smith, G.M. (2009). *Mixed Effects Models and Extensions in Ecology with R*, Springer.